UNIVERSITY OF LEEDS

Plate-type separator for improved separation of liquid-liquid dispersions

Charlotte Elizabeth Parrington

Submitted in accordance with the requirements for
the degree of Doctor of Philosophy

University of Leeds
School of Chemical & Process Engineering

October 2018

The candidate confirms that the work submitted is his/her own, except where work which has formed part of jointly authored publications has been included. The contribution of the candidate and the other authors to this work has been explicitly indicated below. The candidate confirms that appropriate credit has been given within the thesis where reference has been made to the work of others.

A number of publications have arisen or are under development from the work presented in this thesis:

Chapter 3:

C. Parrington, A. Baker, T. Charpentier and B. Hanson. "The effect of heavy metal ion concentration on coalescence rate in Tri-n-butyl phosphate/dodecane - nitric systems." (Accepted, Solvent Extraction and Ion Exchange.)

In addition to writing the publication, all experimental design and results were completed by myself. A. Baker assisted with the explanation of complex chemical interactions. Other authors assisted in a supervisory position.

Chapter 6 and Chapter 7:

C. Parrington, J, Keeley, T. Charpentier and B. Hanson. "Use of confinement for improved separation rates within a Plate-Type Separator" (Draft)

In addition to writing the publication, all experimental design and results were completed by myself. Dr. J. Keeley assisted with the development and validation of droplet counting code. Other authors assisted in a supervisory position.

Chapter 6 and Chapter 7:

C. Parrington, T. Charpentier and B. Hanson. "Use of super-hydrophobic organosilane coating on stainless steel for the industrialisation of the Plate-Type Separator" (Draft)

In addition to writing the publication, all experimental design and results were completed by myself. T. Charpentier assisted with metal coating methodology development. Other authors assisted in a supervisory position.

Acknowledgements

First and foremost, I would like to thank my supervisor Bruce Hanson for all his help and support throughout not only my PhD but also my undergraduate studies. Thank you for providing me with the opportunity to develop into an independent researcher and really take ownership of this project, and for always believing in me and my ideas no matter how outlandish they sometimes were.

Thanks to everybody I have worked with or shared an office with over the past 4 years, especially those in G29. You all mean the world to me, keep up the procrastination and being awesome! Special thanks to Jamie for all the vanilla ice cream, silliness, and for putting up with slightly delirious, tired Charlotte! You really made working late nights and weekends much more enjoyable :).

To all the friends I've made outside of academia, I can't thank you enough for supporting me through the highs and lows and for all the incredible memories. I can't mention everybody but special thanks to Adam, Helen, Stadius, RAB (# matebro), the men, Khal, Jord, lauren, so so many more!

Jess and Toby, thank you for being there since day one, through all the ups and downs, and on that one run! You have both believed in me more than I could ever imagine and have shown me how to believe in myself. You guys are the best friends I could have ever asked for. You both mean the world to me and I can't wait for the many, many for adventures we will have together.

Thanks to my parents and sisters, for supporting me at every step from primary school to now. You all inspire me to work hard and have fun everyday (but I'll still never sing karaoke!). Also, Dad you can stop asking me how big school is going now! Love you all 336.

Finally, I'd like to thank Jay for answering the phone in the morning whenever I needed a pep talk to get me into the lab, for the endless supply of puppers, for all the nommos, for being my best friend, and for telling me I can do the thing. I honestly couldn't have finished this without you. Thank you for making my smile everyday.

Abstract

The improved separation of liquid-liquid dispersions by coalescence has stimulated significant interest since the development of more efficient, microprocessing methods. This is due to the requirement to create fine droplet dispersions for increased mass transfer rates. However, efforts to increase mass transfer rates via an efficient mixing method are futile, if the dispersions created cannot be effectively separated.

By combining the separation properties of different advanced settling devices, the basic plate-type separator (P-TS) is highly efficient at separating immiscible fluid dispersions. This is shown through the achievement of 83 % separation with a non-optimised P-TS, separating an immiscible water-kerosene dispersion of initial droplet size 100 μm. The P-TS is manufactured from two plates, one hydrophobic and the other hydrophilic. The difference in interaction of the aqueous phase with the two plates is proven to enhance the separation efficiency of the P-TS. The simple, compact design with few crevices and no moving seals, reduces the likelihood of corrosion and increases the potential lifespan of the unit. The simplicity of the design makes the P-TS perfect for industrial application, in particular the nuclear industry; where is it easy to predict how the unit would operate within a nuclear reprocessing facility and how decommissioning with traditional methods would be achieved.

This work was completed in three stages. Firstly, an understanding of the coalescing interface was developed with static droplets. Next, the commissioning and testing of a simple P-TS was completed, with completed tests challenging the overall separation mechanism of the device with increasing plate spacings. Finally, design alterations were made to enhance coalescence and separation based on results from the previous stages.

Overall, it was found that maximising the difference between plate interaction with each phase through the use of a super-hydrophobic and hydrophilic plate configuration, the utilisation of confinement theory thought the reduction of the plate spacing, and the introduction of localised turbulence with the presence of plate textures, provided a final optimised design achieving a separation efficiency of 96.9 %.

List of Publications

The following journal and conference papers were published by the author during the course of the presented work.

C. Parrington, A. Baker, T. Charpentier, and B. Hanson. 2019. "The effect of heavy metal ion concentration on coalescence rate in Tri-n-butyl phosphate/dodecane - nitric systems." (Accepted - Solvent Extraction and Ion Exchange).

C. Parrington, and B. Hanson. "Industrial application of a plate-type coalescer for the improved separation rate of ultra-fine liquid-liquid dispersions". ISEC2017. Japan. 9/11/17.

C. Parrington, T. Charpentier, and B. Hanson. "Plate-type coalescers for improved separation of liquid-liquid dispersions". IEMPT2019. Manchester. 3/10/2018.

Contents

List of Figures

List of abbreviations

Aq	Aqueous
COEX	Co-extraction
E	Extract
FP	Fission Product
GANEX	Group actinide extraction
GEN IV	Fourth generation reactors
HLW	High Level Waste
HMI	Heavy Metal Ion
ILW	Intermediate Level Waste
L-G	Liquid-Gas
L-L	Liquid-Liquid
L-L-S	Liquid-Liquid-Solid
L-S	Liquid-Solid
Ln	Lanthanide
MA	Minor Actinide
MOX	Mixed oxide fuel
NUEX	New Uranium Extraction
Org	Organic
PACIFIC	Providing a nuclear fuel cycle in the UK for implementing carbon reduction
Pe	Peclet Number
PMMA	Poly(methyl methacrylate)
Pr	Prantl Number
P-TS	Plate-Type Separator
PUREX	Plutonium Uranium Redox Extraction
R	Raffinate
Re	Reynolds Number
SAM	Surface Active Matrix
SDS	Sodium dodecyl sulphate
SS	Stainless Steel
SS*	Non-textured, non-treated Stainless Steel
SS-C	Stainless Steel - Crosshatch texture
SS-S	Stainless Steel - Straight texture
SS-StO	Stainless Steel - Straight to Outlet texture
T-SS	Silane coated - Stainless Steel
TBP	Tri n-Butyl Phosphate
TEHP	tris(2-ethylhexyl)phosphate
THORP	Thermal oxide reprocessing plant
UREX	Uranium Extraction

Nomenclature

μ	Viscosity	h	Height
ρ	Density	f	Correction factor
ν	Viscosity/Density	n	Number of droplets
υ		R/r	Radius
α	Constant	$\dot{c}$	Coalescence Rate
β	Bond Number	$[x]$	Concentration of x
χ	Determination of dispersed phase	D	Distribution ratio
Δx	Change in x	E	Total surface energy
δ	Characteristic value of molecular size	F	Force
γ	Interfacial Tension	P	Pressure
$\dot{\Gamma}$	Shear rate	T	Temperature
ϕ	Volume fraction	U	Cohesive energy
d	Diameter	V	Volume
v	Velocity	Re	Reynolds Number
w	Width	SA	Surface Area
g	Gravity	St	Stokes Number
t	Time	SR	Surface Roughness
Cp	Specific heat capacity	Wo	Worthington Number
κ	Thermal Conductivity		

Super/Subscripts

Aq	Aqueous	0	initial
Org	Organic	m	Meniscus
C	Continuous	t	Target
D	Dispersed	e	Equilibrium
S	Solid	Vol	Volume
H	Heavy	max	Maximum
L	Light	crit	Critical
d	Droplet	h	Hydraulic diameter

Constants

κ_c	0.145 $W.m^{-1}K^{-1}$	ρ_d	996.99 $kg.m^{-3}$
Cp_c	2000 $kJ.kg^{-1}K^{-1}$	μ_c	0.89 $mPa.s$
ρ_c	788.45 $kg.m^{-3}$	μ_d	2.26 $mPa.s$

CHAPTER 1

Introduction

The United Kingdom has vast experience with managing nuclear facilities, operating 41 reactors, two reprocessing plants and several other fuel processing facilities since 1956[1]. Unfortunately, due to intermittent financial and political support, the industry will be reduced to only 5-9 reactors by the end of 2018 (dependant of end of life extensions) and no reprocessing capacity[2]. An effort to restore the industry has been made through the identifaction of 11 site for potenital new reactors[2]. These reactors would be more advanced, third generation reactors producing 16 GWe collectively[3]. Despite this effort to re-establish nuclear power within the UK, no long term reprocessing goals have been outlined and all new reactors will operate within an open fuel cycle. Overall, in terms of progression, this is considered a huge step back for UK nuclear[3]. Slow progression is not uncommon for the nuclear renaissance due to the high outlay of new nuclear investment, both financially and politically.

With this in mind, industry and research institutes are combining R&D efforts to ensure the skills and technology required are available when advances in civil nuclear are required. This research is funded within the research council R&D collaboration, PACIFIC (Providing a nuclear fuel cycle in the UK for implementing carbon reduction)[4]. PACIFIC is a collaboration of major, industrial research facilities and 12 leading UK univerisities. The main aim of PACIFIC is to address research requirements essential for the UK to achieve a closed fuel cycle[4].

There are three potential nuclear fuel cycles a country can adopt when they choose nuclear energy: open, partially closed and closed[5]. In an open, or once-through cycle, nuclear fuel is used only once to produce energy; after which the fuel is removed from the reactor, cooled and immobilised for long term storage. The open fuel cycle is the only fuel cycle option that does not recover any usable components from the spent fuel[5]. The partially closed fuel cycle reprocesses the cooled spent fuel, to recover usable uranium and plutonium[6]. The uranium and plutonium is then stored and processed for use in

mixed oxide fuel (MOX). In addition to producing a MOX fuel, an advantage of partial reprocessing is the further classification of nuclear waste. Further classification of waste can reduce the volume of waste that requires long term, deep geological storage[6]. The UK adopted a partially closed fuel cycle in 1997, however, in 2018 the thermal oxide reprocessing plant (THORP) closes, beginning an open fuel cycle for current, planned future UK reactors[7]. Finally, the closed fuel cycle incorporates advanced reprocessing techniques to recover all usable elements from spent fuel, reducing high level waste (HLW) to a minimum[8]. This is achieved by increasing the fuel acceptance window of reactors to include atoms traditionally taken as HLW including neptunium, americium and curium[8]. To achieve fission of these atoms, high temperatures are required to provide neutrons with greater energy. Neutrons with higher energies are known as fast neutrons as the increased energy causes an increase in their speed; fast neutrons are produced with fast (GEN IV) reactors[6]. The increased energy of the fast neutrons is required to cause a fission event occurring upon collision with one of the heavier actinides (uranium, plutonium, neptunion, americium etc.)[6].

Advanced chemistry options are being developed so that heavier actinides can be recovered and to reduce the proliferation, as well as the traditionally recovered uranium and plutonium. Within this thesis, traditional extraction methods are challenged to meet the requirements of the new advanced chemistry options being developed. This is achieved thought, the development of a high efficiency plate-type separator (P-TS) for the separation of immiscible liquids. The outcome of achieving this goal will be reducing separation times and volumes, providing an overall reduction in the economic impact a new reprocessing facility would have on the UK or elsewhere.

1.1 Nuclear Reprocessing

Reprocessing in its basic form is the treatment of spent nuclear fuel to recover the usable plutonium and uranium from the highly active, long lived isotopes and other wastes[5]. Advanced or further reprocessing is the extraction of uranium, plutonium and heavier

actinides. These heavier actinides are only produced within a reactor environment and therefore their potential properties are still relatively unknown; one recently discovered application on a heavier actinide is the use of americium as a constant heat source for space travel[9].

Much of the development of advanced nuclear reprocessing options has focused on the separation of actinides from lanthanides[10]. It is paramount that a high separation is achieved as lanthanides act as neutron poisons within a neutron driven system, such as within a reactor core, due to their large neutron absorption cross section[11]. Whereas, actinides are required within an advanced reactor to produce energy upon collision with a fast neutron. The separation of lanthanides and actinides is difficult due to having very similar electron structures. Displayed in the f-block of the periodic table (Figure 1.1), actinide and lanthanide outer electrons occupy the 5f and 4f subshells, respectively[11].

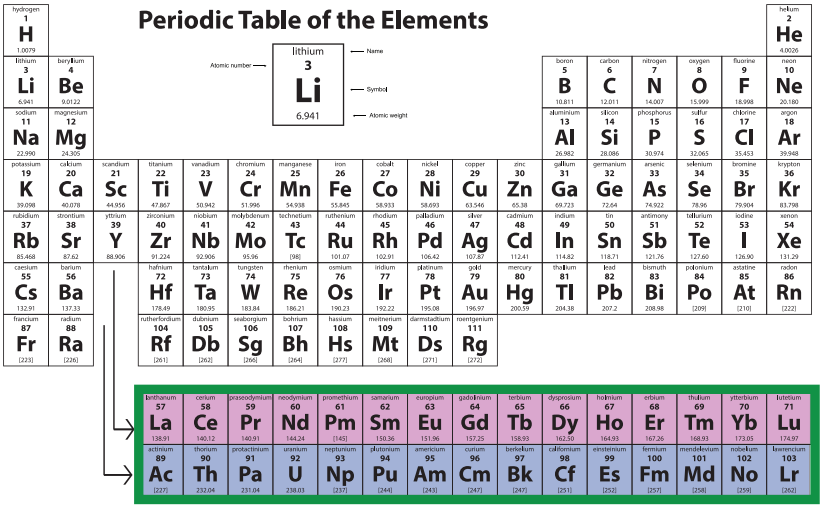

Figure 1.1: Location of F-block on periodic table; the F-block contains the Lanthanides, shown in pink, and the Actinides, shown in blue[12].

Actinides and lanthanides have similar ionic radii due to indentical inner electrons[13]. The property utilised in reprocessing is the bonding strength between the nucleus and actinide outer shell electrons[14]. As the actinides outer most electrons, the electrons in the 5f subshell, are less tightly bound to the nucleus, therefore, feel less of an attraction

to those in the 4f or 5d subshells. This slight difference gives actinides a minimal but important increased attraction to alkaline solutions[14], which is taken advantage of within nuclear reprocessing. It is this behaviour that means actinides can form more oxidation states within aqueous solutions; for example americium can be forced into oxidation states III,IV,V and VI, whereas a lanthanide (Ln) in a aqueous solution will exist prominently in the trivalent state, Ln(III)[14]. Controlling an elements oxidation state using different acidic and alkaline conditions allows for the control of which chemical complex the element will form with the extraction ligand. The control of process chemistry allows for the removal of the desirded element(s) from others within an aqueous solution, forming the basis of solvent extraction based reprocessing[14].

1.2 Solvent Extraction

There are many different proposed methods for reprocessing nuclear fuel; ion exchange, electrolysis and solvent extraction are just a few[10]. Solvent extraction is currently the only method commercially used[15].

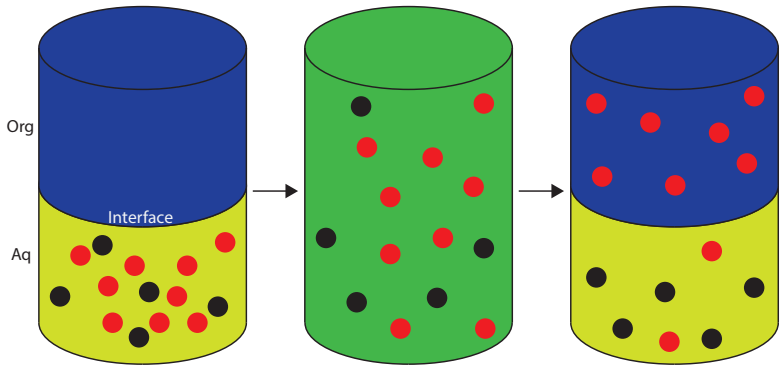

Figure 1.2: Schematic representation of a basic solvent extraction stage. Solute A (red), initially dissolved in the aqueous phase (yellow) with unwanted solutes (black), is extracted into the organic phase (blue). Extraction occurs when the two phases are mixed (shown as green). Both solutes are then distributed between the upper and lower phases.

Solvent extraction in its simplest form is illustrated in Figure 1.2. In basic solvent extraction, a vessel is filled with two fluids of different phases, an aqueous (Aq, yellow)

and an organic (Org, blue). The desired solute (solute A, shown in red) is initially dissolved into the aqueous phase with other undesired elements (shown in black). Through contact with the organic phase, solute A is extracted and distributed between the two phases; provided the organic phase has a chemical affintity for only solvent A and not the undesired elements. At equilibrium solute A is distributed between the phases in the distribution ratio given by Equation 1.2, where D is the distribution ratio, $[A]_{Org}$ the concentration of A in the organic phase and $[A]_{Aq}$ the concentration of A in the aqueous phase[16].

$$D = \frac{[A]_{Org}}{[A]_{Aq}} \tag{1.1}$$

The distribution ratio is used to determine the extent of extraction at equilibrium. For a system where A is extracted into the organic phase from the aqueous; the larger the distribution ratio the greater the extent of extraction. To control the distribution ratio the extractant itself can be altered to an extractant with a higher affinity for the solute[16].

Once the system is confirmed and the distribution ratio known, the number of stages to achieve the required extraction is calculated. This calculation is outside of the scope of this work, as it focuses solely on a single stage of separation. However, for a detailed description of stages undertaken to complete this process, see Chemical Engineering, Volume 2: Particle Technology and Separation Processes[17].

To reach industry standard extraction extents, simple extraction, as shown in Figure 1.2, must be accompanied by other processing stages within a flowsheet. Using Figure 1.3 to aid with the explanation of terminology, it can be seen that these flowsheet processing stages start with a feed. The feed is an aqueous solution entering the process containing the material/s to be recovered (the desired solute) in a mixture with undesired waste products. The feed meets a recycled solvent phase in a joint extraction and separation unit (shown in red)[16]. Within the extraction and separation unit, the phases are intimately mixed to increase the rate of extraction of the desired solute into the solvent phase. The waste products, remaining in the aqueous phase, are taken as raffinate. Whereas the

loaded solvent phase is taken as extract. Commonly the raffinate will undergo the extraction/separation stage several times, determined by the distribution ratio and required extraction requirement of the system.

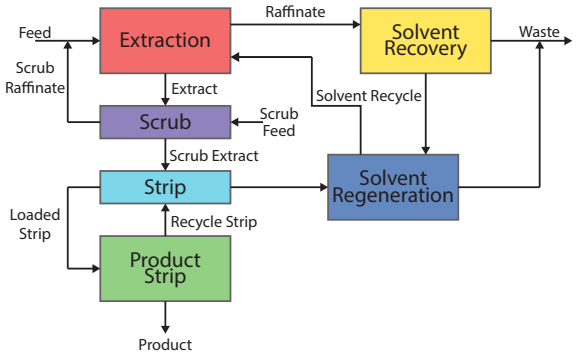

Figure 1.3: An example of a traditional solvent extraction flow sheet showing the stages required to extract the desired solute from a mixed feed [16].

Once the raffinate has been depleted of the solute, it passes through solvent recovery (yellow) to remove any entrained solvent phase which may have been carried over. Phase entrainment is the capture of liquid droplets within the continuous phase which are of a droplet size and weight that Brownian motion is dominant and therefore will not readily phase separate under gravity [16]. Once any solvent is recovered the aqueous raffinate is processed as waste.

Solvents rarely have affinity for only the desired product and usually some waste solutes are co-extracted into the solvent phase during the first extraction (shown in red in Figure 1.3) [16]. These impurities have to be extracted back from the solvent into an aqueous phase in the purple scrubbing section in Figure 1.3, where the scrub feed is usually a higher molarity solution of the pure aqueous feed. Post scrub, the scrub raffinate is taken to join the feed to ensure desired product has been back extracted and the scrub extract is taken into a strip section (light blue in Figure 1.3). The strip section is designed to strip or back-extract the desired solute from the organic scrub extract into a clean aqueous phase [16]. It is preferred for product recovery and finishing that the final form of the recovered solute is in an aqueous phase, as typical recovery processes such as precipitation and evaporation are more readily achievable for aqueous than solvent phases [10]. The strip stage

also allows for phase recovery and regeneration, this is important both environmentally and economically[18].

As discussed above the extraction/separation stage is commonly repeated in order to achieve desired extraction efficiencies. The repetition of extraction/separation processes to maximise extraction extent is called a stage wise process as the extraction occurs over a series of stages. The stages can be arranged in three ways[18]: co-current, counter-current and cross-current, each is outlined in Figure 1.4

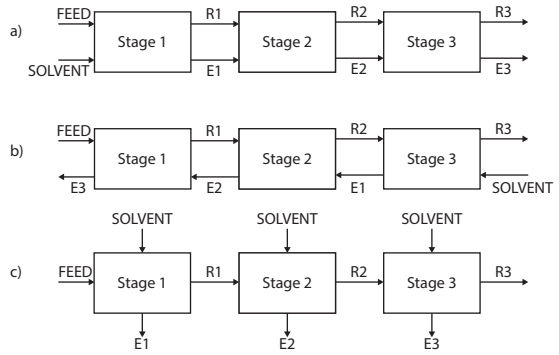

Figure 1.4: Different stage arrangements for stage wise solvent extraction processes, where E and R show the direction of flow of the extract and raffinate streams[18]; a) co-current; b) counter-current; c) cross-current.

In co-current extraction, Figure 1.4a, there is no real benefit to stage wise processing as equilibrium will have been reached within stage 1. The phase equilibrium will continue in any following stages as there is no addition of fresh feed therefore equilibrium conditions will be maintained[18]. Counter-current processing, Figure 1.4b, is the industry standard as this method is most efficient for extraction as the concentration gradient is always maximised. For example, within stage three the dilute raffinate is introduced to a fresh solvent feed. Counter-current extraction provides efficient extraction while maintaining a constant phase volume. Cross-current extraction methods, Figure 1.4c, also achieve high extraction efficiencies, however, use much larger volumes of solvent. Cross-current methods mimic the basic processing stages of using a separating funnel within a laboratory. As the raffinate is always introduced to a fresh solvent feed the extraction extent is high, however, this creates large volumes of extracts with varying concentrations which are combined for

scrubbing and stripping[18].

1.2.1 PUREX

The most common solvent-extraction-based reprocessing technique is PUREX (Plutonium Uranium Redox EXtraction)[5]. PUREX was first operated at full scale on irradiated nuclear fuel in 1954, and was developed at Chalk River National Laboratory, Canada[13]. Initially designed for the separation of plutonium for atomic weapons manufacture, the process was adapted by the civil nuclear sector into a commercial reprocessing technique in 1956[5]. As a consequence of its origins, PUREX provides separated uranium and plutonium aqueous product streams increasing the risk of proliferation. These streams are individually processed before re-mixing to produce a mixed oxide fuel (MOX)[19]. The PUREX process is well established within the industry, but is starting to be considered an outdated technique for the modern political, economic and environmental requirements[5,7,19]. With research focusing on developing the technology to support a closed fuel cycle, advanced reprocessing techniques have been developed such as COEX, NUEX and UREX[20]. In Figure 1.5, it can be seen that advanced reprocessing options avoid separating the uranium and plutonium fully and directly produce a MOX fuel. This reduces the proliferation risks associated with PUREX. These processes are more commonly associated with the collective term "advanced PUREX techniques" as they still recover only the uranium and plutonium and require a secondary process to separate FPs, minor actinides (MA) and lanthanides.

1.3 Traditional Separation Equipment

The primary objective for solvent extraction equipment is to create a homogeneous mixture of aqueous and organic solvent phases[22]. This intimate mixing increases the rate of mass transfer between phases as the surface area of dispersed droplets is increased[23]. The majority of research and equipment advances in this area for the past decade have been aimed at improving the rate of mass transfer by increasing surface area through improved

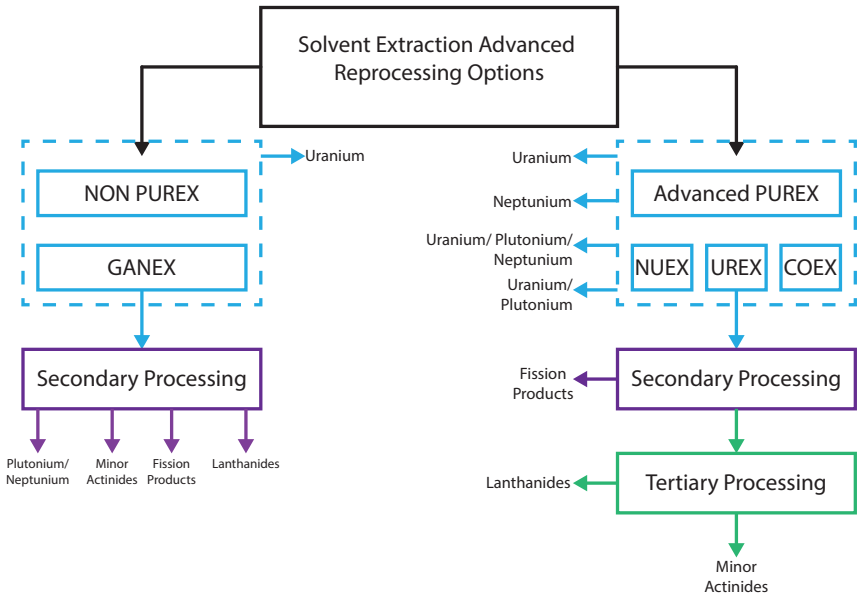

Figure 1.5: Flow sheet representation of advanced reprocessing options (all abbreviations defined in list of abbreviations)[21].

mixing, however, this increased extent of mixing is worthless if the dispersion cannot be separated within a desirable time frame[24,25].

Within the nuclear reprocessing industry, pulsed columns and mixer settlers (Shown in Figures 1.6 and 1.7) are ideal for use within radiation areas, however, these are now becoming recognised as potenitally unsuitable in terms of their mixing and separating functionality for future process requirements. Other industries have the advantage of significantly less design considerations and easy access to equipment for the retrofit of updates and completing maintenance. This combination greatly increases the speed in which research and development outcomes can be tested and implemented, allowing non-nuclear industries to keep process equipment up to date.

Much of the process equipment used in conventional solvent extraction must be altered or redesigned before use within high radiation environments. A typical example of equipment redesign is the relocation of motors/moving parts. These pieces, the most likely to require maintenance over the life cycle of the plant, are relocated to accessible areas, outside of the radiation risk. In some occasions, this relocation is not a viable and equipment must be designed specifically for the nuclear industry; the pulsed column is an example

of this. Designed specifically for liquid-liquid nuclear systems the pulse column is tall, thin and has no moving seals. This design is ideal for high radiation nuclear applications, especially where criticality control of highly active liquids is required[26].

Like all liquid-liquid extraction systems, the mixing of the two phases is key to achieving high mass transfer efficiencies between phases. In a pulsed column, the two phases are fed into the column with the aqueous inlet at the top and organic inlet at the bottom[26]. The column is designed as such that with gravity the two phases will separate over time. Pulsation is used to force the organic up through the perforated plates and drag the aqueous down, shown in Figure 1.6.

The size of the holes in the plates, as well as the amplitude, and frequency of the pulsations control the droplet size of the dispersed phase (organic) within the continuous phase. Each plate spacing is considered to be the equivalent of a single mixer settler stage, however, unlike for mixer settlers, the mass transfer coefficient for pulsed columns is difficult to calculate directly as the flow dynamics and extraction within a pulse column are more complex and less well defined[27].

The mixer settler, shown in Figure 1.7, has two discrete sections for mixing and settling[28]. Within the mixing section, the two phases are combined using a high shear overhead impeller. The dispersion then flows over a weir and enters the settling area[28]. Within high radiation areas, this settling area is kept as simple gravity separation, whereas, in non-radiation areas, this can be retrofitted to allow for enhanced gravity settling options, see Section 1.3.2. A mixer settler can only be used for lower activity liquid processing (primarily uranium processing) as the large volume settling area does not provide criticality control of highly active liquids[26].

The advantage of a mixer settler over a pulse column is, the mixer settler design is well defined and frequently used in many industries. This makes the mixer settler the cheaper option in comparison to the pulse column. In order to adapt a mixer settler for a nuclear environment, the impeller motor is moved out of high radiation areas for safe maintenance access.

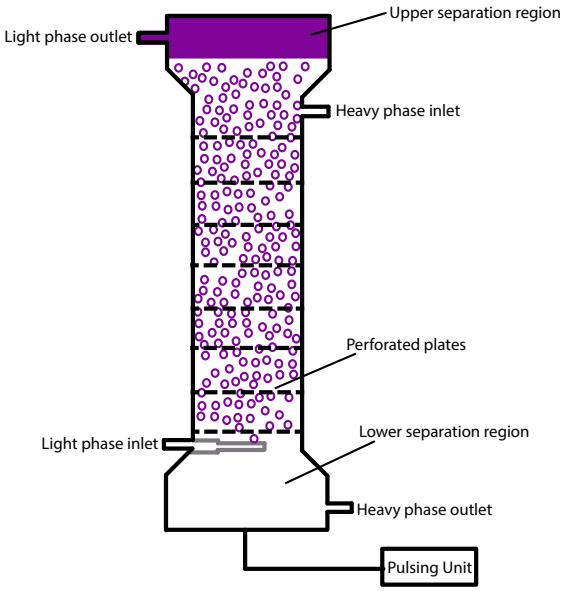

Figure 1.6: A Schematic of the internal workings of a pulse column. The light phase is introduced at the bottom where is it forced upwards through perforated plates. Phases are separated in upper and lower separation regions.

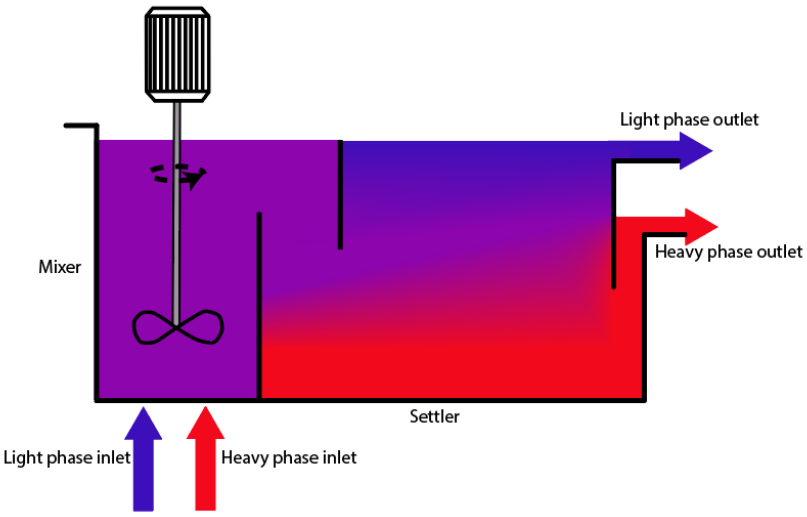

Figure 1.7: A Schematic of the internal workings of a mixer settler. The light and heavy phases are introduced to the mixing region, where they are combined. The dispersion flows over a weir into the separation region, and gravity separates. The separated phases are collected via weir overflow.

1.3.1 Gravity separation

Gravity separation is the simplest form of separation techniques and is governed by Stokes law.

$$v_s = \frac{g(\rho_H - \rho_L)d^2}{18\mu_c} \tag{1.2}$$

Where v_s is the settling velocity, g the gravitational constant, ρ_H and ρ_L the densities of the heavy and light phases, d the droplet diameter and μ_c is the continuous phase viscosity[17].

Stokes law is used to calculate the settling rate of the dispersed droplets within the continuous phase using three main parameters: difference in phase density, droplet diameter and continuous phase viscosity[17]. The difference in density between phases is considered because if the density difference is too large, the phases will readily separate, forming an unstable dispersion. The second parameter is the droplet diameter, as smaller droplets are dominated by Brownian forces as opposed to gravitational forces. Droplets dominated by Brownian motion are not likely to separate in an acceptable time frame as they are more likely to be caught in eddy or convection currents during settling time. Finally, Stokes law considers the viscosity of the continuous phase, as a high viscosity continuous phase will be thicker, slowing the settling velocity of droplets.

Separators for gravity settling designed solely using estimations from Stokes law are often much greater in volume than is required, as Stokes law assumes all droplets are spherical and are moving freely in a stagnant flow[29]. A more comprehensive representation of a settling unit would consider turbulent regions at fluid entrances, which cause eddy currents throughout the separator. This turbulance can drag droplets away from what the undisturbed trajectory would be. Turbulence in the unit can also distort droplets away from the spherical shape, causing a drop in velocity due to the increased drag[29].

1.3.2 Enhanced gravity separators

To address many issues identified with designing using Stokes law, baffles are introduced to the separation area. The baffles are designed to minimise the effect of turbulence from the fluid entry point by partitioning the large volume of the separating unit into smaller channels. The effective settling volume is now relative to the baffle spacing and the distance travelled by the droplet before reaching an interface is greatly reduced[29]. The baffle plates also provide a larger surface area for droplet coalesce by increasing the internal surface area of the settling region.

Enhanced gravity separators are more efficient and compact compared to standard gravity settlers making them ideal for commercial use[26]. However, the introduction of baffles also introduces crevices and potential for stagnant flow, both of which are not acceptable within high radiation areas.

1.3.3 Coalescers

To promote coalescence, baffle plates can be accompanied by a wire mesh at the inlet. The principle of adding a wire mesh is the same principle behind the design of a coalescer. The aim of a coalescer is to increase the surface area on which a droplet can settle on, as increasing the number of droplets that settle increases the likelihood of a coalescence event occurring. Coalesced droplets attached to the coalescer internals, known as the target, then capture other droplets within the flow. Once a critical droplet mass is achieved the droplets fall off the mesh and collect at the bottom of the coalescer, this process is shown in Figure 1.8.

As with the baffle plates, the flow conditions within the equipment must be controlled. To determine the most effective target size and flow velocity, Stokes number is calculated[17],

$$St = \frac{\rho_d v (d_d)^2}{18 \mu_c d_t} \tag{1.3}$$

where Stokes number, St, is calculated using the dispersed phase density, ρ_d, and the droplet diameter, d, the flow velocity, v, viscosity of the continuous phase, μ_c, and the

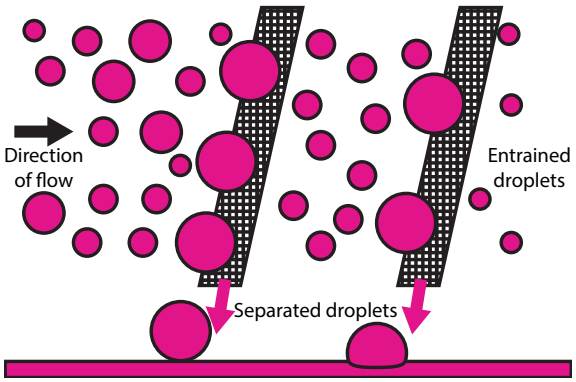

Figure 1.8: A schematic of a coalescer. Droplets within the flow are captured by the coalescer target, separating them from the bulk flow.

coalescer target diameter d_t.

As droplet collection efficiency increases with Stokes number it can be assumed from Equation 1.3 that droplet collection will increase with increasing velocity, decreasing continuous phase viscosity and decreasing target diameter. This assumption is true, however, a compromise between the three factors must be found.

Greater flow rates increase the probability of smaller droplets impacting on the target rather than flowing around targets in streamlines. However, greater flow rates also cause low mass, coalesced droplets to prematurely fall off targets, reintroducing them to the flow. High flow rates can also promote further droplet break up as droplets impact on thin target wires with higher velocities [17].

Decreasing continuous phase viscosity allows dispersed droplets to move more freely within the continuous phases at higher settling velocities due to reduction in drag. The most common way of decreasing the viscosity of a system is to heat the continuous phase, however, heat within liquid-liquid extraction processes could increase solubility of the phases, reducing separation [29].

Finally, decreasing the target diameter allows for control of flow around the targets and through the coalescer as turbulence is reduced allowing for streamlines to flow undisturbed [29]. Through careful design, these streamlines can be manipulated to force smaller droplets towards a target to impact upon. However, reducing the target diameter too far can mean that droplets bypass the coalescer completely unless the target density is

increased.

Coalescers cannot solely be designed on first principle and require more complex, computational fluid dynamic modelling to optimize droplet collection efficiency.

1.3.4 Centrifuge

A final, commonly used liquid-liquid (L-L) separator is the centrifuge[30]. The disk or bowl centrifuge is recommended for the separation of L-L dispersions, as they are designed to separate mixtures with specific gravity differences of $0.01g^{-1}$ and dispersed droplets down to $1\mu m$[30].

For large centrifugal extractors, sieved trays surround the inner shaft. The heavy phase is fed into the centre of the unit and the light phase at the outer edge[18]. As the unit rotates, the heavy phase is forced against the inner side of the sieved tray. Once the rotation speed is fast enough the heavy phase jets through the sieve holes towards the outer shell of the extractor[18]. The same occurs with the light phase, travelling inwards towards the outer side of the sieved tray and jetting through the sieved holes towards the central shaft . The movement of each phase through the sieved holes and the jetting into droplets ensures large transfer areas and efficient counter-current extraction[17]. The heavy phase continues through the extractor to the outer edge where is collects; whilst the light phase collects at the inner shaft[17].

The most common industrial centrifugal contactor is the Podbielniak extractor[18]. The Podbielniak extractor works based on the same principles as above however is usually positioned horizontally, unlike other common centrifuges[17]. Centrifuges are preferred for systems with very low density differences, such as in uranium enrichment. They have a low hold up, meaning the time taken between entering and exiting the unit is reduced, ideal for systems where contact between organic and acidic aqueous phases must be kept to a minimum[17]. Due to the high efficiency of the extraction and separation, the size of the unit is usually smaller that other extraction units, therefore, a lower volume of solvent is required[17].

Implementing centrifugal extractors in high radiation areas is difficult due to the high

maintenance requirements of the large numbers of moving parts. Other disadvantages of centrifugal extractors are, high initial cost and high operational energy requirements, leading to high operational costs[5].

1.4 Plate-Type Separator

The P-TS has been identified as an alternative separation device for the separation of immiscible L-L dispersions. The microfluidic device, currently only used for research purposes, has been reported to reduce turbulence and separate fine dispersions rapidly by combining characteristics of both coalescers and enhanced gravity separators[31,32]. Based on the review of current technologies above, the P-TS could easily be introduced to a low viscosity L-L industrial environment given the easy to bulk manufacture design, minimal operational maintenance and low operational costs. In addition to this, the lack of moving parts and stagnation areas make the design ideal for use within high radiation areas as opposed to centrifugation.

The first device of this kind was developed by Okubo *et al.* in 2004[32]. The overall aim of this initial research was to explore liquid-liquid dispersion separation using a simple micro-flow device. Their research methodology focused on understanding the interaction between plate material and fluid. The device was the smallest of those that have been reported on and used the Polytetrafluoroethylene-glass (PTFE-glass) plate combination. The channel was a 10 mm square and the channel depth was created by placing foil gaskets of different thickness (5 or 12 μm) between the plates, shown in Figure 1.9.

Two experimental methodologies were used to feed the device, direct introduction of a dispersion into the microchannel device and the introduction of prepared and stabilised dispersion. The direct feed methodology used a micromixer, manufactured by IMM (Mainz, Germany) (25 μm outlet slit) to create dispersions of water and dodecane. This was fed into the device via 75 mm of silicone tube. The second method used the micromixer to create a dispersion of water and octanol, the dispersion was stabilised using a 0.5 wt% sodium dodecyl sulphate (SDS) aqueous surfactant solution. This dispersion was later

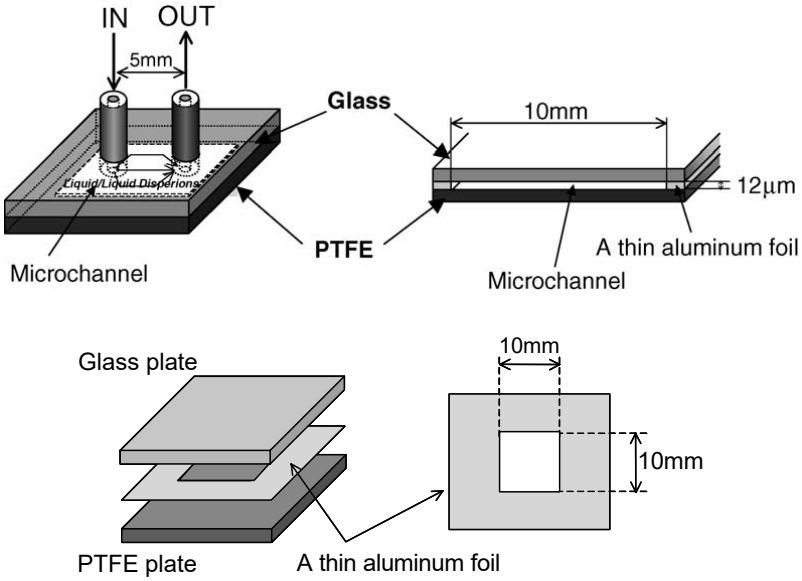

Figure 1.9: Structure and fabrication of a simple microchannel device[32].

fed into the micro-channel device using micro-syringe pump. Dispersion characteristics of both water-dodecane and water-octanol were observed using a laser scattering, particle size distribution analysis and visual analysis with a microscope. Investigations varied feed flow rates, materials of construction combinations and channel depths. For each investigation the effect on separation efficiency was recorded.

In terms of coalescence achieved within this study, it was found that with 2.7 ml/min water and 0.3 ml/min dodecane fed into the MC device using the direct feed method, separation was almost 100 % efficient. Upon observing the aqueous exit liquid with a microscope it was found that the entrained organic droplets were less than 10 μm diameter. This separation occurred with an upper plate of glass and lower PTFE, with a channel depth of 12 μm and residence time of 0.01 s. Overall it was found that the dispersed droplets diameter decreased when flow rate was increased or when the dispersed phase ratio was decreased.

A polypropylene sheet (100 μm) was then used to replace the foil and provide an increased channel depth. No difference of the inlet and outlet dispersions was observed. A possible explanation for this is that using a third material altered the spreading characteristics of the fluids. Okubo *et al.* also completed tests within a glass-glass configuration,

finding it did not provide any overall coalescence.

Octanol was used to replace the solvent feed for the second methodology due to its ability to form H-bonds with water and create stable emulsions. Using the glass-PTFE plate combination and a dispersion of octanol in water (1:4 octanol:water ratio) with a droplet distribution of 2-18 μm, it was found that an overall flow rate of 0.3 ml/min provided 100% separation of all droplets greater than 10 μm. However, when the overall flow rate was increased to 2.0 ml/min no separation was observed. This flow rate limit was then investigated for water-dodecane mixtures using method one and it was found that separation was possible up to 6.0 ml/min. A suggestion for this behaviour is that water-octanol have a natural affinity for each other unlike water-dodecane making them more challenging to separate.

It was concluded that the successful coalescence of droplets with a smaller diameter than the channel height must occur within the device, and must be governed by the difference in velocity created by the interaction with plate materials. Figure 1.10 shows droplet development over time, where the velocity of larger droplets will decrease relative to the smaller droplets. It is predicted that this change in velocity is the cause of the increase in coalescence. From Figure 1.10 it can be theorised that, with a higher residence time smaller droplets will also coalesce, suggesting that scale up will require lengthening the plates. This theory is supported by the data carried out by Kolehmainen and Turunen (2007) who achieved 80% and higher separation of dispersions with an average droplet diameter of less than the channel height and in the region of 100% when the droplet diameter equalled that of the channel height. Their plate area was 3000 mm^2 in comparison to 100 mm^2.

Kolehmainen and Turunen, 2007[31] discuss that it is now easier to create a dispersion of micro droplets than it is to separate one, due to modern equipment advances in mixing. The aim of their research was to continue that of Okubo *et al.*, and assess the efficiency of a larger P-TS, using droplet size information and phase separation efficiency data. Their P-TS consisted of two plates, a PTFE upper and stainless steel (SS) lower plate. The plates were sandwiched together with a milled channel between, the channel was 15 mm

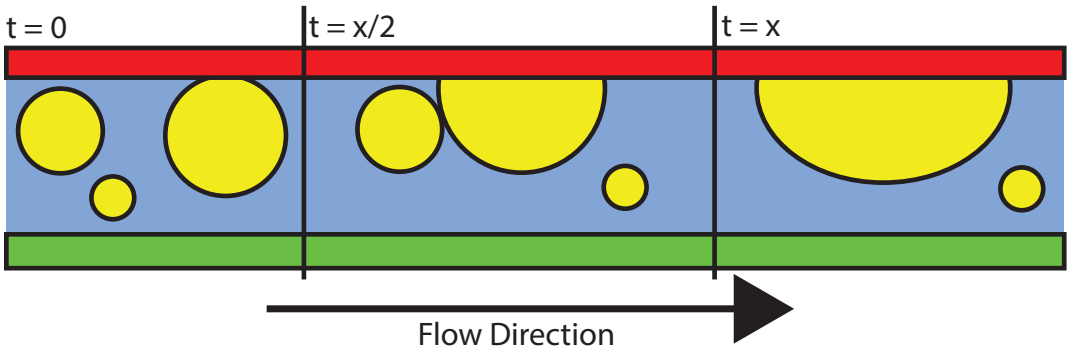

Figure 1.10: Schematic of droplet coalescence for a droplet diameter is less than the plate spacing.

wide, 200 mm long. The channel depth was varied from 100 and 200 μm. Experimental work was undertaken at room temperature (295 K) using water as the aqueous phase and Shellsol D60 with 10, 30 and 50% Tris(2-ethylhexyl)phosphate (TEHP) as the organic phase. Shellsol D60 is a mixture of C10-C12 paraffins and naphthenes and TEHP is a common liquid-liquid extractant used predominately to extract metallic elements. The two phases were fed through an IMM slit micromixer to create a fine dispersion and then passed directly though the P-TS, shown in Figure 1.11.

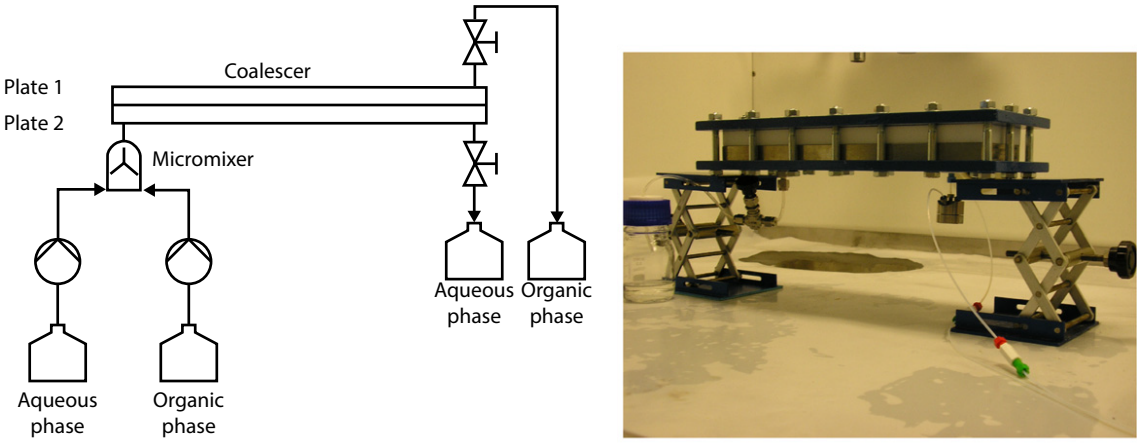

Figure 1.11: Experimental set up used by Kolehmainen and Turunen (2007)[31].

Kolehmainen and Turunen (2007)[31] found that: surface material, channel height, fluid composition, average fluid velocity and residence time all effected the separation efficiency. They managed to achieve complete separation when total flow rate was less than or equal to 3 ml/min (corresponding to superficial velocities of 3.3 cm/s for 100 μm depth and 1.7 cm/s

200 μm depth). Above 3 ml/min a separation efficiency of greater than 80% was still achievable depending on the plate spacing. For plate spacings of 100 μm and 200 μm at a flow rate of 8 ml/min, separation efficiencies of 90% and 80% were achieved.

It was reported that when the average droplet diameter is equal to the channel height separation will be 100%, as the droplets are forced to contact and spread on the plate surface causing them to slow down. This slowing increases the chance of the smaller droplets contacting and coalescing with the larger. It is important to note that within this study entrainment of the organic was not accounted for and therefore separation efficiency reported could be significantly lower.

As stated previously the plate materials were SS and PTFE, however, PTFE-PTFE and PTFE-glass plate combinations were also tested. PTFE-PTFE provided no separation, suggesting that the liquid interaction with the materials of construction of the P-TS is crucial in maintaining sufficient extraction extent. This result supports those of the glass-glass configuration from Okubo *et al.* suggesting that two different materials are required for separation to occur within the P-TS. The PTFE-glass plate combination provided separation up to 200 μm, however, at significantly reduced separation efficiencies. Both Kolehmainen *et al.* and Okubo *et al.* record the contact angle of each phase on the plate material, finding that the aqueous phase is more likely to spread on the glass or stainless steel as they are hydrophilic. The aqueous is likely to be repelled from the PTFE, hydrophobic plate which is wetted by the organic. This remains the current understanding of how the P-TS works and why separation efficiency increases when the average droplet diameter is equal to that of the plate spacing. Both studies also state that the P-TS separation efficiency is not effected when used vertically.

The most significant result provided from Kolehmainen *et al.* was found when comparing P-TS rates to gravity settling. They report 100% separation of a dispersion of average droplet sizes 60 to 120 μm of water/Shellsol + 10 %TEHP in a residence time of 20 s. Whereas, the gravity separation time within a separation funnel of the same dispersion was upwards of 30 minutes. This data shows that the P-TS can provide the efficiency improvements that are required to fulfil the outcome of this research, providing efficiency

is maintained upon scale up.

Following on from the above research, a group at Sichuan university, China, published results documenting the de-emulsification of water/kerosene emulsions[33]. The author criticises the research of Kolehmainen *et al.* and Okubo *et al.* for their use of the IMM micromixer in both instances as the systems used large droplets (200 μm dimeter) which are unstable when this equipment is not used. Dispersions with larger droplets, like those produced with the IMM micromixer, would separate rapidly without the aid of stabilisers and therefore the separation efficiencies presented above are potentially a mixture of natural gravity separation and the effect of the P-TS. To address this, Chen *et al.* used a high shear mixing apparatus rotating at 12 ,000 revolutions per minute (RPM) for 100 s. The emulsions were analysed to find the droplet size distribution using a laser particle analyser and visual testing with a light microscope. Once the emulsions where formed they were forced through the P-TS by pressurising the inlet vessel and relying on pressure differentials to feed the separator. Two P-TSs were used, both were of the SS-PTFE configuration, with an aluminium shim to provide the plate spacing. The dimensions of the separators were 10 mm wide by 43 and 87 mm long, and the plate spacings used were 100, 140 and 200 μm. The actual plate spacing used were approximately 20 - 30 μm smaller than this however as the PTFE plate distorted, allowing the shim to embed itself into the plastic and reduce the volume of the channel.

Results from Chen *et al.* show an increase in de-emulsification with increasing flow rate until a plateau at approximately 10 mL/min[33]. This plateau is most likely due to increased shear forces, this ability of micro-channels is well known and there are numerous publications on dispersion creation using a micro-channel, for this reason it is assumed that above 10 mL/min there is a balance between coalescence and dispersion creation. It would be expected that if the flow rate was increased further the separation efficiency would start to decrease.

Chen *et al.* confirm that gravity effects can be neglected as no change in de-emulsification efficiency was observed when the PTFE plate was above or below the shim; supporting the finding of Kolehmainen and Turunen[31,32].

Single stage efficiencies of 10% were reported which are far below industry requirements so the lower aqueous phase was recirculated. It was shown that for a 30% water-kerosene emulsion, 90% separation could be achieved in 5 iterations[33]. Droplet size distributions of initial and post separation emulsions after multiple iterations show that large droplets ($\geq 17.6\,\mu$m) are easily removed and smaller droplets coalesce into larger droplets during the recirculation iterations.

Chen *et al.* found equal de-emulsification efficiency when using a PTFE-PTFE configuration as when using the PTFE-SS configuration which is unlike what was published previously. They had expected the PTFE-PTFE configuration to provide much greater separation efficiency as the droplet interactions with the hydrophobic (PTFE) plate causes large oil droplets to adsorb onto the surface allowing for increased probability of collisions leading to coalescence events[33,34]. The asymmetric velocity profile experienced in the PTFE-SS configuration is given as the cause of the discrepancy from what was expected. This is discussed in more detail in Section 4.2.

Applying aspects of the above studies completed by Kolehmainen *et al.* and Okubo *et al.*, a study was conducted at the University of Lorraine into how the dimensions of a plate-type micro separator affect the demulsification of oil-in-water[35]. This study did not reference the work conducted by Chen *et al.*. This study used a PTFE-SS plate combination with a shellsol/water emulsion, the emulsion was stabilised using the surfactant Tween-80. They varied the size of the separator, channel depth, flow rates and plate configuration to determine the optimum size for a P-TS.

Three reactor types were used, shown in Figure 1.12, R1 being the largest (21x530 mm WxL) and R2/R3 which are smaller (16x60 mm WxL). The channel depth of R1 was variable (25-100 μm) depending on the tightness of the clamping plate. The study states that there was a problem with this method as the seal placed within a groove in the PTFE plate (shown in Figure 1.12a) was thicker than anticipated, also using the tightening method allowed for slight variation in channel depth along the length of the separator. R2 was manufactured so the separator channel and seal were machined out of the stainless steel plate, as opposed to the PTFE plate in R1 and, used a fluoroelastomer seal like R1.

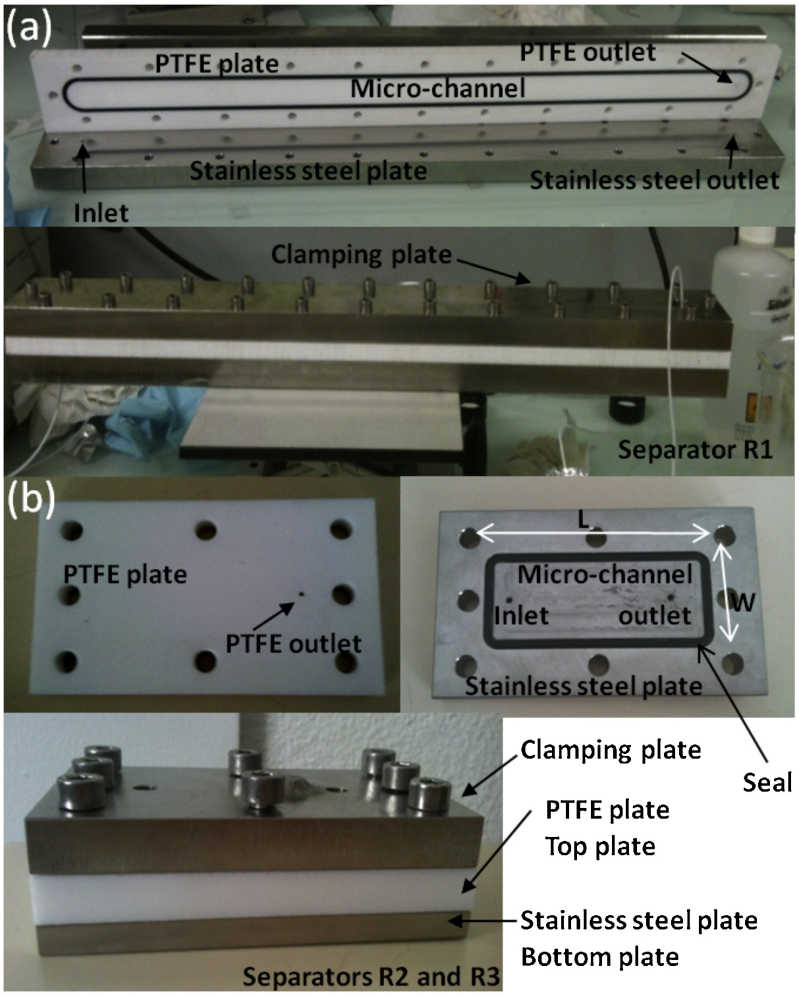

Figure 1.12: P-TS used in investigation conducted by Roques-Carmes (2014), a) R1 and b) R2 which is the same dimensions as R3 (not shown)[35].

R3 used thin aluminium foils to create the channel depth. The reactor depth of R2 and R3 was determined by laser-scanning surface profilometry at 9 locations along the channel, the channel height of R2 is $87 \pm 2\,\mu$m, and R3 is $9 \pm 1\,\mu$m.

The droplet size distribution of the incoming and outlet stream was determined using laser diffraction granulometry with a mastersizer 2000. The difference between this study and the previous is the focus on emulsions, where the average droplet size within the mixture was $8.7\,\mu$m. This average droplet size is significantly smaller than the majority of channel depths within this study, based on knowledge from previous work this suggests that the efficiency of separation will be less than what was achieved by Kolehmainen

and Turunen (2007) and Okubo, Toma *et al.* (2004)[31,32]. Results from Roque-Carmes, Monnier *et al.*. (2014)[35] shown in Figure 1.13 conclude that when droplet size is much less that the separator channel height (R1 and R2) then the separation efficiency is less, supporting this strong dependency on the ratio between droplet distribution size and channel height.

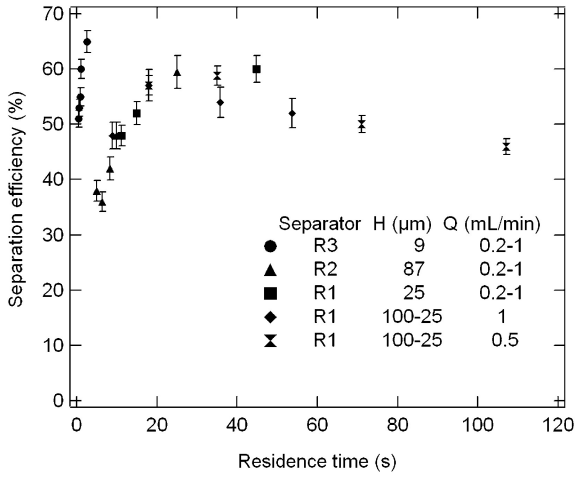

Figure 1.13: Separation efficiency as a function of residence time for different separators, flow rates (Q) and channel depths (H)[35].

It can be seen that, for channel heights much greater than the droplet size there tends to be a maximum separation efficiency at approximately 40 s residence time, however, completely separation was not achieved. Roque-Carmes, Monnier at al. (2014) suggest that this could be due to the larger drop sizes being separated and smaller diameter droplets within the droplet size distribution remaining within the flow without contacting either plate or other droplets. This however does not explain why the residence time increasing causes the separation efficiency to drop[35].

These results suggest that with the correct channel height for a droplet dispersion and a long residence time that close to 100% separation is achievable, which is supported by the results from Kolehmainen and Turunen (2007). This is also supported by the steep gradient in the R3 data within Figure 1.13. From the result in all three studies, it is clear that when the channel depth is similar to the average droplet size, the dominate separation mechanism is coalescence. Roque-Carmes, Monnier *et al.* (2014) conclude

that both channel depth and surface area to volume ratio are combined to intensify the separation, and state that in this situation (R3) capillary forces dominate[35].

A summary of parameters investigated by previous studies is provided in Table 1.1.

Table 1.1: Summary of previous P-TS investigations. The z-dimensions are the plate spacings investigated, unless specified the plate spacing was provided by an interchangeable gasket.

Investigation	**x-y dimensions (mm)**	**z dimensions (μm)**	**Materials of construction**	**L-L system**	**Flow rates (mL/min)**
Okubo, Toma *et al.*[32]	10 x 10	5 - 12	PTFE-PTFE Glass-Glass	Water-Dodecane Water-Octanol-SDS	Up to 6
Kolehmainen and Turunen[31]	15 x 200	100 - 200 (milled)	PTFE-SS PTFE-PTFE PTFE-Glass	Water-Shellsol-TEHP	Up to 8
Chen *et al.*[33]	10 x 43 10 x 87	100,140,200	PTFE-SS PTFE-Glass	Water-Kerosene-SDS	Up to 20
Roques-Carmes, Monnier *et al.*[35]	R1 - 21x530 R2/R3 - 16x60	R1 - 25-100 R2 - 87 R3 - 9	PTFE-SS	Water-Shellsol-Tween80	Up to 1

1.5 Structure of Thesis

This thesis comprises of two main parts. Part one focuses on static droplet coalescence and part two, flow-driven coalescence.

Part one, comprising of Chapters 2 and 3, and contains investigations into different factors that could effect the separation efficiency of traditional nuclear reprocessing facilities if a microfluidic separation device was to be implemented. Within this part, Chapter 2 covers the supporting theory to the experimental chapter, Chapter 3. The aim of part one is to find the effect of pH, solvent dilution and heavy metal ion concentration, $[HMI]$, on contact angle, interfacial tension and coalescence rate.

Following on from this, part two focuses on how the design of the P-TS effects the efficiency of separation. Chapter 4 expands on the static theory and how this can be applied to the coalescence of flowing droplets within the P-TS. This theory is applied in a series of experimental investigations developing the methodology to be used within the design optimisation investigation, Chapter 5. Chapter 6 outlines the results of an experimental investigation into separation efficiency when varying the plate spacing. Chapter 7 continuous with design optimisation of the P-TS by applying different surface textures and treatments onto different plate materials. The aim of Part two is to provide an optimum design for the P-TS using industry appropriate materials.

Figure 1.14 shows how the different experimental chapters link together to provide an optimised design for the separation of different dispersions. The overall conclusions are suggested future work resulting from this thesis are provided in Chapter 8.

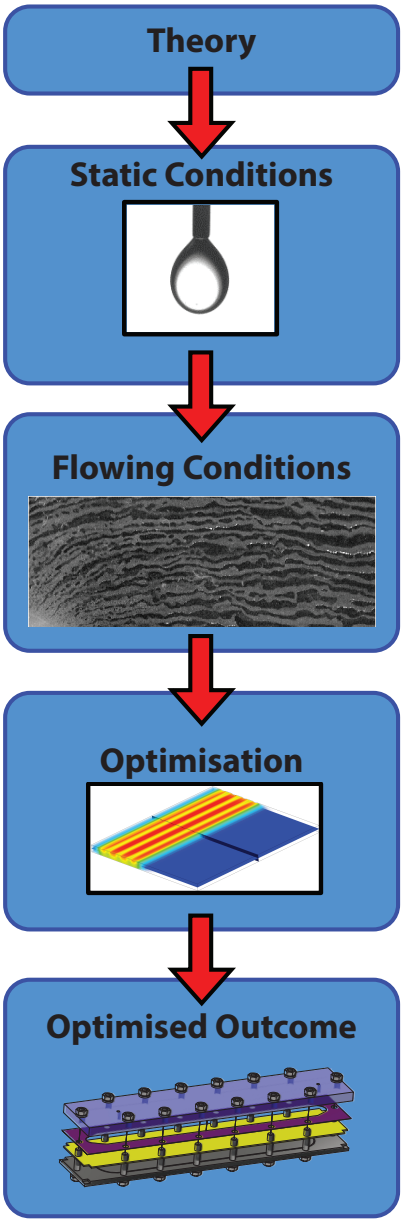

Figure 1.14: Representation of steps undertaken in order to achieve the final research target.

Part I

Coalescence of Static Droplets

CHAPTER 2

Static Flow Coalescence Theory

The development of microfluidic systems requires in-depth analysis of forces that are commonly considered negligible at macroscopic scale. Within this chapter the fundamentals of surface tension and capillarity are discussed with regards to L-L systems and droplet wetting ability on solid plates. The L-L system mimics the behaviour occurring in the centre of the P-TS, where smaller droplets are dispersed within the flow. Whereas, liquid-liquid-solid (L-L-S) environments mimic a droplet settled on the solid walls.

2.1 Mixing Immiscible Liquids

To understand the design requirements of a settling system the dispersion must first be understood. A dispersion in L-L systems consists of two immiscible phases: the continuous and the dispersed[36]. To confirm which liquid will be dispersed the following equation can be used[22]. In Equation 2.1, ϕ is the volume fraction, ρ the density and μ the viscosity. Aqueous and organic phases are represented by Aq and Org.

$$\chi = \frac{\phi_{Org}}{1-\phi_{Aq}}\left(\frac{\rho_{Org}\mu_{Aq}}{\rho_{Aq}\mu_{Org}}\right)^{0.3} \tag{2.1}$$

The magnitude of χ relates directly to the behaviour of the aqueous and organic phases in the following relationship; assuming $\rho_{Org} < \rho_{Aq}$.

$\chi < 0.3$	Organic phase always dispersed.
$\chi = 0.3 - 0.5$	Organic phase probably dispersed.
$\chi = 0.5 - 2.0$	either phase can be dispersed, and phase inversion may occur.
$\chi = 2.0 - 3.3$	Aqueous phase probably dispersed.
$\chi > 3.3$	Aqueous phase always dispersed.

Droplet dispersions can be obtained by three different methods: phase condensation, chemical reaction or mechanical agitation[29]. As mechanical agitation is the most common method for creating dispersions in industry, this will be the method discussed[36].

For the purposes of extraction, the ideal dispersion is an unstable dispersion, that also provides a reasonable amount of time and interfacial area for mass transfer occur between the phases[22]. To create the perfect, unstable dispersion, the droplet size distribution must be correct for the desired system. Mechanical agitators, centrifugal pumps, or rotating impellers create wide droplet distributions, due to the difference in shear velocity between the agitator shaft and the tip of the agitator blade. This type of agitation creates a high percentage of smaller droplets[29]. In contrast, in-line mixers and column agitators, like the pulsed column, provide a uniform shear, creating a narrow droplet distribution ratio. In-line mixers or column agitators provide greater droplet size control, however, are usually more expensive than high shear mixers.

The agitation techniques above are considered industrial processes and are not the most efficient techniques to create a dispersion with a controlled droplet size. For laboratory dispersions many microfluidic devices have been developed, two of the most promising techniques are membrane dispersions and impinging-jets cells. Membrane dispersion creation builds upon the simple injection microfluidic mixing techniques. These techniques involve individual droplets of a controlled size being injected into a flowing continuous phase[37,38]. A membrane dispersion is created by forcing the dispersed phase through a membrane with controlled pore size into the flowing continuous phase, creating multiple, uniform sized droplets[38]. Although membrane dispersions are a promising technique, there are potentially some material compatibility complications with using strong solvents or acidic phases with the membrane material. For this reason membrane dispersions would not be applicable for nuclear solvent extraction; a more likely advanced mixing technique would be impinging-jets cells. The impinging-jets cell has no moving parts and can be manufactured from stainless steel therefore mitigating any maintenance or materials compatibility issues. Dispersions are created by firing two jets together with the immiscible phases meeting within the impingement zone. Droplet size is controlled by varying the

liquid velocity through the jets[39].

It was discussed above that the ideal dispersion for solvent extraction purposes is unstable but provides a reasonable amount of time for mass transfer to occur, one way of influencing the stability time is to consider the density difference of the two liquids. A large density difference, ($\Delta\rho$), between the aqueous and organic phase results in faster separation of the dispersion than a reduced density difference[17,40]; this effect is also taken into consideration in Stoke's law (Equation 1.2). Addition of a dilution agent to provide the desired density and viscosity is a common practice, such as the use of dodecane in the PUREX process. In this case, dodecane is added to Tri-n-butyl Phosphate (TBP) to reduce the density of the organic solution.

If the increased stability provided by altering the density difference between the phases is not sufficient, surfactants can be added to the solution. Surfactants are long-tailed, molecules that dissolve into either the aqueous or the organic phase. Once dissolved the surfactant will naturally diffuse through the liquid until it reaches an interface. In its simplest form an interface is the geometrical surface defining the boundary between two liquids. At the interface the surfactant molecule is captured; this capturing causes a build up of molecules at the interface, that in turn reduces the surface tension of the liquid. The aim of coalescence, from the droplets perspective, is to reduce its overall surface tension; the lowering of the surface tension by the addition of surfactant reduces the need for the droplet to coalesce and therefore stabilising the dispersion. An adverse effect of surfactant addition is the average size of the droplets within the dispersion is likely to reduce, causing an emulsion or creamed dispersion.

2.2 Defining an Interface

The definition of an interface, the geometrical surface defining the boundary between two liquids, implies a perfectly smooth, infinitely thin interface. For the majority of engineering applications this assumption is acceptable as it holds true at macroscopic levels. In reality, at a microscopic scale, separation of immiscible liquids depends on molecular interactions

at the boundary and thermal (Brownian) diffusion of the bulk. This comparison is made in Figure 2.1. The macroscopic scale, Figure 2.1a, takes the contact angle as a given value, and does not explain why contact angles change with different liquid systems. This can only be understood by considering the microscopic scale.

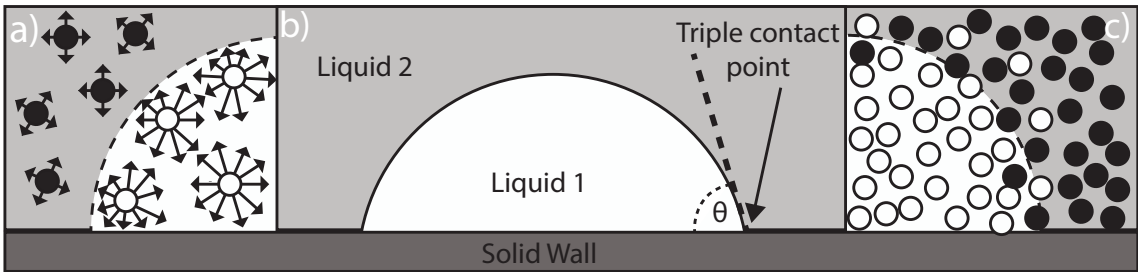

Figure 2.1: Representation of a droplet interface at the macro and microscopic scale, a) Microscopic view of molecule interactions at the interface; b) Microscopic view of the unbalanced forces surrounding molecules at the interface; c) Macroscopic view of a L-L droplet interface.

When considering a droplet on a solid plate, there are three possible environments a molecule can experience. Molecules within the bulk (black circles in Figure 2.1) have equal interactions with all neighbouring molecules, these interactions will primarily be Van der Waals for organics and hydrogen bonds for aqueous liquids. Molecules at the L-L or Liquid-Solid (L-S) interface have half the interactions of those in the bulk. At the L-L interface, molecules will still interact with molecules of the second phase (see Figure 2.1c), however, due to the difference in density of the liquids, the number of interactions across the boundary will not be symmetrical. This dissymmetry causes variations of the energy at the interface, also known as interfacial tension[41].

Figure 2.1a shows how molecules at the surface of a droplet have an imbalance of the forces surrounding them, represented by the variation in arrow size. The attractive forces felt between like molecules are called cohesive forces, the imbalance of cohesive energy surrounding droplets at the interface is typically assumed to be $U/2$ where U is the total cohesive energy. An approximation for surface tension using cohesive energy can be calculated as $\gamma \approx \frac{U}{2\delta^2}$, where γ is the interfacial tension of the liquid and δ is a characteristic value of the molecules size. Therefore, molecules with a small molecular

dimension but high cohesion energy, like mercury, have a very large interfacial tension.

For a droplet to be stable it must seek to reduce this imbalance of energy. As a larger number of molecules at the surface leads to higher cohesion imbalances, one way a droplet can reduce the imbalance is to join with a second droplet in a coalesce event. The coalescence of two droplets increases the volume of the final droplet, and therefore the ratio of molecules in the bulk to those on the surface increases. A second way to reduce cohesion imbalance is for the droplet to spread out on the solid material. When spreading, the molecules are essentially looking for other molecules to correct the force imbalance. Depending on the solid surface on which the droplet is located, this spreading will either result in a flat, pancake shaped droplet or convex, rounded droplet as close to a sphere as possible. By altering the number of molecules at the droplet surface or the droplet surface area, the total surface energy, E, can be predicted using the relationship

$$E = \gamma SA \tag{2.2}$$

where SA is the interfacial surface area.

2.3 Surface and Interfacial Tension Measurement Methods

To help to distinguish between a L-L systems and a liquid-gas (L-G) system, the terminology of interfacial tension is used for L-L and surface tension for L-G. Within this project only the interfacial tension will be considered.

As previously discussed interfacial tension results from an imbalance in energy between molecules at the interface and molecules within the bulk[42]. The quantitative term for measuring the amount of energy per unit surface is commonly expressed in the units mN/m[41]. Another definition of interfacial tension is the amount of energy required to produce a unit area of interface between two immiscible liquids; if the interfacial tension between two liquids is 0 mN/m the liquids are said to be miscible[41,42].

Many techniques have been developed for the measurement of interfacial tension, Drelich *et al.*[43] splits the different techniques into five groups, three of the more com-

mon options are covered below.

2.3.1 Measurements using a microbalance

Interfacial tension measurement techniques using a microbalance use probes such as a plate or ring on the interface to cause a response from the interface, resulting in a measurable force applied onto the probe. There are two main techniques that measure interfacial tension by measuring this response, the Wilhelmy plate and Du Noüy ring method.

The Wilhelmy plate method (Figure 2.2) equates excess energy per area to force per length which is numerically equal to interfacial tension in Equation 2.3[43].

$$\gamma = \frac{F}{perimeter * cos\theta} \tag{2.3}$$

where the force, F, is the force applied onto the plate by the interface. This force is measured by bringing the plate into contact with the interface, ensuring the plate is completely wetted by the liquid, as shown in Figure 2.2. When the plate contacts the surface, the liquid at the interface rises, forming a meniscus due to capillary forces. The interaction between the liquid and the plate increases the interfacial tension, pulling the plate downwards towards the liquid. This force will be measureable on the microbalance, as the force is equal to the weight of the liquid in the meniscus above the plane of the original interface[43]. P in Equation 2.3, is the perimeter of the 3 phase contact line, in this case the perimeter is equal to $2(L + w)$.

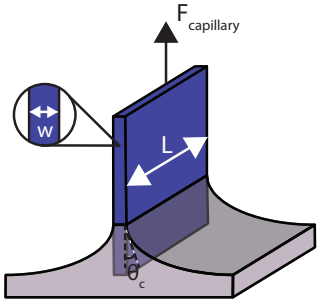

Figure 2.2: Wilhelmy plate method for the measurement of interfacial tension.

The Du Noüy ring method measures the force required to pull a wire ring off the

interface[44,45], shown in Figure 2.3. A wire of radius, R, and thickness, r, where $\frac{R}{30} > r > \frac{R}{60}$ [46], is introduced to the the liquid surface. As with the Wilhelmy plate method, the interface responds by forming a meniscus. As the Du Noüy method is solely a detachment technique, where force measured is the force required to separate the probe from the interface, a correction factor f must be applied to Equation 2.3[45]. f varies from 0.75 - 1.05 depending R and r, the angle between the meniscus and the ring (the wettability of the ring), θ, and the difference in density between the liquids, $\Delta\rho$, and can be calculated using Equation 2.4[45]. The perimeter in Equation 2.3 is twice the circumference of the ring, $4\pi R$.

$$f = 0.725 + \left(\frac{9.074 \times 10^{-4} F}{\pi^3 \Delta\rho g R^3} - \frac{1.079 r}{R} + 0.04534\right)^{1/2} \tag{2.4}$$

Equation 2.4, applies for the range $0.045 \leq \frac{\Delta\rho g R^3}{F} \leq 7.5$[45], where g is the force due to gravity.

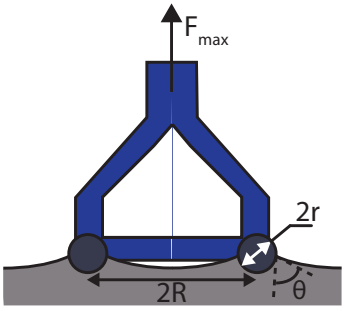

Figure 2.3: Du Noüy ring method for the measurement of interfacial tension.

The Wilhelmy plate method has the advantage that it can be used both static, the plate remains in contact with the liquid for the entire measurement, and detached unlike the Du Noüy method which is solely a detachment technique. The Wilhelmy plate method is also the favoured method between the two for interfacial tension measurements, as the Du Noüy method is not as reliable in L-L systems due to diffculities in achieveing the correct methodology[42].

For both methods the probe is usually manufactured out of a platinum-iridium alloy or platinum. The Wilhelmy plate method provides more options for probe materials as

glass and steel plates have also been used depending on the hydrophobic relationship of the liquid with the plate material[47].

A major source of error in both systems is contamination of the probe. For both methods, this can be combated by thorough cleaning of the probe followed by flame treating; however, thorough cleaning of the Du Noüy ring can cause deformation of the ring. This is the most common source of error for the Du Noüy method.

2.3.2 Capillary rise

The oldest technique for measuring interfacial tension is the capillary rise technique. For the most part this technique has been replaced by more advanced computational methods, however, it still provides very accurate results.

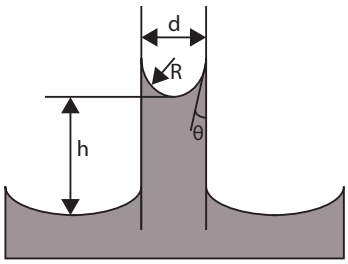

Figure 2.4: Capillary rise method for the measurement of interfacial tension.

A round glass tube of known diameter d is placed just below the liquid surface, as shown in Figure 2.4[48]. Due to capillary forces, the liquid climbs the inside of the tube forming a meniscus of radius,R. When d is smaller than the height of the meniscus, h, the meniscus will be spherical in shape. From this, Equation 2.5 can be used to calculate the surface tension[43,48].

$$\gamma = \frac{\Delta \rho g h R}{2 cos\theta} \tag{2.5}$$

An advantage of this method over the microbalance methods is that glass is easier to decontaminate than metal probes. However, being limited to only the use of glass can be detrimental as many liquids will perfectly wet the tube, causing $\theta = 0$. If $\theta = 0$ the

meniscus will no longer be spherical. In this case, Equation 2.6 can be applied[48]

$$\frac{1}{2}\Delta\rho g R h\left(1+\frac{R}{3h}-0.1288\frac{R^2}{h^2}+0.1312\frac{R^3}{h^3}\right) \tag{2.6}$$

The largest source of error for this method is not having an accurate measurement of diameter, d, as errors can occur in the fabrication of uniform bore tubes[43]. The capillary rise method can provide the most precise measurements of any method discussed within this section for surface tension, however, is not recommended for interfacial tension measurements[43].

2.3.3 Measurement for gravity distorted droplets

A droplet in zero gravity will form a spherical shape to reduce excess energy at the interface. When attached to an object under gravity, the shape will distort into a pendant drop or sessile droplet. A sessile droplet is a static droplet pressing against a large solid surface, whereas a pendant drop is a static droplet pulling away from a small solid surface, like a needle tip. The sessile droplet can be used to calculate interfacial tension, however, it is more common to use a pendant drop as more computational techniques have been developed to improve the pendant drop method[42,49].

Table 2.1: Summary of interfacial tension measurements[42]

Method	**Accuracy mN/m**	**Suitability for L-L systems**
Wilhelmy Plate	~ 0.1	Good
Du Noüy Ring	~ 0.1	Reduced accuracy
Capillary Rise	$<<0.1$	Very good, experimentally difficult
Pendant Drop	$\sim 0.1^*$	Very good

Berry *et al.*[42] suggest that although the accuracy of Wilhelmy Plate, Du Noüy and pendant drop are around $0.1\,mN/m$, the pendant drop method has the best suitability for two phase, L-L systems as shown in Table 2.1. Therefore the pendant drop method will be used in this study and will be discussed in more detail than other methods.

2.3.3.1 Pendant drop

Pendant drop interfacial tension measurements are found through an iterative fitting of the Young-Laplace equation to an axisymmetric droplet. The first interfacial tension measurements performed on a pendant drop was conducted in 1881 by Worthington[50]. Worthinton calculated the pressure drop across the interface of a pendant drop suspended from a glass tube[50,51]. To aid in this solution, the Young-Laplace equation, shown in Equation 2.7, was used where, R_1 and R_2 are the radii of curvature and $\Delta P \equiv P_{in} - P_{out}$ the Laplace pressure across the interface[42,50].

$$\gamma\left(\frac{1}{R_1} + \frac{1}{R_2}\right) = \Delta P \tag{2.7}$$

Later, Bashford and Adams[52] produced comprehensive tables of solutions to the Young-Laplace equation by expressing Equation 2.7 in terms of cylindrical coordintates r and z, as well as φ, the tangent angle, shown in Figure 2.5a. They showed that the shape of the pendant drop can be related to a dimensionless quantity β, defined as $\beta \equiv \frac{\Delta\rho\frac{d}{2}^2}{\gamma}$, where d is the droplet diameter, as shown in Figure 2.5b. Originally, β was presented as an "abstract number"[52], however, it was later proved as a measure of the relationship between gravitational force and interfacial forces[42,53]. After this discovery it was named the Bond number by Merrington and Richardson[53] in 1947, it can also be referenced as the Eötvös number in literature[54].

Use of the Bond number was intended to increase the reproducibility of interfacial tension values, however the process to determine the Bond number accurately proved difficult[43]. Andreas *et al.*[55] developed an approach to improve this process in 1940. They proposed a method that required two experimentally measured parameters from the pendant drop, d the diameter at the widest point, and d_{apex} the diameter l distance from the apex, as shown in Figure 2.5a[55]. These values can be equated to interfacial tension using Equation 2.8.

$$\gamma = \frac{\Delta\rho g d^2}{H} \tag{2.8}$$

where H is depends on the shape factor, $S = \frac{d_{apex}}{d}$. Tables relating $1/H$ to S can be found in several references[47,56] or H can be calculated using:[57].

$$\frac{1}{H} = \frac{B_4}{S^A} + B_3 S^3 - B_2 S^2 + B_1 S - B_0 \tag{2.9}$$

where $B_i (i = 0, 1, 2, 3, 4)$ and A are empirical constants for a defined range of S. Values of B_i and A are published in varies data collections, with the most extensive being provided by Misak, 1968[57].

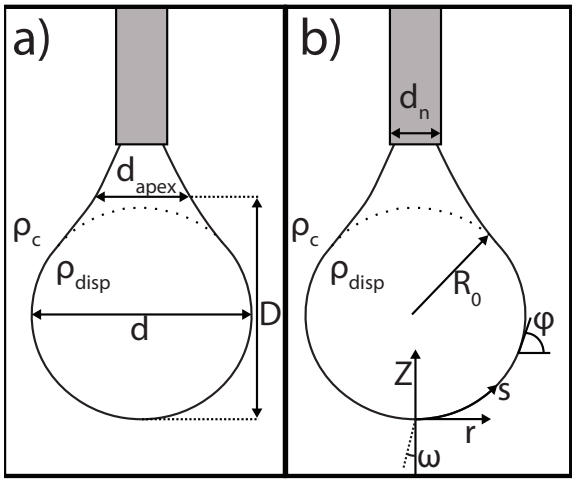

Figure 2.5: Original measurements required for the Pendant drop method. a) Measurements required for interfacial tension using the Andreas simplification. b) Measurements required to solve Young-Laplace equation using cylindrical coordinates.

With this simple method of measuring interfacial tension, the needle diameter must be $<0.5d$ but not too small otherwise there is a loss in precision in the measurement of diameter, d_{apex}.

In 1983 two articles were published that developed a method to computationally combine existing data, greatly improving the precision of measurements using the pendant drop technique[58,59]. After this breakthrough, and with the increased accessibility to enhanced computational power, computational methods have been continually refined and verified for different environments into the technique used today[60–62]. Improvements over this time showed improved accuracy for measurements with a low Bond number, however, this is still considered a major source of error with this method. Experimentally this can

be minimised by choosing a system with a large $\Delta\rho$ and by ensuring the diameter, d, of the pendant drop is as large as possible, without necking (discussed in Section 3.2.1 [42]).

Berry *et al.*[42] conducted a sensitivity test on a series of water droplets in air formed by increasing diameter needle tips, and therefore, with increasing Bond numbers. It was found that for low known bond numbers (d = 1.65 mm and β = 0.09), the calculated Bond number using current methods varied between 0.06 - 0.11. This highlighted the requirement for a secondary non-dimensional number to provide a variation of the Bond number, independent to the needle diameter. This value was given the name, the Worthington number. The Worthington number, Wo, is related to the droplet volume, V_d and theoretical maximum drop volume V_{max}, as shown in Equation 2.10.

$$Wo = \frac{V_d}{V_{max}} = \frac{\Delta\rho g V_d}{\pi\gamma d_n} \tag{2.10}$$

where d_n is the diameter of the needle tip, shown in Figure 2.5a and $V_d = \pi \int \bar{r}^2 sin\varphi \, d\bar{s}$, r, s and φ are shown in Figure 2.5b.

2.4 Interfacial Tension Dependence on Temperature

The value of interfacial tension of a liquid can vary depending on temperature [41]. An equation to describe this property was first published in 1886 by Eötvö. Equation 2.11 was formulated on the assumption that interfacial tension, γ, tends to zero when the temperature, T, reaches a critical value, T_{crit} [41].

$$\gamma = \left(\frac{1}{\upsilon_D}\right)^{\frac{2}{3}} (T - T_{crit}) \tag{2.11}$$

where υ_D is the molar volume of the dispersed liquid.

In 1915 and 1945, Equation 2.11 was improved to become the Katayama-Guggenheim equation [63].

$$\gamma = \gamma^* \left(1 - \frac{T}{T_{crit}}\right)^n \tag{2.12}$$

where γ^* is a constant for each liquid and n is an empirical factor ($\frac{11}{9}$ for organics). Equation 2.12 provides high accuracy for organic liquids but not aqueous. If temperature dependence is not of high importance, n can be taken as one and Equation 2.12 becomes;

$$\gamma = \gamma^*(1 + \alpha T) \tag{2.13}$$

where α is a constant that can be found in literature[41]. The value of α is always negative, giving rise to the relationship: interfacial tension decreases when temperature increases.

With new measurement techniques for interfacial tension, it can often be easier to measure γ_0 and T_0, shown in Figure 2.6. This eliminates the need for the value α which may not be reported for all liquids. If using this method Equation 2.13 becomes;

$$\gamma = \gamma_0(1 + \zeta(T - T_0)) \tag{2.14}$$

where $\zeta = \frac{1}{T_c - T_0}$ and $\gamma_0 = \gamma^* \frac{T - c - T_0}{T_c}$

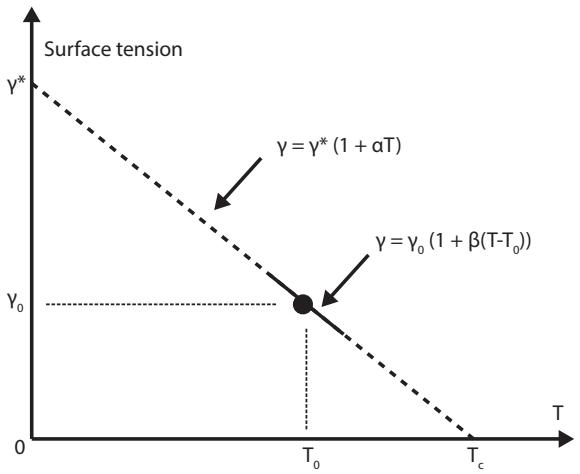

Figure 2.6: Effect of temperature on interfacial tension[41].

The relationship between temperature and interfacial tension can be seen in Figure 2.6, which also shows how Equations 2.14 and 2.13 can be used together.

A phenomenon that arises from the negative dependence on temperature is called Marangoni convection or thermocapillar instabilities[64]. Marangoni convection arises when part of the interface is heated via convection, radiation or conduction, causing a temper-

ature gradient across the interface. This imbalance of temperature in turn causes an imbalance in interfacial tension. The result of this imbalance is movement of liquid along the interface from warmer, low interfacial tension areas to cooler, high interfacial tension areas. This movement often propagates into the bulk liquid causing doughnut like convection currents within a static droplet.

Practically, this convection flow has little effect on coalescence when the temperature source is temporary, as the convection will reach an equilibrium with the temperature and movement will slow. Whereas, if the temperature source is permanent or changing, like heat within an industrial plant or from the heat of radiation, the change in temperature across the plant must be taken into consideration as changes in interfacial tension could effect separation efficiency.

2.5 Contact Angle

As not all droplets are perfectly spherical, research has shown how external factors effect the form of the droplet. The largest external factor effecting droplet formation is the material on which the droplet sits. When an aqueous liquid sits on a hydrophobic material, or an organic on a hydrophilic material, the droplet is likely to relax and spread. A liquid will take the shape that expels the least energy; spreading, also known as wetting, is when a droplet lays flat on a material with a contact angle close to 0^o, shown in Figure 2.7a.

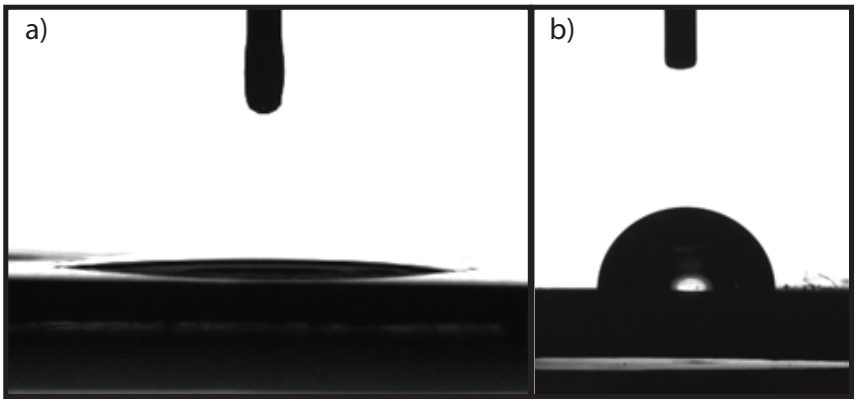

Figure 2.7: Sessile water droplet on a) stainless steel b) PTFE.

The opposite to spreading/wetting is beading. Beading, shown in Figure 2.7b, occurs when an aqueous/organic liquid comes into contact with a hydrophobic/hydrophilic material, respectively. The bead is formed as the lowest energy environment for the droplet is within the bulk liquid, due to the repelling nature of the material. This material repulsion and attraction is due to adhesion and cohesion[65]. Adhesion is the interaction between the liquid molecules and the material, whereas, cohesion is the interaction between the liquid molecules themselves[65]. When adhesion is greater than cohesion the liquid will spread on the material.

Härth and Schubert[66] published a very detailed paper on force balances across droplets with different spreading dynamics; they take into consideration capillary force, gravitational force and viscous frictional force. They define that if the radius of the drop is smaller than the capillary length then the droplet will be spherically capped as capillary forces dominate[66]. Capillary length is defined in Equation 2.15, where l_c is the capillary length and γ_D the dispersed phase interfacial tension. For the droplet to spread completely onto the plate, its radius must be larger than the capillary length; in this situation gravitational forces dominate.

$$l_c = \sqrt{\frac{\gamma_D}{\rho g}} \tag{2.15}$$

Balancing the forces acting upon a droplet and utilising previous models[66,67] found that Equations 2.16 and 2.17 were true for complete wetting and partially wetting (beading) droplets.

$$\gamma_D \frac{16V^2}{\pi r^5} + \frac{4\rho g V^2}{3\pi r^3} - \frac{\eta \dot{r} r^6}{\lambda V^2} = 0 \tag{2.16}$$

Complete wetting

$$2\pi r\left(S + \gamma_D \frac{8V^2}{\pi^2 r^6}\right) + \frac{4\rho g V^2}{3\pi r^3} - \frac{\eta \dot{r} r^6}{\lambda V^2} = 0 \tag{2.17}$$

Partial wetting

V	Drop volume
H	Frictional coefficient
$\dot{r}$	Rate of spreading of at the 3 phase boundary
λ	Dimensionless shape factor
S	Spreading dynamic ($S = \gamma_S - \gamma_D - \gamma_{SD}$)

Härth and Schubert[66] go on to derive an equation defining a correlation between the radius of the droplet and spreading time from complete and partial spreading (Equation 2.18 and 2.19)

$$r(t) = \left[\left(\gamma_d \frac{96\lambda V^4}{\pi^2 \eta}(t+t_0)^2 + \left(\frac{\lambda(t+t_0)}{\eta}\right)^{\frac{2}{3}}\left(\frac{24\rho g V^{\frac{8}{3}}}{7.96^{\frac{1}{3}}}\pi^{\frac{4}{3}}\gamma_d^{\frac{1}{3}}\right)\right]^{\frac{1}{6}} \tag{2.18}$$

Complete wetting

$$r(t) = r_e\left[1 - e^{\left(-\left(\frac{2\gamma_d}{r_e^{12}} + \frac{\rho g}{9r_e^{10}}\right)\frac{24\lambda V^4(t+t_0)}{\pi^2\eta}\right)}\right]^{\frac{1}{6}} \tag{2.19}$$

Partial wetting

where t_0 accounts for experimental time delay and r_e is the equilibrium contact radius. With Equations 2.18 and 2.19, any droplet can be described at any moment during the spreading time.

Härth and Schubert[66] took into consideration frictional force, however, did not consider the roughness of the surface on which the droplets sits. Figure 2.8 shows three separate situations a settled droplet can experience. These situations are explained in a study completed by Whyman *et al.*[68].

Figure 2.8a shows the situation of a droplet on a flat surface, this situation is where the well-known Young-Dupre equation, Equation 2.20, holds true.

$$cos\theta_e = \frac{\gamma_{SC} - \gamma_{SD}}{\gamma_{CD}} \tag{2.20}$$

where $cos\theta_e$ is the equilibrium contact angle and, γ_{SC}, γ_{SD}, γ_{CD} are the surface tension values between the solid and the continuous phase, solid and the dispersed phase and continuous and dispersed phases, respectively, as represented by the subscript lettering.

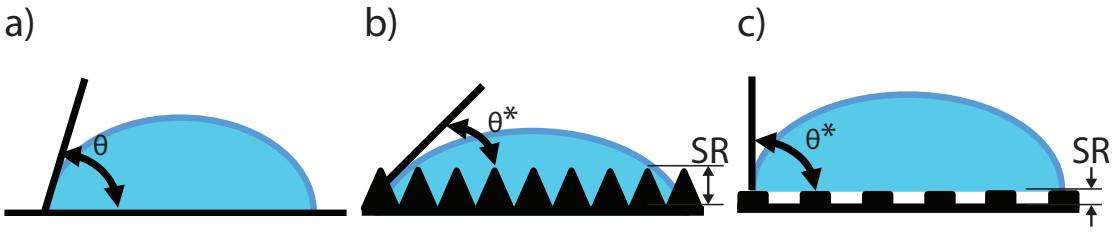

Figure 2.8: Different wetting regimes. a) Flat, b) Rough (Wenzel), c) Rough with air (Cassie-Baxter)[68].

Figure 2.8b shows the situation of a rough surface with a spreading droplet, known as the Wenzel regime. Here the surface roughness, shown as SR in Figure 2.8 is > 1. Contact angles for droplets in the Wenzel regime are calculated using Equation 2.21, where θ^* is the apparent contact angle as the true contact angle cannot be directly measured.

$$cos\theta^* = SRcos\theta = f\left(\frac{\gamma_{SC} - \gamma_{SD}}{\gamma_{CD}}\right) \tag{2.21}$$

Finally, 2.8c shows a rough surface material ($f > 1$) with a beading droplet. This situation is called the Cassie-Baxter regime, described by Equation 2.22. Here interfacial tension is proportioned (ϕ_i) between the solid/continuous interaction, $\gamma_{i,SC}$, and the solid/dispersed interaction, $\gamma_{i,SD}$.

$$cos\theta^* = \Sigma\phi_i(\gamma_{i,SC} - \gamma_{i,SD}) \tag{2.22}$$

Most commonly, two phases are present and so Equation 2.22 can be written as Equation 2.23.

$$cos\theta^* = \phi_1(\gamma_{1,SC} - \gamma_{1,SD}) + (1 - \phi_1(\gamma_{2,SC} - \gamma_{2,SD}) \tag{2.23}$$

2.6 Coalescing Droplets

When droplet interfaces collide, they combine to become a single droplet with larger volume. This mechanism is known as coalescence. Coalescence is the most common

mechanism of dispersion breakdown and phase separation. For this reason, coalescence of droplets will be discussed more than the other breakdown mechanisms. It is believed this is the principle reason for separation within a micro-separator.

Dispersed droplets within a continuous phase have a finite lifetime before two separate phases are formed through coalescence[25]. The direction a droplet travels during the separation process, depends on the difference in density of the two liquids in the system. A dispersed droplet travelling through a liquid will continuously accelerate until the drag force and gravitational force balance with its buoyancy, at which point the droplet will reach terminal velocity.

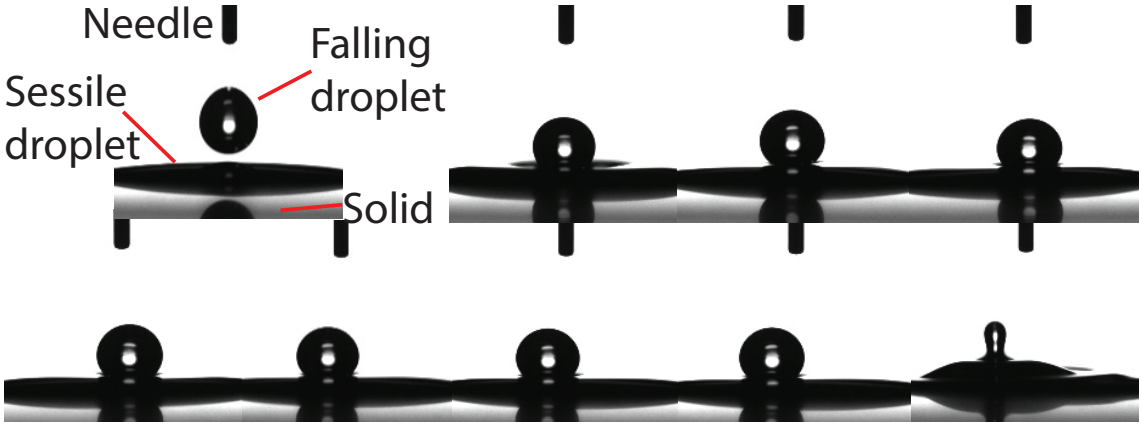

Figure 2.9: Coalescence progression of a falling droplet onto a sessile droplet on SS. Each frame is equal to 1×10^{-6}s.

When two droplets meet, or a droplet meets a surface coated by the same liquid, such as in Figure 2.9, they will coalesce to reduce their overall surface energy. This is more favourable for each droplet as previously state in Section 2.2[41]. Figure 2.9 shows a coalescence event which occurred much less than a second, however, droplets can sometimes be in close proximity for several hours both a coalescence event occurs[41].

The first stage of coalescence is the collision, Figure 2.10a. This can sometimes result in the droplet bouncing apart, however, if the surface characteristics are correct the continuous phase begins to drain from between the colliding droplets, forcing the two together. After the initial collision a planar region is formed as a result of the increased surface tension experienced by the molecules of the different droplets post collision, Figure 2.10b.

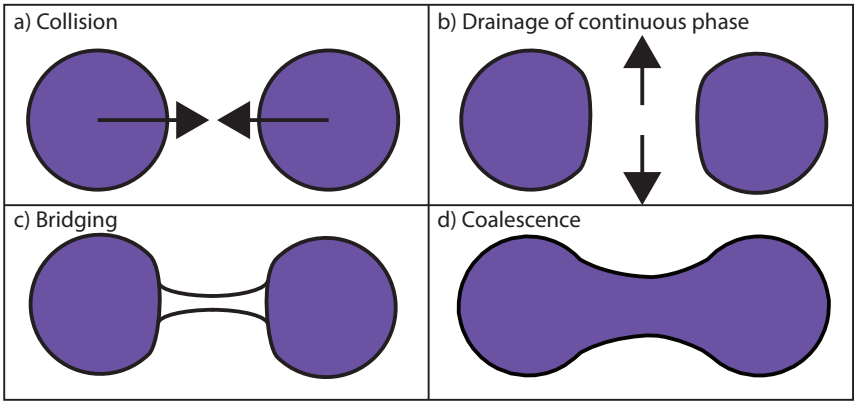

Figure 2.10: Diagram of the four stages of coalescence

These molecules are attracted towards each other forming a neck or bridge, Figure 2.10c. This bridging mechanisms can also be a result of the roughness of the surface material if the coalescence is occurring on a surface[69]. Once the neck is formed, the development of the final droplet is determined by viscous, inertial and surface forces[69].

The Reynolds number of this flow can be estimated by Equation 2.24.

$$Re = \frac{\gamma R_m}{\rho \nu^2} \tag{2.24}$$

where γ remains as interfacial tension, ρ_d the density of the dispersed phase, $\nu = \frac{\mu}{\rho}$ the kinematic viscosity and R_m the meniscus radius, shown in Figure 2.11.

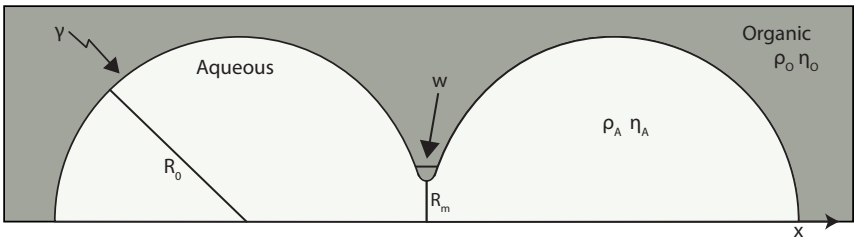

Figure 2.11: Surface profile of two coalescing drops of radius R_0, viscosity η and IFT, γ. The bridging radius R_m has width of w

Within Figure 2.11 it can be seen that the two droplets are identical, sharing the same density and viscosity, whereas, the continuous organic phase has different properties. The difference in these properties determines the length of time (t) the meniscus of radius $R_m(t)$ with width $w(t)$ take to form. The extent at which variations in droplet properties

effects coalescence rates is investigated further in Section 3.3[69].

CHAPTER 3

Effect of pH and Heavy Metal Ion Concentration on the Coalescence Rate of Static Droplets

To develop high efficiency settling technologies, a greater understanding of the coalescing interface is required. Traditionally it is understood that for a two phase, immiscible system with low viscosity fluids, the coalescence rate of droplets is controlled by the overall droplet inertia and the interfacial tension[70]. However, with most microfluidic devices operating within a laminar flow region, it is unknown to what extent other factors, such as wall effects or ion concentration, will influence coalescence rates.

As such, a study of contact angle and interfacial tension in a two phase, temperature controlled, immiscible system was completed. The study used tri-n-butyl phosphate (TBP) with an n-dodecane diluent, this system was chosen to represent the nuclear reprocessing process PUREX (plutonium, uranium redox extraction). The TBP volume percentages used within the PUREX process were 20 v% to 30 v% TBP. PUREX uses the ratio between TBP and the n-dodecane diluent to control process viscosity and density. Cerium (III) nitrate was used as the heavy metal ion (HMI) as it is not extractable with TBP in this oxidation state, and therefore mass transfer kinetics do not effect the results found. The effect of aqueous phase metal ion loading was observed for contact angle, interfacial tension and coalescence rate.

3.1 Contact Angle

Contact angle, as discussed previously, is a measure of how the liquid and surface material interact with each other. The droplet environments experienced within the P-TS will be on the plate materials; stainless steel, acrylic (PMMA) or both. For this reason experiments were completed on both surface materials with an organic continuous phase and aqueous dispersed phase, and repeated with continuous and dispersed phases reversed.

Contact angle experiments were conducted to find the influence of pH or HMI con-

centration ([HMI]) on the hydrodynamic behaviour of fluids within the separator. It has previously been proposed that the relationship between the fluid and wall material has the largest effect on the separation efficiencies experienced within a P-TS[31,33]. Here, we propose that varying the [HMI] or pH ($[H^+]$), a common occurrence throughout a solvent extraction flow sheet, could potentially alter the effectiveness of the P-TS. This alteration could result in potential design alterations to the separator to ensure consistent separation efficiency throughout the entire flow sheet.

The contact time of a droplet with the device wall will be brief, as droplets are flowing in a confined system and are unlikely to settle and flatten like a stationary droplet. As such the instantaneous contact angle was measured.

3.1.1 Methodology

All reagents used were 99% purity or higher from Fisher Scientific (Loughborough). All water used is ultra pure, deionized water from a MilliQ water purification system by Millipore (Millipore, Watford, UK). Organic phases were pre-equilibrated with 3 M HNO_3 or 3 M $Ce(NO_3)_3$ prior to measurements. Pre-equilibration is used to reduce the time taken for the system to reach equilibrium. Contact of the two phases was achieved via five minutes of high speed stirring and five minutes centrifugation in the Compact Star CS4 centrifuge. All test plate materials and glassware were prepared by cleaning with acetone, ultrasonic bath and compressed air spray to remove dust between each change of dispersed or continuous phase.

Contact angle measurements were taken using a Biolin Scientific optical tensiometer. Attension Theta software computationally tracked the outer edge of the sessile droplet. Within the software, this outline is related to a user input baseline, and the angle at the point of intersect is taken as the contact angle. Measurements taken are shown in Figure 3.1.

Initial calibration was completed using a 4 mm calibration ball submerged in the desired continuous phase. Camera positioning was altered to point up or down towards the sample area, 2^o off horizontal to ensure the reflection of the droplet in the material was captured

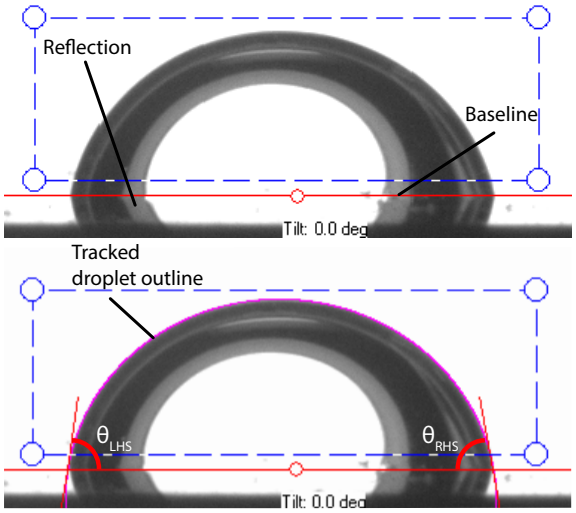

Figure 3.1: Contact angle measurement procedure where $\theta_{LHS/RHS}$ are the left and right hand contact angles, respectively.

(Figure 3.1). This reflection allows for the baseline of the droplet to be clearly defined allowing for more repeatable results. Once the camera was moved to its final position the calibration was reconfirmed using the known diameter needle width.

The continuous phase and test material were contained in an optical glass cuvette. A syringe of the dispersed phase, orientated perpendicular to the test material was positioned and the cuvette sealed from the environment. The experimental set-up is shown in Figure 3.2a. The dispersed phase was introduced to the continuous phase as a sessile droplet using a screw thread Hamilton gas tight syringe and gauge 25 straight or hooked needle tip, see Figures 3.2b and c. A hooked needle, shown in Figure 3.2c, was used for *in situ* testing when the dispersed phase density was less than that of the continuous phase. In this situation, the test material was held upside down in a 3D printed holder. Using this set up, the Attension Theta software is set to vertically flip the image. All experiments were conducted at approximately 20 ℃.

A droplet at its largest volume was released from the syringe to fall/rise onto the test plate material. The instantaneous contact angle was recorded as soon as the droplet remained stationary. The contact angle and droplet volume was measured in triplicate. Droplet volume was controlled using a screw thread syringe.

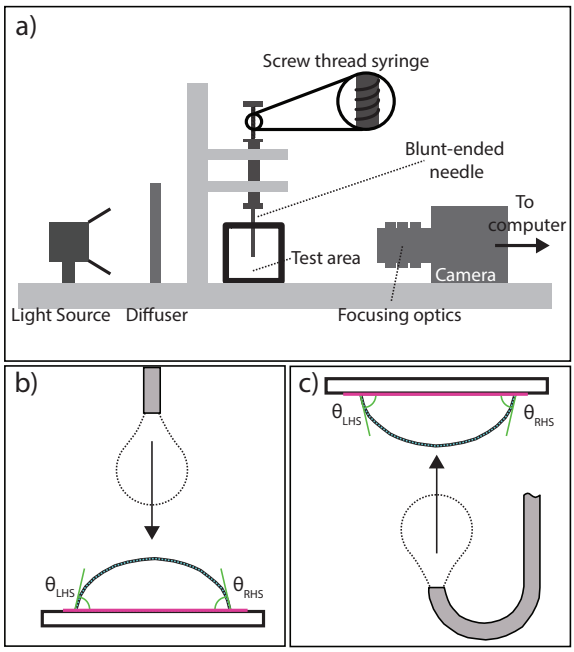

Figure 3.2: Contact angle experimental set-up, a) Set up of optical tensiometer for contact angle measurements. b) Test area set up for heavy phase as dispersed droplet. c) Test area set up for light phase as dispersed droplet.

Two control experiments were conducted. The first control experiment was conducted using increasing concentrations of nitric acid dispersed phases (1 M, 3 M, 5 M HNO_3), with dispersed phase measurements of TBP ligand with varying dodecane dilutions. Dodecane dilutions used were 100 v%, 90 v%, 80 v% and 70 v%, with TBP making up the remaining volume. The second control experiment reversed the dispersed and continuous phase so that increasing TBP concentrations within dodecane were the dispersed phases and 1 M, 3 M, 5 M HNO_3 the continuous phases. All experiments were conducted on both PMMA and SS.

This experiment was repeated with HMI introduced. Here, increasing concentrations of cerium (III) nitrate dispersed/continuous phases (1 M, 3 M, 5 M $Ce(NO_3)_3$) were used. The organic phase used for the HMI experiments were the same as those used in the control experiment (100 v%, 90 v%, 80 v%, 70 v% dodecane). As with the control experiments the continuous and disperse phases were reversed and the measurements repeated on both stainless steel and PMMA. Measurements of 5 M $Ce(NO_3)_3$ were not taken due to similar

refractive indexes of the two phases.

3.1.2 Results and discussion

3.1.2.1 Aqueous dispersed in bulk organic

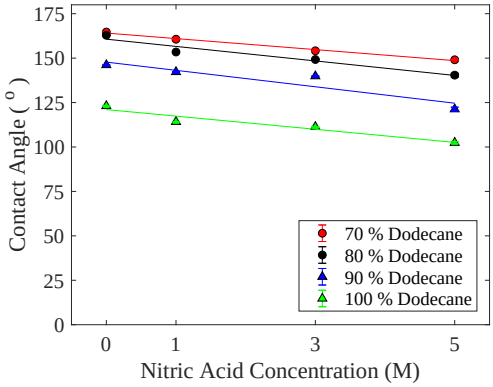

(a) Dispersed phase: Nitric acid.
Test material: PMMA

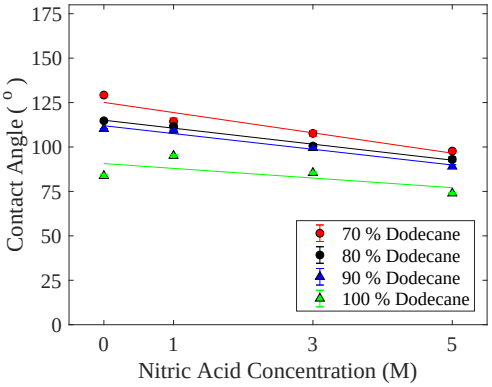

(b) Dispersed phase: Nitric acid.
Test material: Stainless steel

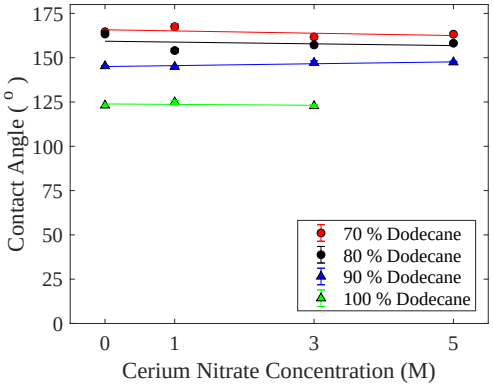

(c) Dispersed phase: Cerium nitrate.
Test material: PMMA

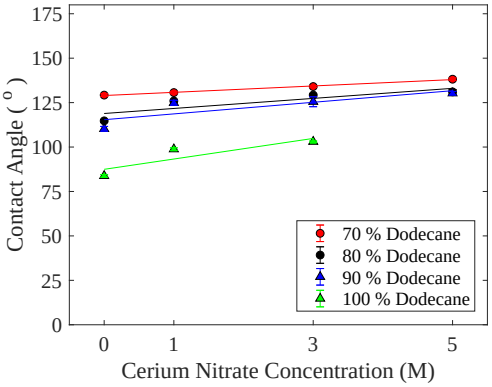

(d) Dispersed phase: Cerium nitrate.
Test material: Stainless steel

Figure 3.3: Contact angle measurements for aqueous dispersed systems in TBP/dodecane continuous phases for comparison of pH and HMI variation effects. 0M measurements substituted the dispersed phase with pure water. Lines are used to guide the eye.

The results from the HMI-free aqueous in organic experiments are shown in Figures 3.3a and b. No strong relationship within this data was observed. The most significant results are the relatively high contact angles observed on the hydrophilic, SS plate. It was assumed that the angles would be less than 90^o, however, here it is found that an

organic continuous phase alters the hydrophilic behaviour on the SS plate. The results of the HMI-free experiments show an average decrease in contact angle of 27.7 % with the material change from PMMA to stainless steel. The results from the HMI aqueous in organic experiment, shown in Figures 3.3c and d, also follow this trend with an average decrease in contact angle of 18.8 %. Again, it was expected that the change in contact angle from the hydrophobic to hydrophilic plate material would be more significant as usually the aqueous phase contact angle on a hydrophilic material is less that 90^o.[66].

3.1.2.2 Organic dispersed in bulk aqueous

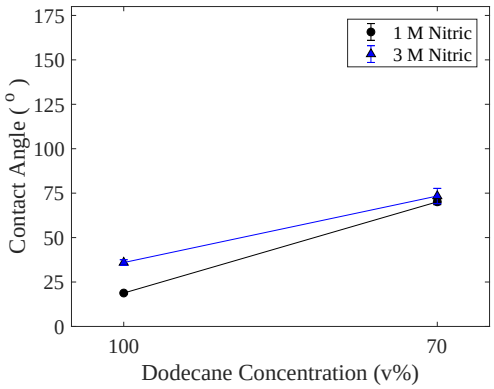

(a) Dispersed phase: 30 v% TBP in Dodecane. Test material: PMMA

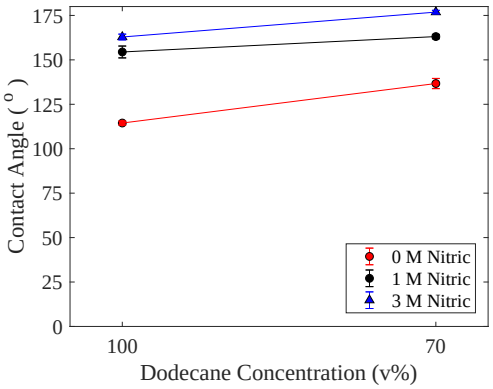

(b) Dispersed phase: 30 v% TBP in Dodecane. Test material: Stainless steel

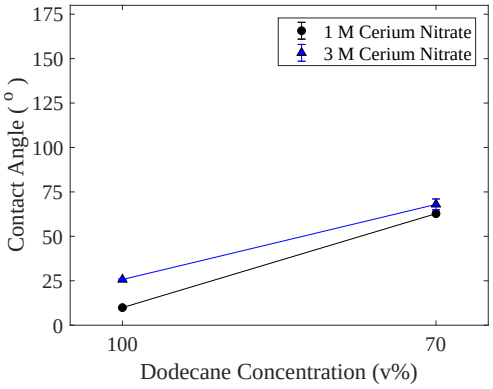

(c) Dispersed phase: 30 v% TBP in Dodecane. Test material: PMMA

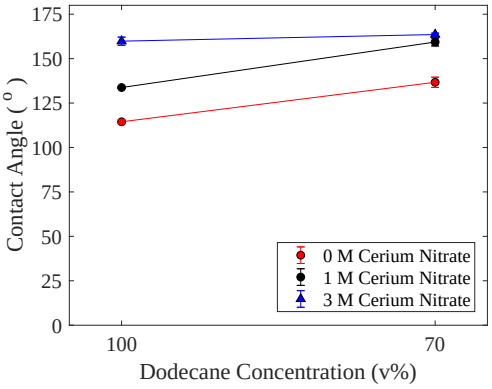

(d) Dispersed phase: 30 v% TBP in Dodecane. Test material: Stainless steel

Figure 3.4: Contact angle measurements for organic dispersed systems in acidic continuous phases for comparison of pH and HMI variation effects. 0M measurements substituted the dispersed phase with pure water.Fitted lines are used to guide the eye.

The results from the HMI-free organic in aqueous experiment, are shown in Figures 3.4a and b. Unlike the aqueous in organic experiments, results of these experiments show a large average increase in contact angle with the material change from PMMA to SS. These are calculated as a 136 % increase for the 30 v% dodecane system and 537 % for the 100 v% dodecane system. This magnitude of change is expected when moving from hydrophilic to hydrophobic systems[66]. As the magnitude of change was so large within the aqueous bulk system, this therefore, supports the hypothesis that an interaction between the organic continuous phase and the stainless steel test material caused the increase in contact angle observed in the aqueous in organic test case. The results from the HMI organic in aqueous experiment, shown in Figures 3.4c and d, also follow this trend with an average increase in contact angle of 147 % and 904 % for the 30 and 100 v% dodecane systems respectively. However, as aqueous dispersed data, no strong relationship was found.

3.1.3 Conclusion

It was found that the hydrophilic nature of SS in air is reduced in a bulk organic environment. However, when the bulk phase is changed to aqueous the SS behaviour is as expected. This shows that although SS is hydrophilic, its hydrophobic behaviour can be altered by organic contamination. In terms of separator design, it has been suggested in previous studies that the cause of separation in the P-TS is a result of the different fluid interactions with the hydrophobic and hydrophilic walls[31–33,35]. Using the results found within this study, if the previous statement is correct, it would be found that the separation efficiency of a P-TS is reduced when the continuous phase of a dispersion is organic phase. No significant relationship was observed with increasing [HMI].

To fully understand if separation efficiency will increase or decrease with an increased contact angle of either the dispersed or continuous phase either non-static investigations or, as with coalescer design (described in Section 1.3.3) computational fluid modelling would have to be completed.

3.2 Interfacial Tension

Surface tension of a liquid is a measure of cohesion strength between the liquid molecules. Interfacial tension between fluids effects the ease at which droplets coalescence and separate. Continuing from the contact angle investigations, the effect of pH and [HMI] on interfacial tension was investigated. Interfacial tension variations will mainly affect droplets that have not contacted on either plate, these droplets are likely to coalescence with a slowed droplet, adhered onto a wall. Again, it is proposed that a change in the interfacial tension with varying heavy metal ion concentration or pH could effect the efficiency of a microfluidic separator throughout a solvent extraction plant. This change would not be of concern to larger separation units as wall effects are less apparent.

3.2.1 Methodology

Reagents and methods used to prepare solutions and glassware are as described in Section 3.1.1.

Interfacial tenisons were measured using the pendant drop method, explained in Section 2.3.3.1, and shown in Figure 3.5a, on a Biolin Scientific optical tensiometer. Attention Theta software running the Young - Laplace model was used for data analysis. The measurements used by the software are shown in Figure 3.5b [42].

Initial calibration was completed by measuring the interfacial tension of a pendant drop of water in an air continuous phase (72.86 $mN.m^{-1}$) [71]. It was observed that changing continuous phase caused a difference in measurement due to a change in the refractive index. Calibration was then confirmed using a 4 mm calibration ball submerged in the desired, organic continuous phase. This confirmation negates any error caused from refractive index.

The aqueous, dispersed phase was introduced to the continuous phase as a pendant drop. Droplets were produced using a screw thread Hamilton gas tight syringe and gauge 25 needle tip. Both continuous phase and dispersed phase were contained in a sealed, optical glass cuvette. All experiments were conducted at 20 ℃.

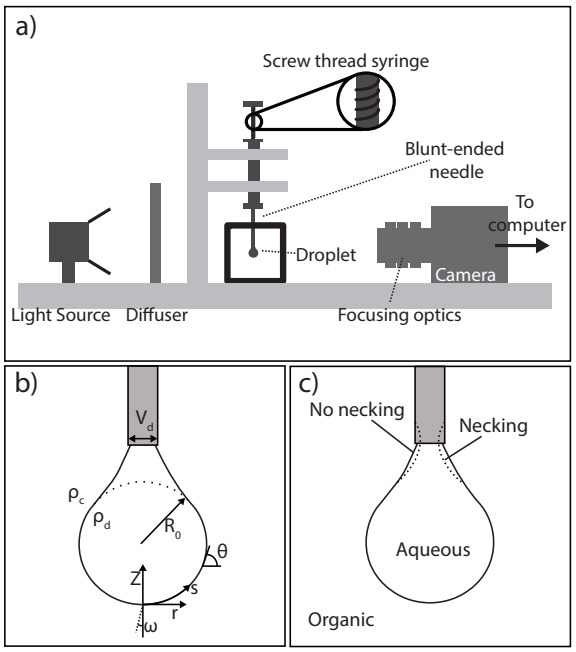

Figure 3.5: Interfacial tension experimental set-up. a: Set up of optical tensiometer for pendant drop interfacial tension measurements[42]. b: Measurements taken to determine IFT with the Young-Laplace model, further details are published by Berry et al[42] (repeated from Figure 2.5b for ease of reading). c: Ideal droplet condition for interfacial tension measurements.

A droplet at its largest volume without necking, see Figure 3.5c, was left to reach equilibrium. To ensure system equilibrium, the droplet interfacial tension was measured for 10 seconds, when three consecutive interfacial tension readings taken 30 seconds apart gave the same value, the system was assumed to have reached equilibrium.

The interfacial tension and droplet volume was measured for each system and repeated in triplicate. The volume of each droplet was compared to ensure a consistent maximum volume prior to necking. Droplet volume was controlled using the screw thread syringe.

Interfacial tension data presented within this investigation is the average of the triplicate results for each system.

A control experiment was first conducted using increasing concentration nitric acid dispersed phases (1 M, 3 M, 5 M HNO_3). The control dispersed phase measurements were taken within continuous phases of TBP ligand with varying dodecane dilutions. TBP dilutions used were 30 v%, 20 v%, 10 v% and 0 v% TBP.

The HMI experiment was conducted using increasing concentration of cerium (III) nitrate dispersed phases (1 M, 3 M, 5 M $Ce(NO_3)_3$). Cerium (III) nitrate solutions were prepared by matching the nitrate concentration to that of the control systems; from this nitrate concentration the mass of cerium could be calculated. Using the mass of cerium and the desired molarity the volume of water required could be calculated. The continuous phases used for the HMI experiments were the same as those used in the control experiment.

3.2.2 Results and discussion

The results from the control experiment (HMI free) are shown in Table 3.1; they show a large initial drop in IFT with addition of TBP from 0 v% to 10 v%; this drop plateaus upon further addition of TBP. These results suggest that the property control provided by dodecane dilution does not affect the process IFT within the industrially used region (20 v% - 30 v%)

Bajoria *et al.*[72] found the properties of increasing HNO_3 concentration varies after contact with increasing concentrations of TBP. For 3 M and 4 M HNO_3, a minimal increase in both viscosity and density was observed when increasing TBP. As the increase is minimal, they conclude that interfacial tension variations observed are due to adsorption of TBP at the interface, as opposed to changes in the physical properties of the HNO_3. The observations by Bajoria *et al.* support the data provided and confirm that the control experiment can be taken as a baseline for interfacial tension variations for the HMI free system.

The results from the HMI experiment, shown in Table 3.2, also show a large decrease in

Table 3.1: IFT variations with acid molarity within continuous organic phase.

Interfacial Tension mN/m		**Dispersed Phase**			
		Water	**1 M HNO3**	**3 M HNO3**	**5 M HNO3**
Continuous Phase	**Dodecane**	27.23	25.55	23.93	25.71
	10 v% TBP	12.52	7.02	11.60	11.33
	20 v% TBP	10.38	9.34	10.69	12.45
	30 v% TBP	9.43	8.89	9.82	11.77

interfacial tension followed by a plateau when TBP concentration is increased. This trend appearing in both systems confirms that interfacial tension within the PUREX process will not be affected by varying the dilution of TBP.

Table 3.2: IFT variations with [HMI] within continuous organic phase

Interfacial Tension mN/m		**Dispersed Phase**			
		Water	**1 M $Ce(NO_3)_3$**	**3 M $Ce(NO_3)_3$**	**5 M $Ce(NO_3)_3$**
Continuous Phase	**Dodecane**	27.23	35.37	40.99	Unavailable
	10 v% TBP	12.52	17.12	24.65	40.46
	20 v% TBP	10.38	14.72	26.62	43.64
	30 v% TBP	9.43	14.39	28.44	46.18

A notable difference to the control experiment observed within the HMI experiment is the increase in interfacial tension with increase of $[Ce^{3+}]$. As the loaded Ce^{3+} system does not experience the $[H^+]$ change present in the control, it was suggested that $[H^+]$ could inhibit interfacial tension increases. Previous studies have found that the ability of the P=O group on the TBP molecule to absorb onto an aqueous droplet is reduced with the addition of $[H^+]$[73]; therefore, it was expected that the interfacial tension observed for TBP/n-dodecane in the presence of HNO_3 would increase with acid strength. This behaviour was observed for the control system with an average increase of 30 % from 1 M HNO_3 to 5 M HNO_3 for 10 v% TBP and higher systems. Across the same range of continuous and dispersed phases the Ce_{3+} loaded system experienced an interfacial tension increase of 184%.

To investigate this further, the $[H^+]$ of the Ce^{3+} loaded systems was increased with small additions of concentrate HNO_3; the interfacial tesion variations with increasing $[H^+]$ are shown in Figure 3.6. With increased $[H^+]$, interfacial tension increases of 33 % and 109 % were observed for the 3 M Ce^{3+} systems in 30 v% TBP and n-dodecane when compared to 1 M, respectively; 80 % and 72 % of this change occurred once the system pH dropped below 1.5. The reduction of pH for the 1 M systems show no change in interfaical tension.

The increase in interfacial tension below $[H+] = 10^{-1.5}M$ is supported by previous studies[73], however, the overall increase in interfacial tension with $[H^+]$ is relatively small

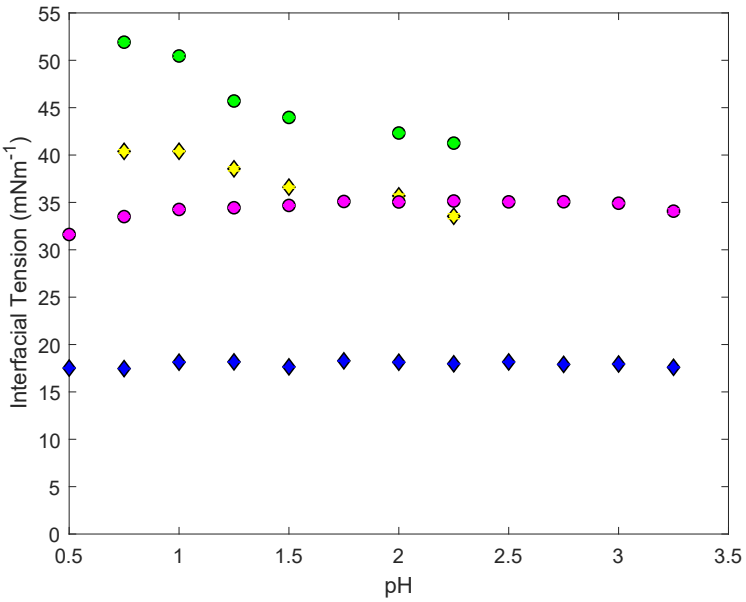

Figure 3.6: Interfacial tension variations with pH for different cerium nitrate systems. Where 1 M and 3 M $Ce(NO_3)_3$ in Dodecane are shown as pink and green respectively. 1 M and 3 M $Ce(NO_3)_3$ in 30 v% TBP are shown as blue and yellow, respectively.

when compared to the increase observed in Table 3.2. Therefore, the change in HMI loading is the primary reason for the change in interfacial tension for lower pH systems, such as those tested in Table 3.2 which were measured at 2.25 and 3.16 for 3 M and 1 M cerium nitrate, respectively.

The relationship established is an increase [HMI] within the aqueous phase will cause a large increase in interfacial tension. This increase is not affected by $[H^+]$.

3.3 Coalescence Rate

With an increase in [HMI] causing an increase in interfacial tension yet minimal influence on contact angle, further tests were conducted to find the practical implications of this relationship on a coalescing system.

Coalescence rate is a measure of the speed at which two droplets combine to become a single droplet upon a collision event. Coalescence is the primary mechanism for separation within a separation device. Here we measure the rate of coalescence while varying the pH

and [HMI]. Results values from the above interfacial tension experiments are used within the following analysis.

3.3.1 Methodology

Using a high-speed camera (Photron fastcam SA5, with x12 zoom lens) images of coalescing sessile droplets (stationary droplets on a surface) were taken at 6000 fps.

An optically clear, glass cuvette with a stainless-steel base was filled with the organic, continuous phase. Droplets of the dispersed phase were then positioned parallel to each other on the stainless base, diagram shown in Figure 2.11. The first droplet was placed on the base of the cuvette and allowed to relax; a single axis stage was then used to orientate a needle into a position where the relaxation of the second droplet would cause a coalescence event. Each droplet was formed using a screw thread Hamilton gas tight syringe and gauge 25 needle tip. The screw thread was used to control droplet volume.

The radius of the coalescing front, R_m, was measured using image processing software, ImageJ, an example of this is shown in Figure 3.7. The known size needle tip was used as the calibration reference.

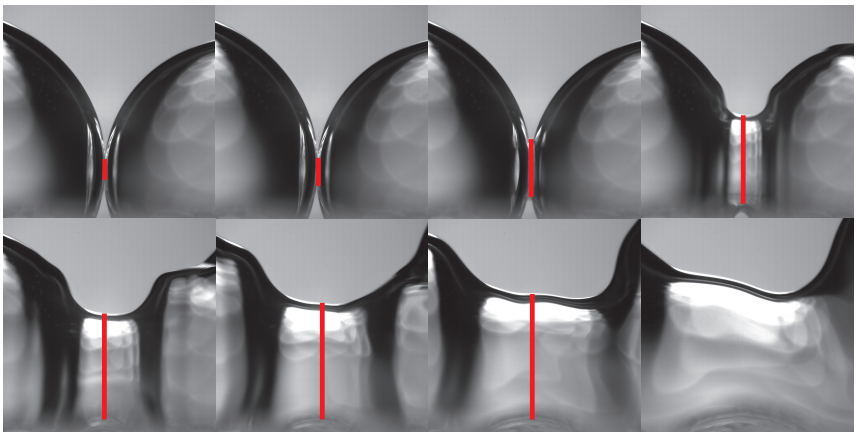

Figure 3.7: Growth of time line, R_m shown in red, over time. The difference between each frame is 1.67×10^4 seconds

The dispersed and continuous phases used were the same as those used within the interfacial tension experiments.

3.3.2 Results and discussion

Rate of coalescence for a droplet is governed by the relationship between the fluid viscosity, η, and interfacial tension γ. It was found by Egger *et al.*[74], that coalescence would occur by either viscous coalescence or inertial coalescence; equations for each situation were developed. Aarts *et al.*[70] found, based on a Reynolds number of the dispersed phase $Re \sim \frac{\rho\gamma R_0}{\eta^2}$, where ρ is the fluid density and R_0 is the undistorted droplet radius, the transition from viscous to inertial coalescence occurs at a Reynolds crossover position of $Re_c = 1.5 \pm 0.5$. The Re_c values for the baseline and loaded HMI systems were calculated using the viscosity terms, 1.19 cP and 1.42 cP, respectively[72,75]. The corresponding Re_c values were calculated as 6.25 and 3.82, confirming both systems are well within the inertial coalescence regime and, therefore the inertial model can be can be assumed true[74,76].

The Eggers *et al.* inertial model concludes with 3.1:

$$R_m \propto \frac{(\gamma R_0)}{\rho^{\frac{1}{4}}}\sqrt{t} \tag{3.1}$$

Equation 3.1 shows that the rate of growth of the tie line R_m, shown in 2.11 is proportion to $\sqrt{t}$, where t is time with a proportionality constant of k. Comparing the predicted R_m from Eggers *et al.* with the raw data collected from the high-speed camera recordings, there was strong agreement. We conclude that all data lies within the inertial coalescence region and that viscosity changes do not affect the coalescence rate of the tested systems; the comparison between raw data and the fitted model is provided in 3.8.

Normalising the data using the undistorted droplet radius, R_0, and inertial time (t_i), shown in Figure 2.11, the data collapses onto a linear relationship were the gradient term, k, can be used to compare the coalescence rate[77].

$$t_i = \sqrt{\frac{\rho R_0^3}{\gamma}} \tag{3.2}$$

It can be seen in Figure 3.9, that there is a clear distinction between the control system (HNO_3) and the loaded HMI system, signifying that loaded HMI droplets coalesce

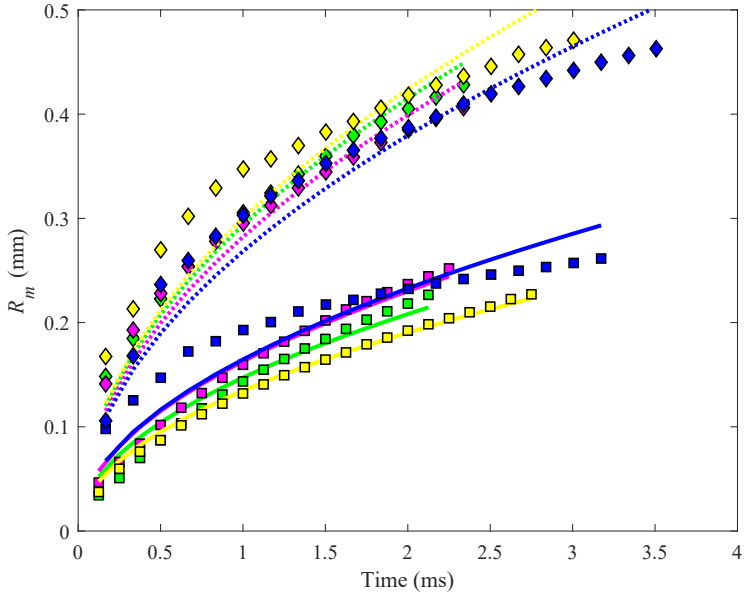

Figure 3.8: Time evolution of the radius R_m for the control and HMI system. Raw data is shown as symbols and the fitted data following the model, $R_m \sim \sqrt{t}$, shown as lines; dotted lines denote the HMI system and solid lines the control system. (◊: Cerium nitrate; □: Nitric Acid. 1 M in Dodecane: Pink; 3 M in Dodecane: Green; 1 M in 30 v% TBP: Blue, 3 M in 30 v% TBP: Yellow). The effect of the organic phase is not shown as the purpose of the figure is solely to compare the strength of the comparison between raw data and the fitted model.

faster. Average coalescence rates for systems with higher Ce_{3+} are 80.8 % faster than those observed for the corresponding control system, based on k values provided in Table 3.3.

Table 3.3: k values for direct comparison of rate of coalescence for the dispersed and continuous systems tested.

	1 M HNO_3	**1 M $Ce(NO_3)_3$**	**3 M HNO_3**	**1 M $Ce(NO_3)_3$**
Dodecane	0.36	0.79	0.42	0.73
30 v% TBP	0.51	0.88	0.43	0.82

For the [HMI] tested, an average decrease of 7 % was observed in the coalescence rate when the concentration is increased from 1 M $Ce(NO_3)_3$ to 3 M $Ce(NO_3)_3$. This decrease was expected as over the same range the interfacial tension is increased.

The k values show that coalescence rate in systems with TBP will coalescence faster than those without. On average the introduction of TBP increased coalescence rate by 12 %, this is supported by the drop in interfacial tension and droplet volume observed in

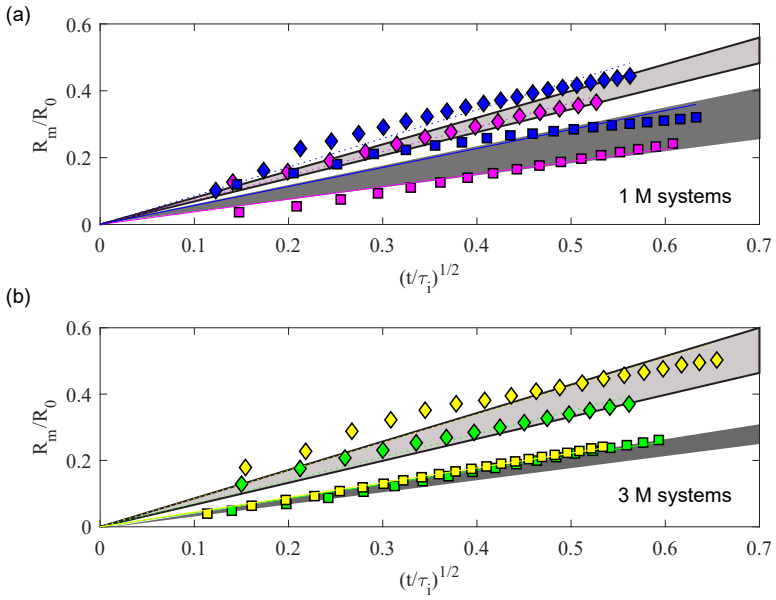

Figure 3.9: Scaled time evolution of the coalescing radius R_m for different aqueous and organic systems. Where (a) focuses on 1 M systems and (b) 3 M system. ($\Diamond$: Cerium nitrate; $\square$: Nitric Acid. 1 M in Dodecane: Pink; 3 M in Dodecane: Green; 1 M in 30 v% TBP: Blue, 3 M in 30 v% TBP: Yellow) Shaded regions are also used to guide the eye, light grey: cerium nitrate and dark grey: nitric acid.

.

the presence of TBP.

3.4 Conclusions

In all cases an increase in [HMI] results in an increase in interfacial tension and a higher coalescence rate. The introduction of TBP increased coalescence rate by 12 %, this is supported by the drop in interfacial tension and droplet volume observed in the presence of TBP. This interfacial tension change was found to be controlled by the [HMI] for systems with a pH greater than 1.5. Below a pH of 1.5 the interfacial tension is likely governed by the relationship at the droplet interface between the ligand, TBP, and $[H^+]$. This relationship between interfacial tension and coalescence rate was expected due to the well documented theory of cohesive forces of molecules at the droplet interface[41].

In practice this conclusion means that in an industrial flowsheet the efficiencies of the

separation stages will vary with a bank as the HMI varies and so, the system [HMI] and diluent concentrations must be taken into consideration to improve separation efficiency and reduce over-engineering.

Part II

Coalescence in Confined, Flow-driven Systems

CHAPTER 4

Flow-Driven Coalescence Theory

The joining of droplets in a flowing system is known as flow-driven coalescence, as opposed to static coalescence investigatedin Chapter 3[33]. As discussed in section 3.3, coalescence is the joining of two droplets after a collision event, and can be effected by changes in [HMI] and pH in a static system. Unlike static coalescence, when considering colliding droplets in a flowing system, coalescence or droplet break-up can occur. In steady state flowing conditions, a balance between the coalescence and break-up is achieved, producing a specific droplet size population[78].

The extent to which static or flow-driven coalescence influences a rectangular channel is estimated through the calculation of the Peclet number[78,79].

$$Pe = Re.Pr = \frac{\rho_d v_d d_h}{\mu_d} \frac{\mu_c Cp_c}{\kappa_c} \tag{4.1}$$

where Re and Pr are the Reynolds and Prantdtl number, v_d is the droplet velocity, hydraulic diameter, $d_h = \frac{2ab}{a+b}$ where a and b are the width and height of the rectangular duct, Cp the specific heat capacity, and κ the thermal conductivity both for the continuous phase. In a system with a $Pe >> 1$ flow-driven coalescence will dominate[33].

In flow-driven coalescence conditions, coalescence is only guaranteed within a small area surrounding the droplet, shown in purple in Figure 4.1. This region is bound by the streamline path of a small droplet, A, with a droplet diameter of d_A, progressing towards the larger droplet, E (diameter d_E). The coalescence of A into E is represented by droplet B. Whereas, outside of the region $d_E + d_A$, the coalescence of small diameter droplets cannot occur, shown by droplet C. For droplets with diameters spanning over the $d_E + d_A$ range, shown as droplet D, droplet deformation will occur upon approach due to momentum along streamlines. Coalescence or rebound of droplet D to E will be dependant on the kinetic force of the collision. Droplets flowing completely outside of the $d_E + d_A$ region will not coalesce.

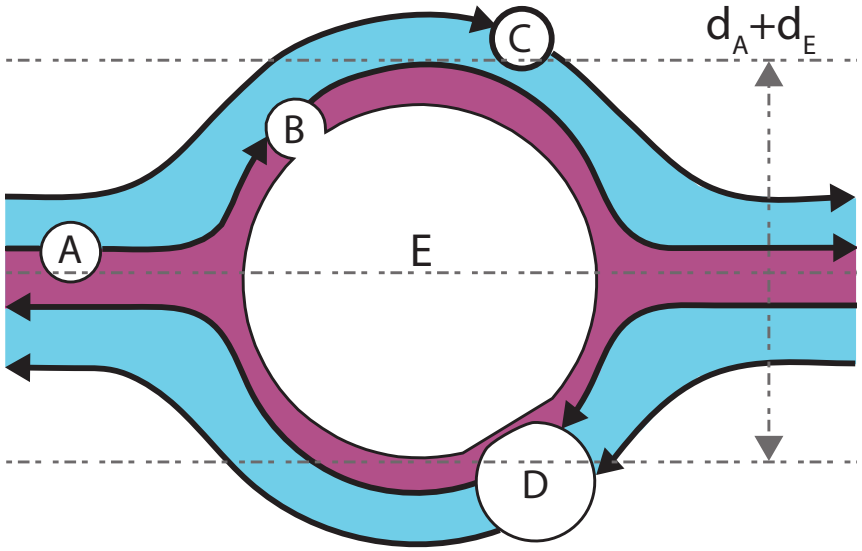

Figure 4.1: Flow-driven Coalescence

Lyu *et al.*[78] state that the computational modelling of flow-driven coalescence is simple in comparison to static coalescence. This is due to a reduction in the driving forces experienced in static coalescence, such as: Brownian motion and sedimentation. They continue to state that in many instances it is more suitable to study flow-driven systems as opposed to the conventional static mechanisms used. However, in contrast to the extensive literature published for computational flow-driven coalescence with solid particles and experimental static coalescence of L-L systems, there is little reported on flow-driven coalescence in experimental L-L systems[33,78,80–83]. Lyu *et al.* suggests a reason for this imbalance in research is due to the technical difficulty in experimentally measuring droplet size distributions under flow conditions. Chen *et al.*[82] corroborate the statement made by Lyu *et al.*, stating that as flow-driven coalescence inevitably involves multiple droplet interactions, it is more complex to study experimentally.

Under flow-driven coalescence conditions, the coalescence efficiency is proportional to the collision frequency, $\dot{c}$, for equal-sized spherical droplets in viscous shear flow[33].

$$\dot{c} = \frac{2}{3}\dot{\Gamma} d^3 n^2 \tag{4.2}$$

where $\dot{\Gamma}$ is the shear rate (s^{-1}), d is the droplet diameter and n is the number of droplets per unit volume. It can be seen that the collision rate is heavily influenced by the droplet diameter.

In a microfluidic device the shear rate experienced by a dispersed droplet from the continuous phase is much greater than that experienced in a macrofluid[84]. Therefore, it is reasonable to assume a higher frequency of collisions within a microfluidic device as there is a greater opportunity of coalescence occurring. However, a high shear rate can also increase the probability of break-up of larger droplets, reducing the d^3 term in Equation 4.2. A measure of whether a droplet will coalesce or break within high shear flow is the Capillary number (Ca).

$$Ca = \frac{\eta_c v}{\gamma} = \left(\frac{\eta_c \dot{\Gamma} r}{\gamma}\right) \tag{4.3}$$

where η_c is the continuous phase viscosity and r the droplet radius.

A critical value of the Capillary number exists at the point at which coalescence can no longer occur[82,85,86]. Calculation of the critical Capillary number (Ca_{crit}) is dependant on a critical droplet diameter as a function of shear rate, and other physical parameters of the dispersion[87].

$$Ca_{crit} = -0.506 - 0.0994log(p) + 0.124log^2(p) - \frac{0.115}{log(p) - log(p_{crit})} \tag{4.4}$$

Ca_{crit}, as shown in Equation 4.4, is reliant on the viscosity ratio of the dispersed and continuous phase, $p = \frac{\eta_d}{\eta_c}$. Based on experimental data obtained by Grace[88], p_{crit} is taken as 4.08. However, it has since been proven that Ca_{crit} is influenced by many factors including shear rate, droplet size, velocity gradient direction, viscosity ratio, flow type, and the molecular weight of the continuous fluid and therefore is best determined computationally[81,82,85,89].

When the viscosity ratio, p, is between 0.1 and 1, Equation 4.4 gives the minimum critical capillary number, Ca_{crit}, above which droplet break-up is prominent[86]. Therefore, a separation device requiring efficient coalescence must have a Ca less than Ca_{crit}[33]. Ca_{crit}

has been reported between 0.3 and 0.5[90–92]. Below Ca_{crit}, shear rate has a high influence on $\dot{c}$ in Equation 4.2[33]. Shear rates within a P-TS have been reported in the region of $10^4\,s^{-1}$[33]. This is much higher than those experienced in macrofludic devices. According to Equation 4.2, a collision frequency is directly proportional to shear rate, therefore it could be assumed that a high shear rate would result in greater coalescence. However, increasing shear rate and therefore, droplet break-up reduces the d^3 term; where d^3 is a more dominant factor in the calculation of collision rate. Increased shear rates and droplet break up would also result in an increase in the number of droplets per unit volume, n in Equation 4.2. As the n term is to the power two, a combination of increased shear rate and number of droplets could influence collision frequency to a greater extent than the reduction in droplet diameter.

4.1 Confinement in Microchannels

In addition to Ca_{crit}, the angle at which two droplets collide has also been found to effect coalescence, provided the ratio of the droplet diameters is outside of the range, 0.7 to 1.[93] To control this coalescence angle and promote coalescence within a flowing system, the space in which the droplets meet can be dramatically reduced, this technique is known as confinement[82]. Confinement is represented by the measurement, $2r/H$, where r is the droplet radius and H the plate spacing. The beneficial effects of confinement ratio are experienced when $2r/H > 0.1 - 0.2$[33,94].

Chen *et al.*[82] found that when increasing the shear rate and maintaining droplet size, $2r < 200\ \mu m$ for bulk flow conditions, the critical capillary number for coalescence decreases with increasing droplet size. Chen *et al.*[82] continuous to gradually increase confinement. Initially at low degrees of confinement, they find that the angle of coalescence is decreased with respect to that of the bulk flow but Ca_{crit} remains unchanged. With further confinement increases, both the coalescence angle and Ca_{crit} are influenced by the presence of the device walls, resulting in a substantial increase in Ca_{crit} and changes to the flow field surrounding droplets within complete confinement $2r/H > 0.2$. In practical

terms this statement means, by introducing confined conditions, the angle of coalescence is reduced and droplets are forced into the purple and blue regions shown in Figure 4.1.

Blawzdziewicz *et al.*[94] provide a reason for this increased coalescence efficiency in confinement. They found that strong confinement causes a pull on central droplets towards the walls, shown in Figure 4.2. These central droplets are likely to flow directly through the microchannel under non-confined conditions. Due to frictional forces, this movement of droplet flow towards the walls under confinement would cause droplet velocity to decrease, increasing the droplet interaction time between the coalescencing pair. Chen *et al.*[82,95] also state that, confinement causes a change in the flow field around the droplet pair, increasing the total interaction time between them and reducing the coalescence angle. Therefore, under confined conditions droplets are forced together at the walls by confinement, slowed by wall effects and spend longer interacting at a reduced coalescence angle. It is thought that the combination of these three factors causes the increased efficiency observed within the P-TS investigations described in Section 1.4.

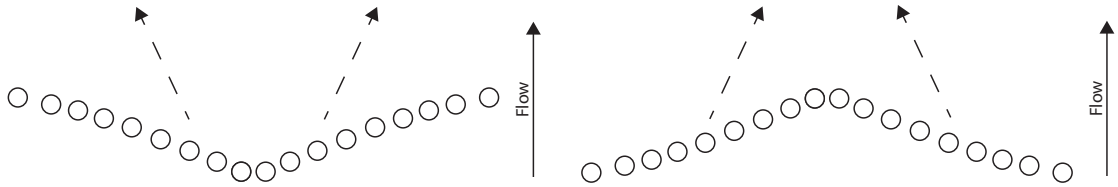

(a) Confined conditions (b) Unconfined conditions

Figure 4.2: Dynamics of flow under confined and unconfined conditions. The flow direction is indicated and the driving force for both conditions is equal, acting parallel to the walls[82,94]

Confinement within a microchannel has also been reported to cause the formation of flow structures in immiscible liquid polymer blends. Migler[96] reports an elongation of droplets into strings with increasing shear rate. The elongation was reported for systems with a viscosity ratio roughly equal to 1 and dispersed droplet diameters comparable to the channel width of two parallel plates. Previously, structures like this had only been observed in biphasic systems with solid particles, such as in sedimentation[97–99].

The formation of string like structures occurs in four stage process, as shown in Figure 4.3. The initial stage is coalescence of smaller droplets resulting in an increase in overall

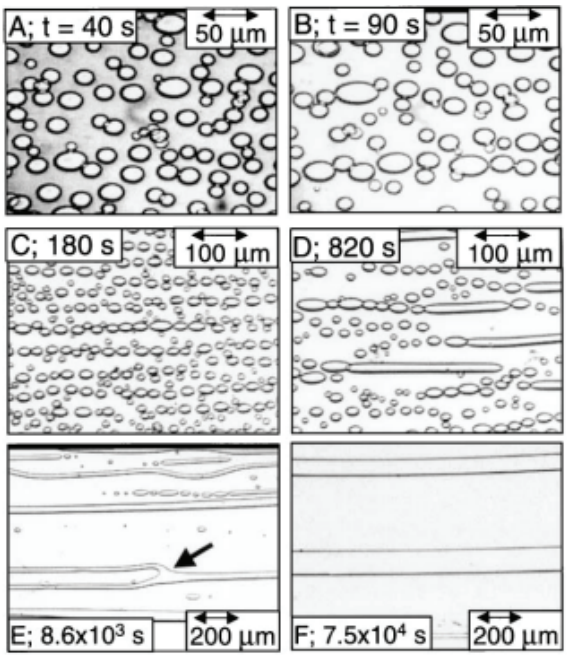

Figure 4.3: Formation of flow structures in confinement with time where, A and B show the elongation of droplets, C the formation into necklace like structures, D the coalescence into ribbons and E and F the coalescence and growth of ribbon structures[96].

average droplet volume. Next the larger droplets self-organise into necklace like structures. The aligned droplets coalesce to form strings and finally, the strings coalesce to form thicker strings, to be called ribbons[96]. Migler[96] speculates that the formation of the structures is a result of the distortion of the velocity field around the droplets when droplet diameter is comparable to channel width. This distortion is thought to cause an attractive interaction between the flowing droplets. Migler[96] also reports stable droplets with a $Ca >> 1$; droplets in these conditions would break up in non-confined systems. This behaviour can be explained by an increased stability due to wall confinement as discussed above. The removal of the wall would result in string break-up due to the Rayleigh-Tomotika mechanism. The Rayleigh-Tomotika mechanism, also referred to as Rayleigh-plateau instabilities[100], states that long cylindrical liquid strings will become linearly unstable with disturbances with a wavelength longer than the circumference of the string in non-confined systems, $2\pi R_s$, where R_s is the radius of the string[101–104]. Capillary break-up in this way is a well understood occurrence in fluid mechanics[103]. As

such, a potential suppression of this under confinement has lead to large interest in the field droplet production in microfluidic devices[105–107]. However, little is reported on its effect in micro-separators.

4.1.1 Hele-Shaw cell

In literature the space between two parallel plates has also been termed a Hele-Shaw cell[108–110]. There are many similarities between research described as confinement in parallel plate channels and those described as Hele-Shaw cells. Both theories provide descriptions of elongating droplets which break up to form characteristic flow patterns due to Rayleigh instabilities and/or varying shear stresses. However, Hashimoto *et al.* state that the classic Hele-Shaw equations neglect the droplet velocity and its dependance on capillary number[110].

However, independent of the specific Hele-Shaw equations, much of the literature surrounding droplet flow in Hele-Shaw cells discusses in detail shear-induced migration and Saffman lift forces in terms of droplet travel in a thin, parallel channel. Saffman lift force, also called wall migration, is the force felt by a droplet in the presence of a wall[111,112]. This force opposes the pull of gravity on a flowing droplet causing it to lift away from the surface as opposed to settling on the wall. Shear-induced migration is the migration of a flowing, bounded droplet towards the centre of a channel[112,113]. Leal *et al.*[114] have produced extensive investigations into this area, providing detailed computational analysis of a droplets dependency on both the velocity induced by buoyant forces and that from droplet migration in microchannels. The most important details from these investigations to this work is that both Saffman lift force and shear-induced migration are influenced by capillary number, shear-rate, plate spacing and droplet diameter[111,112].

4.2 Practical Implications of Flow-Driven Coalescence Theory on the P-TS

It has been reported that the combination of shear-induced migration and Saffman lift cause a significant increase in coalescence of droplets. Figure 4.4 shows the repulsion of oil from the hydrophilic wall focuses a current on the hydrophobic wall. Without the confinement and repulsion kinetics induced by the P-TS geometery, the flow profile would be symmetrical around the z axis. The effect of droplet migration towards the centre of the channel causes an increase in droplet concentration in this area. In turn, this increases the number of collisions that can occur and therefore results in greater successful coalescence events.

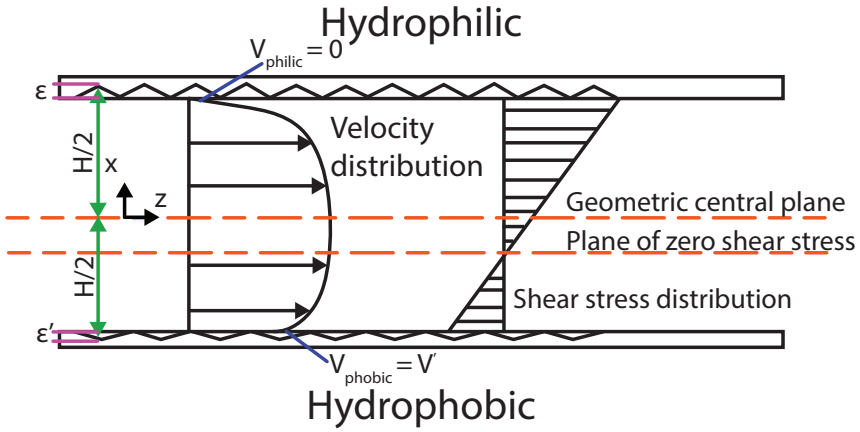

Figure 4.4: Schematic of confined flow between PTFE-SS microchannel under slip-wall boundary condition. ε is the roughness of the SS plate, which is $\approx 2\ \mu m$, and ε' is the roughness of the PTFE plate, which is $\approx 0.2\ \mu m$; H is the height of microchannel. V_{philic} is the velocity of the continuous phase at the SS surface, and V_{phobic} is the velocity of the continuous phase at the PTFE surface. V_{phobic} was non-zero at slip condition[33].

Chen *et al.*[33], discuss an imbalance of the classically asymmetry velocity distribution profiles due to the hydrophobic and hydrophilic materials used to construct the P-TS. It is suggested that this is why the researchers have found a dramatic reduction in separation efficiency when changing the materials of construction to PTFE-PTFE and glass-glass[31–33].

Initially it was assumed that oil droplets collide with the hydrophilic wall and settle. However, it is now believed they bounce away from the hydrophilic wall, increasing the

density of oil droplets between the central axis and the hydrophobic wall. The opposite of this would occur for water droplets, increasing the density of water droplets between the central axis and the hydrophilic wall. Chen *et al.* uses wall and shear migration to describe this movement[33]; however, also considers the work completed by Blawzdziewicz *et al.*. Discussed above in Figure 4.2, Blawzdziewicz reported a relaxation of the high-density region at the center of the channel under strong confinement conditions causing a general movement of droplets towards the walls[94]. It would take an accompanying, comprehensive computational simulations to completely understand the flow behaviour within the P-TS. However, through review of the literature, it is proposed that the high efficiency separation achieved in the P-TS are the result of shear-induced migration of droplets in confinement. This assumption is strengthened experimentally within the proceeding experimental results chapters.

CHAPTER 5

Development of Ancillary Methodologies

The aim of this chapter is to optimise experimental procedures in order to accurately measure the extent at which the design optimisation undertaken in Chapters 6 and 7 effect the separation efficiency of a P-TS of fixed length.

After reviewing previous studies conducted with the P-TS, in Section 1.4, it was considered that conclusive, experimental evidence as to why a decrease in separation efficiency is observed with increased plate spacing was not available. To address this, a clear Poly(methyl methacrylate) (PMMA) and stainless steel (SS) P-TS was designed. The clear PMMA plate was used to allow for visual tracking of fluid flow patterns and droplets within the P-TS. It was predicted that as the separation efficiency decreased, there would be a visible difference in the flow pattern and droplet size distributions (DSD) across the plate length.

5.1 Design and Manufacture of P-TS

A modular design was chosen for the P-TS to allow for the inter-changing of plates and gaskets. Varying thickness gaskets will be used to change the plate spacing of the P-TS. From Figure 5.1a, it can be seen that a four plate design was chosen consisting of the PMMA upper plate, SS gasket, SS lower plate and a supporting backplate. The modular design was held together with 14 bolts allowing for the even distribution of pressure across the entire plate. Previous work has reported that the inclusion of an o-ring between the gasket and upper or lower plate gives a false reading of the plate spacing, therefore, in this work an o-ring was not included within this area. A thin o-ring was included between the SS lower and supporting backplate to ensure no aqueous outlet liquid was lost, the location of this o-ring can be seen in Figure 5.1a. Although, it was later observed that the surface between these plates was dry when changing plates between experiments and concluded that this o-ring was not required. To further ensure equal pressure was applied across plate

area a torque wrench was used to precisely apply an equal torque to all bolts. Notches were included on the SS lower and supporting backing plates to aid in the disassembly of the gasket from the rest of the P-TS. The final dimensions and locations of the inlet and outlets are shown in Figure 5.1b.

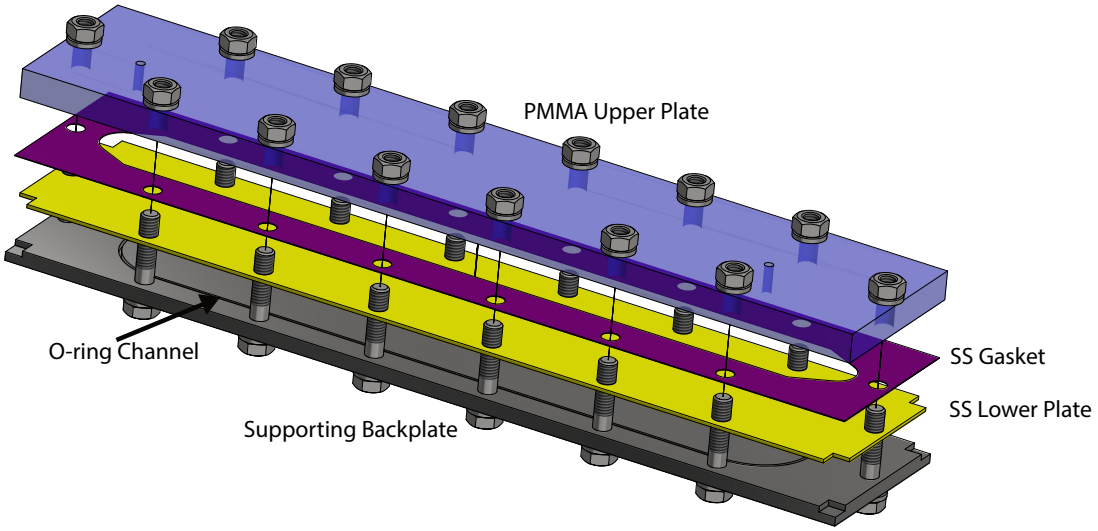

(a) Final exploded design where clear blue indicates the PMMA top plate, purple the SS gasket, yellow the SS lower plate and grey the SS support plate.

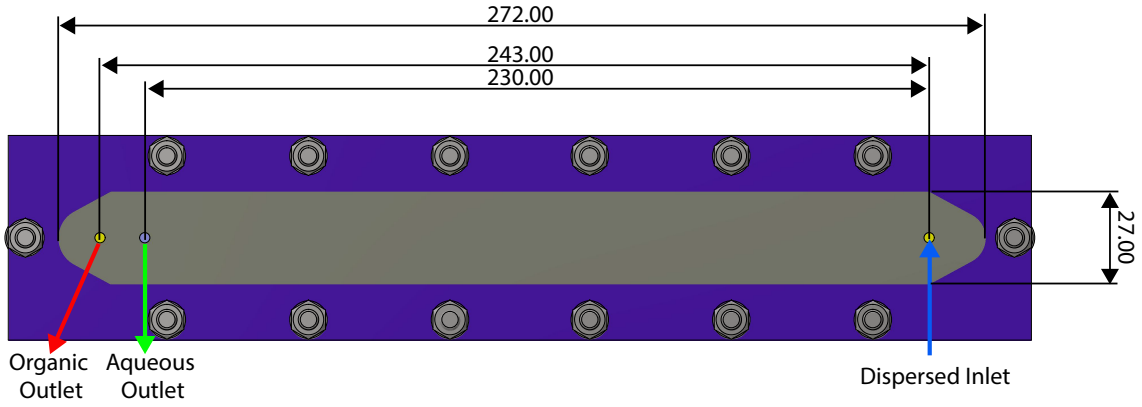

(b) Final Dimensions of P-TS, where the black arrow indicates the dispersion inlet, red arrow the organic outlet, both of which are located on the PMMA plate. The green arrow indicates the location of the aqueous outlet on the SS plate.

Figure 5.1: Final design views and dimensions of P-TS

5.2 Methodology Development

This section of the thesis describes key stages of the methodology required to determine separation efficiency. The key areas for development are dispersion longevity, and accurate visualisation of both macroscopic and microscopic flow structures; including DSD prior, during and post separation. It is data reliability within these areas that will ensure the data presented in this thesis are a true representation of P-TS performance.

5.2.1 Dispersion analysis

A study was undertaken to investigate the bulk dispersion characteristics of the systems investigated in Chapter 3. The bulk dispersion characteristics, primarily the dispersion separation rate, will have to be known before use within the P-TS. The aim of this study is to fully understand how the interfacial tension, pH and [HMI] effect the bulk settling under gravity separation. The result of this study will be the determination of optimum parameters for creating stable dispersions for use within the P-TS investigations.

The outcome of these experiments was unexpected as reported separation times within pulse columns and mixer settlers within THORP are much longer than what was observed within this study[115,116]. The differences between the systems tested within these experiments and those used within the THORP facility are the increased temperature from the heat of radiation, viscosity increases from radiation degradation of the organic phase, larger HMIs and greater [HMI]. The results in Chapter 3 and the discussion in Section 2.4, show that and increase in [HMI] and system temperatures speeds up separation, therefore, it is most likely an increase in viscosity caused by radiation degradation of the organic ligand TBP causing the reduction of dispersion stability observed within this study.

The dispersions resulting from this investigation must remain stable for prolonged periods. This will ensure that any separation that occurs during the P-TS investigations is solely due to the P-TS and no other factors. As discussed, effective solvent extraction requires dispersion stability over an adequate time period to allow for the desired mass transfer to occur. Many of the static droplet factors discussed in Chapter 2 can be taken

into consideration when trying to prolong dispersion stability such as, surfactant addition or changing process temperature/viscosity.

Destabilisation of a dispersion is the process of a dispersion returning to two distinct, immiscible phases. This can happen in four ways: Otswald ripening, aggregation, sedimentation and coalescence. From literature[17,69,117], it has been shown that coalescence, discussed in Section 2.6, is the primary form of destabilisation. However, the other secondary forms of destabilisation are briefly discussed below.

Ostwald ripening is the process of diffusion of dispersed phase molecules through the continuous phase[117]. This occurs due to a concentration difference of dispersed phase molecules between larger and smaller droplet volumes. The concentration of molecules at the interface of the droplet is inversely proportional to its radius of curvature; therefore, smaller droplets have a higher proportion of molecules at the surface[117]. When a large droplet comes into close proximity with a smaller droplet, this concentration gradient causes the molecules in the interface of the smaller drop to diffuse through the continuous phase and into the larger droplet. Over time it appears that the smaller droplet disappears, and the large droplet grows with no collision event occurring. This process occurs very slowly and is not usually the primary form of phase separation.

Aggregation, or flocculation, is the process of droplets touching but not coalescing[17]. This interaction causes larger structures of individual droplets, not larger droplets overall. The droplets are attracted to each other by Van der Waals forces but stopped from coalescing by repulsion forces of either electrostatic or steric repulsion[17]. Droplets are held closely together while maintaining a thin film of continuous phase between them. Flocculation is more likely to occur in colloidal or surfactant containing systems[17,117]. The larger volume of the flocs, a group of droplets joined during flocculation, results in increased sedimentation and coalescence rates.

Sedimention is the natural separation of droplets under gravity[17], and is heavily influenced by the other destabilisation methods. Separation by sedimentation follows Stokes law[17], Equation 1.2, and is governed by the density difference between the liquids. Over time the dispersion separates into two separated continuous phases. This time period is

determined by the density difference and the radius of the droplets within the dispersion. Dispersions with larger radii droplets can separate in a time period of seconds. Whereas, dispersions with smaller radii can form stable, creamed emulsions and can remain stable for several hours. This separation can be seen in Figure 5.2.

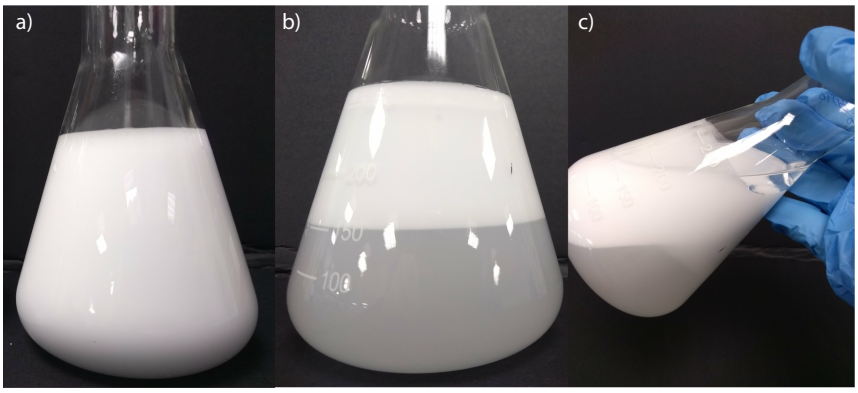

Figure 5.2: Settling behaviour of a 50:50 Aq:Org dispersion of water/kerosene produced via high shear mixing for 10 minutes where; a is the separation time at t = 0, b at t = 6 hours, and c at t = 6 hours (alternative view)

Initially, Figure 5.2a, the entire solution was dispersed creating a white, creamed dispersion. After 6 hours the heavier, water layer had separated, reducing the volume of the dispersed layer. From Figure 5.2c, it can be seen that a film of the creamed layer had adhered to the glass of the conical flask giving the illusion of a thicker layer than what was actually present. This adhesion is most probably due to contamination of the glassware and was taken into consideration within the experimental methodology.

5.2.1.1 Methodology

All reagents used were 99% purity or higher from Fisher Scientific (Loughborough). All water used is ultrapure, deionized water from a MilliQ by Millipore water purification system (Millipore, Watford, UK). Between each experiment all glassware was thoroughly decontaminated with Decon-90 and acetone and dried for an hour in a drying oven. Glassware was left to cool to room temperature before beginning the experiment. This thorough cleaning was required to avoid the adhesion observed within an initial test dispersion shown in Figure 5.2c.

A flask was fed with both organic and aqueous phases, then the dispersion was mixed with a high shear mixer for 10 minutes. After 10 minutes the dispersion was transferred into a measuring cylinder. The separation of the dispersion was recorded at 15 fps for an hour, or until the dispersion had fully separated. This methodology is shown in Figure 5.3. The upper and lower phase boundary of all captured frames were tracked using image processing software, AxioVision. A basic schematic of this process is shown in Figure 5.4. Dispersion results between Figure 5.5 and Figure 5.10 show smoothed, average triplicate data.

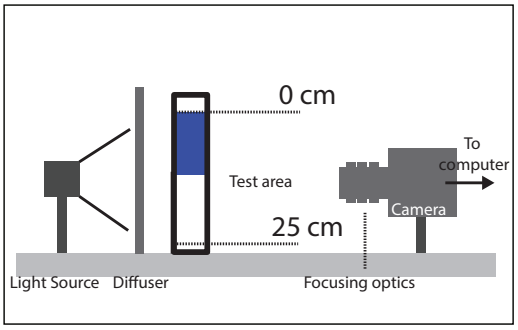

Figure 5.3: Dispersion recording experimental set up, the test area shows the area of the measuring cylinder visible to the camera.

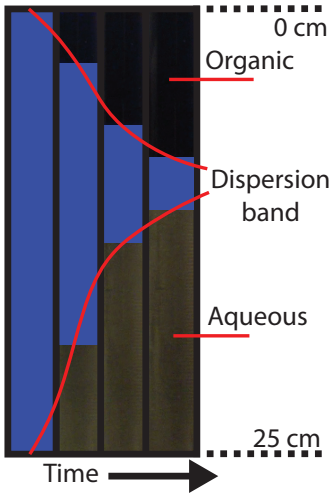

Figure 5.4: Schematic image demonstrating the basic procedure followed by Axiovision for dispersion band tracking

5.2.1.2 Results and discussion

While process parameters were being determined, a less toxic, inexpensive water/kerosene system was used. It was decided that this system would be used for preliminary tests as it displays comparable properties and is more cost effective and sustainable than TBP/Dodecane/acid mixtures. The parameters to be determined within these experiments were the ideal speed of agitation and aqueous to organic ratio (Aq:Org). The systems tested were 80:20, 70:30 and 50:50 Aq:Org, shown in Figures 5.5a to 5.5c. It was found that the highest agitation rate created the greatest stability dispersion for all cases. From Figure 5.5d, it is shown that the Aq:Org ratio does not effect the stability of the dispersion over an extended time period. Parameters of 70:30 Aq:Org and highest agitation rate (2000 RPM) were chosen. These parameters were chosen because they provide the desired dispersion longevity and will provide a reduction in organic waste produced.

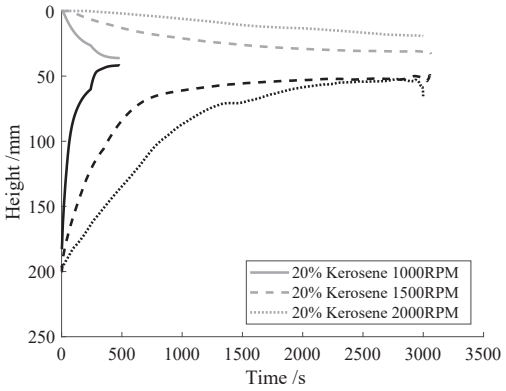

(a) 20 v% organic, variable agitation speeds.

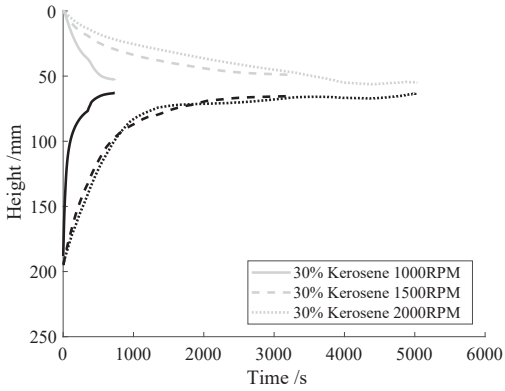

(b) 30 v% organic, variable agitation speeds.

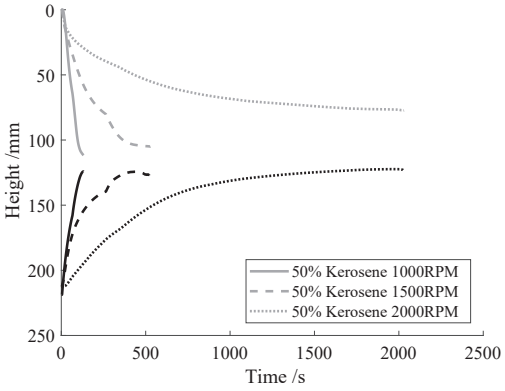

(c) 50 v% organic, variable agitation speeds.

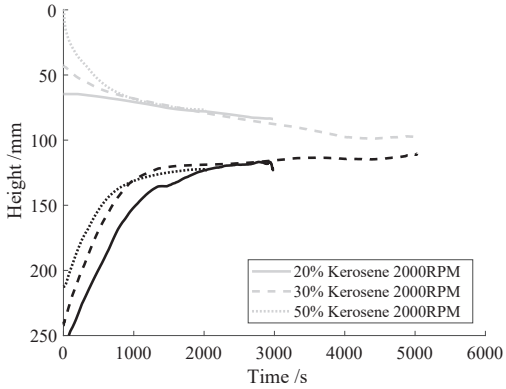

(d) 2000 RPM Agitator speed, variable kerosene content.

Figure 5.5: Determination of process parameters, Organic:Aqueous ratio and agitation speed (Aqueous - bold lines, Organic - grey lines).

An isolated droplet TBP/n-dodecane - nitric acid system was investigated within Chapter 3 as this system is traditionally used within the nuclear reprocessing industry. Further testing was required to investigate the bulk properties of system before use within the P-TS efficiency investigations in Chapter 6. In Figure 5.6 it is shown that, regardless of molarity or [HMI], the dispersion is not stable and separates within approximately 60 seconds as opposed to upwards of 30 minutes for the water/kerosene system.

Looking closer at the individual graphs within Figure 5.6, it can be seen that increasing aqueous phase molarity and decreasing [HMI] decreased the dispersion stability (shown in Figures 5.6a and 5.6b). This result is in correlation with the coalescence rate data provided in Chapter 3. However, the slight increase observed in dispersion stability could

lie within the error of the phase tracking software. Overall, the cerium containing systems had the greatest dispersion stability, with 3 M $Ce(NO_3)_3$ maintaining a dispersion for the longest, Figure 5.6d. This dispersion was only maintained for approximately 70 seconds.

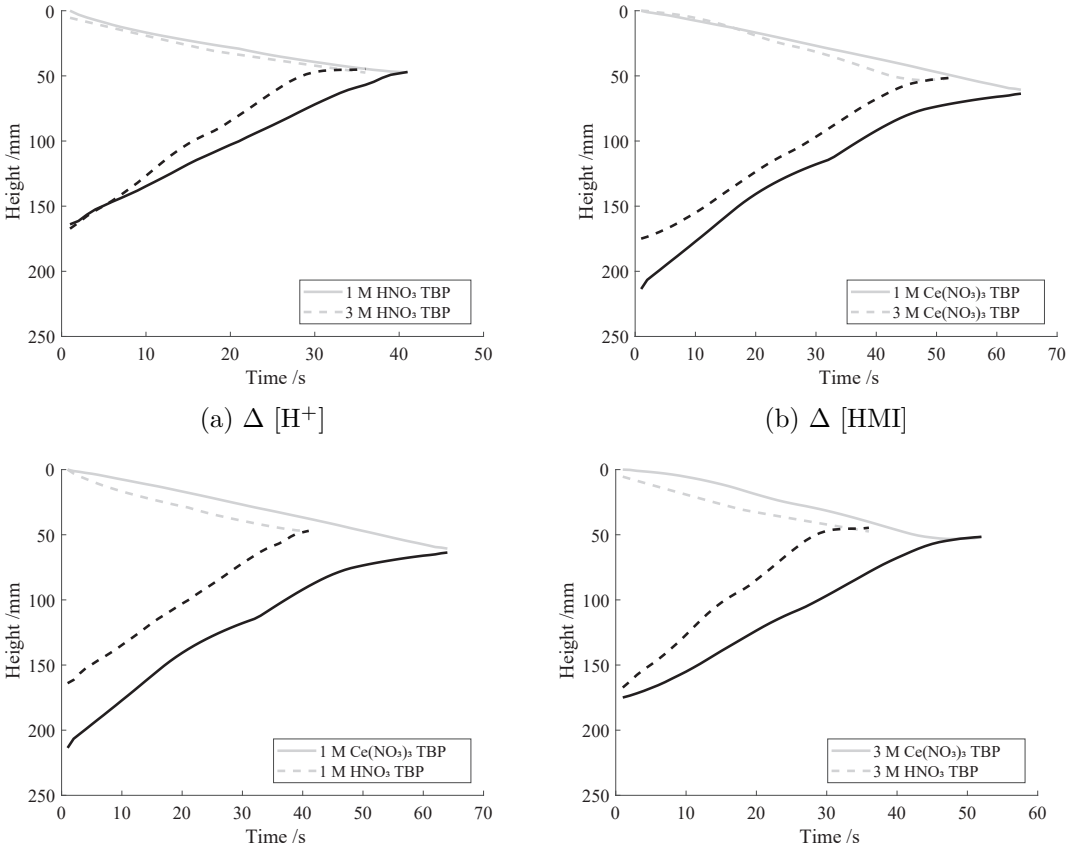

(a) Δ $[H^+]$ (b) Δ [HMI]

(c) Low $[H^+]$ (d) High $[H^+]$

Figure 5.6: Dispersion stability for varying [HMI] and $[H^+]$. The aqueous, lower dispersion band is shown in bold, and the organic, upper band as grey lines.

From literature it was observed that the addition of surfactant sodium dodecyl sulfate (SDS) can be used to prolong the stability of dispersions[32,33]. Surfactants, also known as surface active agents, are long chain molecules with a hydrophilic head and hydrophobic tail. They are added to solutions to stop the formation of aggregates or to stop molecules from adhering to surfaces within a separation device[41]. Surfactants freely diffuse through the liquid until caught at an interface. At the interface, the head is held in the aqueous phase and the tail reaches out into the organic as shown in Figure 5.7a.

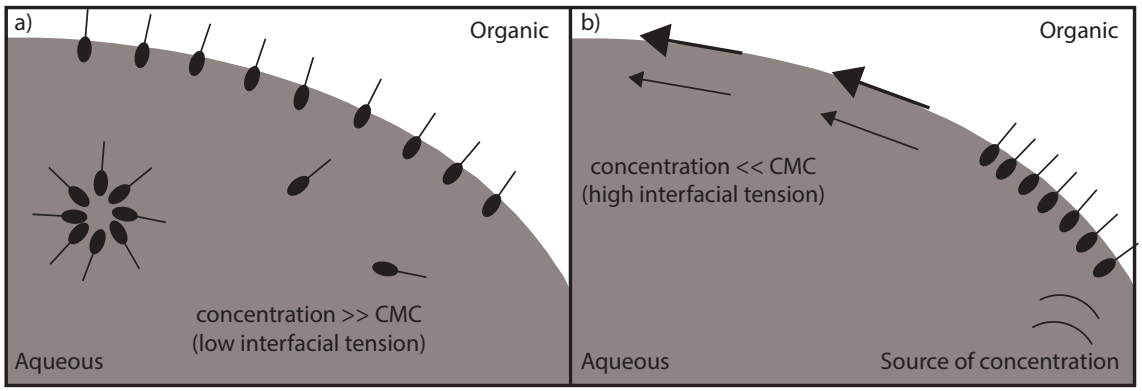

Figure 5.7: Schematic of surfactant use at a droplet interface[41].

The gathering of surfactant molecules on the interface lowers the interfacial tension, therefore lowering the chance of droplet coalescence. This effect is only observed above a critical point known as the critical micelle concentration[41], CMC. The CMC is reached when the interface is fully saturated with surfactant, after this the surfactant can be found within the bulk, represented as a cluster of surfactant molecules in Figure 5.7. Figure 5.8 shows how the CMC must be reached in order to achieve a constant interfacial tension reduction.

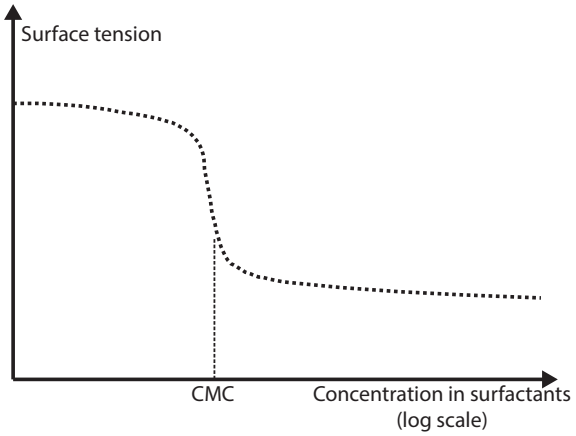

Figure 5.8: Effect of achieving the critical micelle concentration on the interfacial tension of a liquid[41]

As with temperature effects, surfactant effects can cause Marangoni convection within a droplet[41]. If surfactant concentration is less than the CMC, the interfacial tension can be determined experimentally using a methodology similar to that used in Section 3.2.1.

The interfacial tension will be higher when surfactant concentration is lower than the CMC as shown in Figure 5.7b.

To prolong the dispersion separation time of the nitric acid, cerium nitrate systems, 1 mL of concentration 1 g/L solution of SDS was added to each of the aqueous phases. This amount was sufficient to reach the CMC.

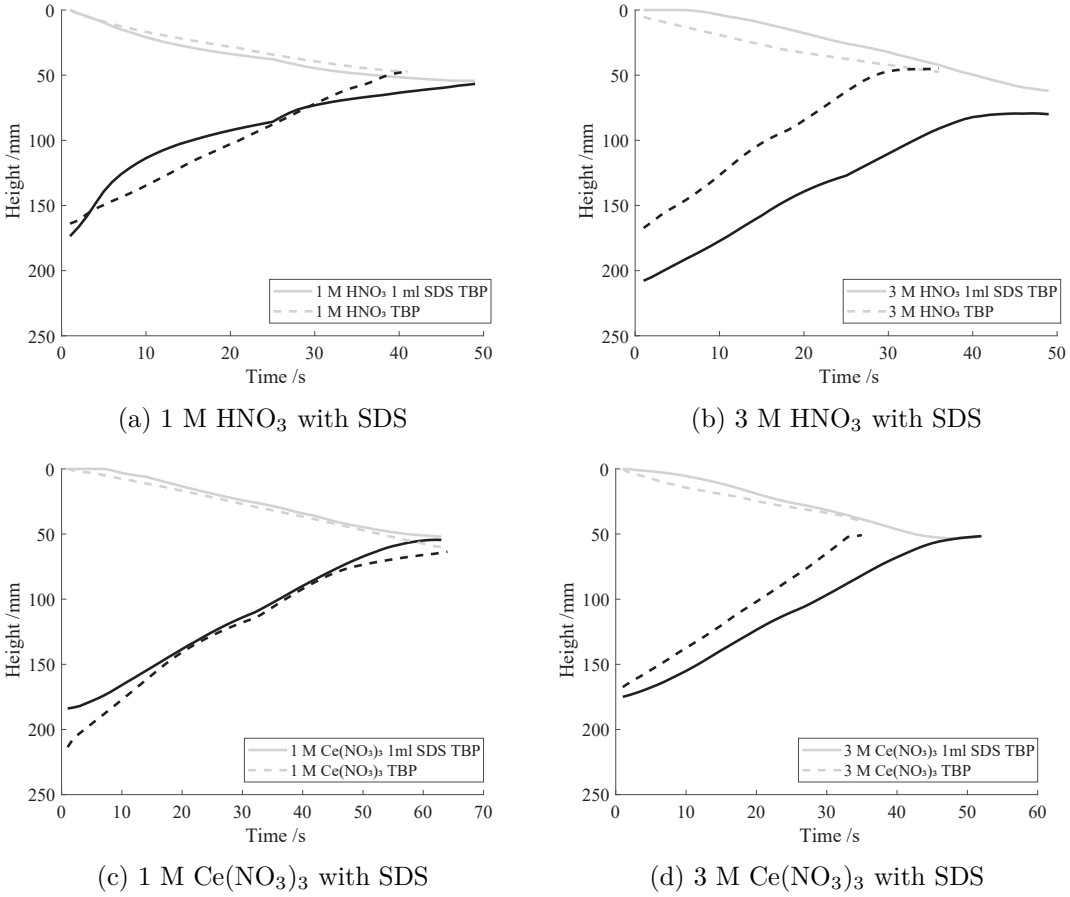

(a) 1 M HNO_3 with SDS

(b) 3 M HNO_3 with SDS

(c) 1 M $Ce(NO_3)_3$ with SDS

(d) 3 M $Ce(NO_3)_3$ with SDS

Figure 5.9: Improved dispersion stability for varying [HMI] concentration and $[H^+]$ with the addition of SDS. The aqueous, lower dispersion band is shown in bold, and the organic, upper band as grey lines.

It can be seen from Figure 5.9 that the addition of the surfactant increases separation time, however, not to the extent required. In Figures 5.9a and 5.9c the effect of the surfactant on dispersion stability is more prominent than it is for higher molarity systems, as shown in Figures 5.9b and 5.9d. Again, although the change to the system improved separation rates, increased dispersion stability, the increase still does not provide the

dispersion longevity required for use within the P-TS investigations. A dispersion stability greater than 30 minutes is required in order to conclude that separation within the P-TS is due solely to the enhanced separation provided and not gravity separation.

The ideal outcome of the P-TS investigations would be to show the effect of interfacial tension changes due to pH and [HMI] on separation efficiency. Therefore, it was concluded that the characteristics of the aqueous phase could not be changed. However, as preliminary tests showed that an aqueous system with an organic kerosene phase created a stable dispersion, a change in the organic phase was considered. The results of this are shown in Figure 5.10.

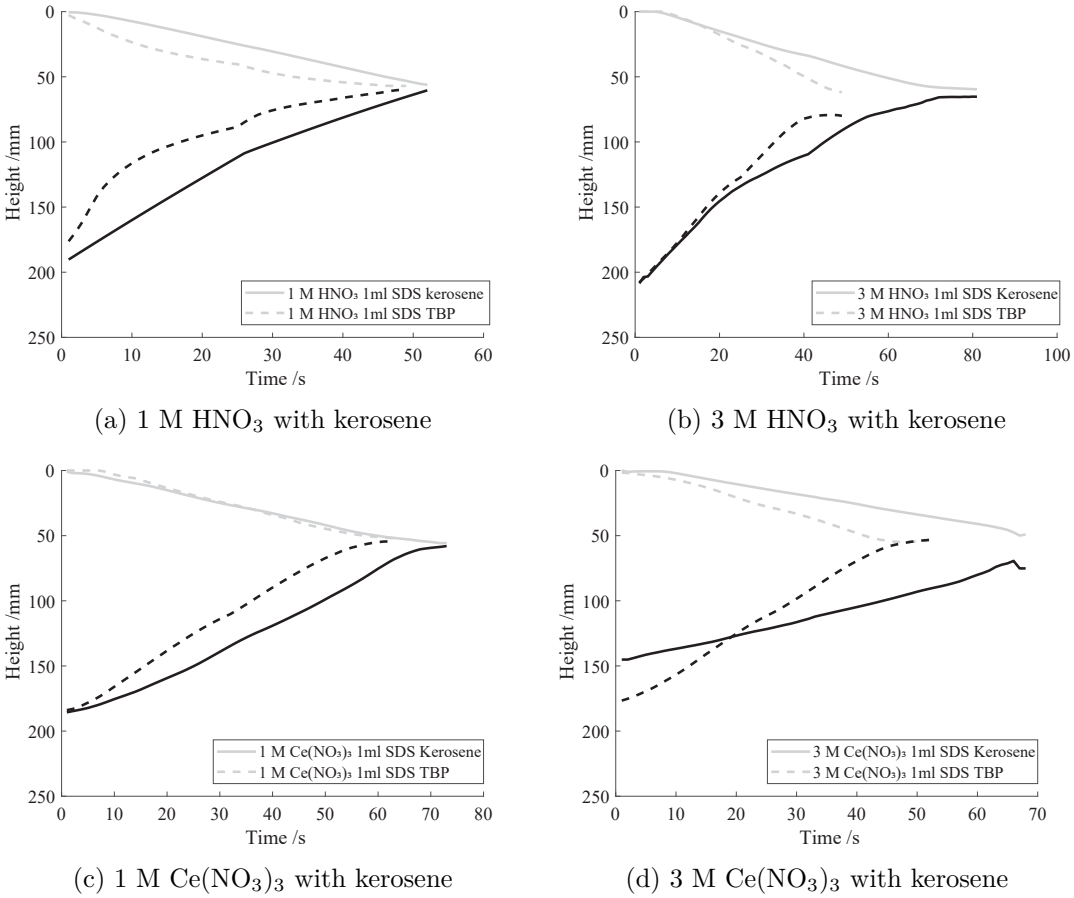

(a) 1 M HNO_3 with kerosene

(b) 3 M HNO_3 with kerosene

(c) 1 M $Ce(NO_3)_3$ with kerosene

(d) 3 M $Ce(NO_3)_3$ with kerosene

Figure 5.10: Comparison of dispersion stability between kerosene and TBP/n-dodecane organic phases. The aqueous, lower dispersion band is shown in bold, and the organic, upper band as grey lines

A change of organic phase to kerosene had a positive effect on the dispersion stability,

Figure 5.10. The effect was more prominent in the higher pH systems, Figures 5.10b and Figure 5.10d. No significant change for the lower [H^+] and [HMI] systems was observed. Although the change observed was positive, the dispersion separation rate remained below two minutes.

To mimic this viscosity increase the straight chain n-dodecane organic diluent was replaced with a branched chain dodecane, isododecane. Isododecane has a viscosity of $3.70\,mPa\cdot s$, which is $\approx 2.5\times$ greater than the viscosity of dodecane at 25 ℃[118]. Although this change provided a significant viscosity increase, the dispersion stability remained low and separation occurred within 3 minutes.

Due to the results found within this investigation and as the primary scope of this work is to develop an efficient separation device, the decision was made that a water-kerosene system will be used for the remainder of the investigation. This decision was made as a water-kerosene dispersion provides the desired stability longevity to ensure all separation achieved is solely a result of the P-TS and not sedimentation or gravity settling. Unfortunately, as a direct result of this decision, a study into the effect of [HMI] and [H^+] on the separation efficiency within the P-TS will not be completed within this thesis. Further work with radiation degradation products of TBP would be required in order to complete this secondary outcome.

5.2.2 Droplet size distribution analysis

The stability of a dispersion is inversely proportional to the size of the droplets within the dispersion[119]. Emulsions are the most stable form of dispersion with droplet sizes ranging between 0.2 - 50 μm. Droplets within this size range are often dominated by Brownian motion[29], remaining suspended as opposed to gravity settling. Droplets suspended in this way are known as entrained droplets, and are difficult to separate in traditional separation devices. Entrained droplets can be avoided by using low sheer pumping and mixing equipment, however, in an industrial settling it is unlikely they can be avoided completely.

Dispersion characteristics can be compared using a graphical representation of the

number of droplets within a dispersion and their respective diameters known as a droplet size distribution, DSD. Using the DSD, key parameters such as the mean and maximum/minimum diameters can be found, as shown in Figure 5.11[29]. Figures 5.11a and b, show a decreasing average and maximum, d_{50} and d_{MAX} droplet size after separation. Figure 5.11c shows the minimum droplet size that can be 100 % extracted by a separation process, d_{100}.

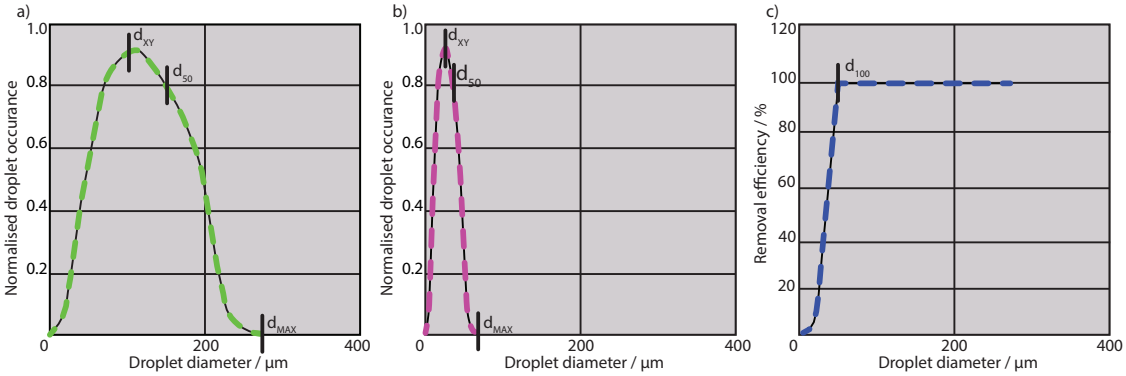

Figure 5.11: Schematic representation of typical parameters used to describe a dispersion where a shows the Droplet size distribution before separation, b - Droplet size distribution after separation, c - small droplet removal separation efficiency[29]

These parameters can be used to calculate commonly used mean values, $d_{[3,2]}$ and $d_{[4,3]}$. The Sauter mean diameter, $d_{[3,2]}$, is the ratio of volume to surface area providing an numerical representation of the overall spread of a dispersion, and is most commonly used in design procedures[120]. The DeBroukere mean, $d_{[4,3]}$ is the mean diameter over volume[120]. These values are effectively the centres of gravity of the respective distributions and are more accurate representations of dispersion characteristics than a traditional mean[120]. Within the case of P-TS design an argument can be made to support the use of either number as surface area and volume of the droplets will effect coalescence. With larger volume droplets more likely to slow within the flow and capture smaller, entrained droplets; and higher surface area, lower volume droplets providing a greater probability of a collision event resulting in coalescence due to their increased speed of collision. A generic equation

for the calculation of both $d_{[3,2]}$ and $d_{[4,3]}$ is provided[121].

$$d_{[x,y]} = \frac{\sum_{i=1}^{n} N_i d_i^x}{\sum_{i=1}^{n} N_i d_i^y} \tag{5.1}$$

where N is the number of droplets with diameter d_i[26,121]

It was decided that $d_{[3,2]}$ was to be used as opposed to $d_{[4,3]}$ even though there is a strong argument for the use of either within this application, as the use of $d_{[3,2]}$ is more compatible with what will be produced within mass transfer studies in future work if the P-TS is ever combined with a microfluidic mixing unit.

To determine the DSD upon entry and exit of the P-TS a technique for droplet size analysis is required. Different approaches and techniques for this have been developed over the past decade[122]. Many measurement techniques have been developed for measuring size distributions using the prinicple of laser backscattering, such as Focused Beam Reflectance Measurement (FBRM)[122]. However, primarily these techniques were developed for *in-situ* particle size measurements as opposed to droplet sizing. A review by Maaß *et al,*[122] found that laser backscattering is not feasible for droplet size measurements. The review compared the FBRM, two-dimensional optical reflectance measurement (2D-OFM) techniques and the fiber optical Forward-backward ratio (FBR) sensor to an *in-situ* photo-based endoscope. The dispersion tested was an immiscible water/toluene system. Each technique was required to measured the DSD of the system within a stirred tank reactor. It was found that for all three techniques, not only the size analysis but also the change in size over time gave unreliable results. As the techniques tested use the principle of laser backscattering to determine droplet size, the overall conclusion of the review was that the laser backscattering measurement principle cannot accurately be used for the online measurement of DSD[122]. Different reasons for this discrepancy in results have been suggested. One is that laser backscattering is not effective on a perfectly smooth shapes, as particles, unlike droplets, has a surface roughness value. However the most accepted explanation for the discrepancy is, the laser measurement techniques often measure the chord length distribution (CLD) as opposed to the actual droplet diameter distribution.

For spherical droplets the chord length is often significantly shorter than the droplet diameter. It is difficult to transform CLD data into a droplet size distribution. Models have been published to transform this data based on complete dispersions of perfectly spherical droplets, however, large errors are often found when comparing to results from experimental tests. Greaves *et al.*[123] found that FBRM underestimated the droplet size distribution for an emulsion. Boxall *et al.*[124] corrobrate this result, finding similar when measuring a dispersion of water in crude oil. Maaß *et al.*[122] state in their conclusions that direct photography still remains the most trustworthy technique for droplet diameter measurements.

Although direct photography and droplet counting have been reported as the most accurate methods for finding DSDs, there are many factors that must be considered when using these techniques. First, the camera used must have the correct focal range to give a high enough definition image at the correct magnification[122]. Next, the positioning of the camera must remain constant for all measurements as to not alter calibration between experiments. Once the camera is positioned, lighting of the frame must take into account reflections into the lens and potential loss of data in shadowed areas. Finally, the shutter speed of the camera must be adjusted to avoid blurred images of the travelling droplets. Three types of images were required to gain a true visual representation of the dispersion and flow characteristics within the P-TS. An overall image of the entire plate was required to see macroscopic flow structures. A microscopic view of three locations within the P-TS was required to show how the DSDs change along the plate length; and finally, a high magnification static image of the inlet and outlet dispersions was required to measure overall entrainment. Once image requirements were defined, the camera requirements and positioning could be set. Imaging locations are shown in Figure 5.12. Figure 5.12 shows the camera holder specifically designed to allow for perpendicular positioning of the cameras. Camera details are provided in Table 5.1.

Four 7 inch, white LED lighting panels with diffusers were located around the camera holder. Each lighting panel is adjustable by height, angle, brightness and lighting temperature. The lighting panels were adjusted iteratively by comparing the unedited images

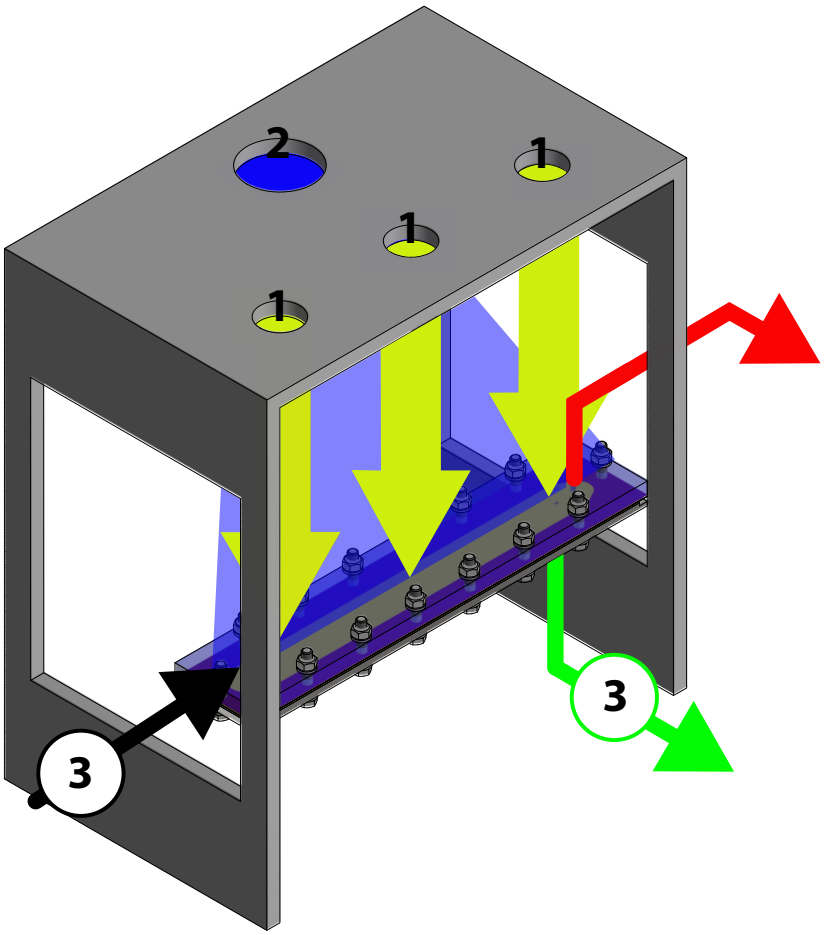

Figure 5.12: Camera Locations for droplet and overall plate views. The yellow represents cameras in location 1, focusing on droplet travel from the inlet, through the centre and finishing at the outlet. The blue represents the camera in location 2, capturing the bulk flow pattern. Circles in location 3 represent external droplet analysis of inlet and aqueous outlet.

with a threshold image to achieve optimal contrast. When the threshold image matched the unedited image the lighting was taken as correct. An example of this comparison is shown in Figure 5.13.

In Figure 5.13, some discrepancy can been seen between the threshold and raw image as indicated by the red circle. This discrepancy is the removal of an air bubble from the threshold image; removal of air bubbles was achieved by varying the threshold level to

only include the aqueous flow.

Table 5.1: Full camera details. Camera locations are shown in Figure 5.12

Camera Location	Model	Resolution / Megapixel	Working Distance / cm	Magnification
1	Dino-Lite AM4115TL	1.3	4 - 15	10 - 140x digital zoom
2	Oneplus One Smartphone camera	13	-	1
3	Long working distance objective lens*	-	20	10x optical zoom

Figure 5.13: Example of threshold achieved with final lighting set-up. a) shows an unediting image of the coalescer and b) the final threshold.

5.3 Summary

An investigation was undertaken to ensure a long lasting dispersion could be consistently be made. It was found that a 20 v% kerosene water dispersion, agitated at 2000 RPM provided the ideal dispersion behaviour.

Different methodologies for droplet tracking were considered with simple, visual techniques being found most appropriate. Stages of work to ensure consistent lighting, focus and threshold detail was undertaken. This stage was an iterative and highly necessary process. The outcome of this iterative process is unique to the lighting conditions at the experiment location, individuals looking to recreate this data will have to ensure this stage is completed.

CHAPTER 6

Effect of Plate Spacing on the Separation Efficiency of L-L Dispersions within a P-TS

The aim of this chapter is to find the effect of reducing confinement conditions within the P-TS on separation efficiency.

Using the methodologies developed in Chapter 5, plate spacing ranging between 50-1200 μm are investigated for volumetric flow rates of 1, 3, and 5 mL/min. The DSD and separation efficiency of each plate spacing and flow rate configuration are recorded. The overall outcome of this chapter is to create baseline results for direct comparison within Chapter 7, and to find the point at which confinement no longer occurs and the increased separation efficiency within the P-TS is reduced.

6.1 Final Methodology

The following methodology was used for all investigations, including plate spacing, textured plates and surface treatment investigations, in Chapter 7. Methodologies for textured and hydro-treated plates may differ slightly from what is described here, however, this will be described and labelled accordingly within the individual investigation.

All reagents used were 99% purity or higher from Fisher Scientific (Loughborough). All water used is ultra pure, deionized water from a MilliQ by Millipore water purification system (Millipore, Watford, UK). 1 mL of a 1 g/L SDS solution was added to the aqueous, water phase and gently mixed for 2 minutes. A small amount (< 1 g) of Sudan blue, organic dye, was introduced to the organic, kerosene phase and gently mixed until the solid was dissolved. Organic dye was used to enhance contrast between phases to improve visual detection of droplets.

Dispersions were produced in accordance with Section 5.2.1. A 250 mL, 70:30 Aq:Org water-kerosene dispersion was produced by high sheer, overhead mixing at 2000 RPM for 10 minutes. After mixing, the dispersion was left to settle for a further 10 minutes

and four samples taken. First, two drops of dispersion from a 1 mL glass pipette were dropped onto a microscope slide and covered with cover sheet. This small sample was used with the long working distance objective lens in camera position 3 (Section 5.2.2) to find the inlet DSD. Next, a 10 mL sample was taken and centrifuged to find the exact volume ratio of the dispersion. The proportion of organic is taken as the value, a, to be used within the mass balance calculations outlined below in Section 6.1.1. Finally, two 20 mL samples were taken into separate syringes, and the first attached to a syringe pump. This sample was introduced to the empty investigation-specific P-TS configuration at the desired volumetric flow rate. No results were taken from the first 20 mL sample. A second, dispersion-full syringe was introduced via the syringe pump, to the now P-TS configuration at the desired volumetric flow rate. This two stage process was required to ensure that the separation occurred at steady state. This two step process could be replaced by one large syringe, however, this was not feasible with the equipment used within this investigation. Overall and point specific images were taken for DSD analysis at camera positions 1 and 2, in accordance with Figure 5.12 from Section 5.2.2. These images were only taken for the second sample once steady state was achieved. A table (Table 6.1) is provided to denote the investigation-specific parameters used within the three design optimisation investigations.

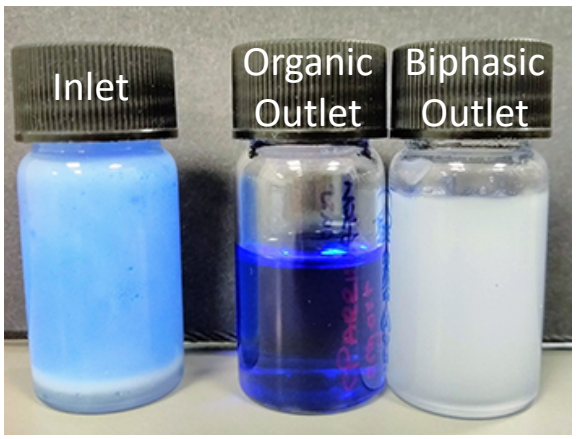

Figure 6.1: Example of the inlet dispersion, allowed to settle for 1 hour, and the organic and biphasic outlets

Post separation, the volume of clear organic phase, see Figure 6.1, was recorded and

taken as $\text{Vol}_{org,out}$ to be used in Section 6.1.1 below. As previously done with the inlet DSD, a two drop sample of from a 1 mL glass pipette of the biphasic outlet was placed onto a microscope slide and covered with a cover sheet; this small sample was used to find the outlet DSD using the methodology described in 6.2.2. The remaining volume of the biphasic outlet (Vol_{mix}) was centrifuged at 7000 RPM for 10 minutes to ensure phase separation. The centrifuged sample was carefully introduced into a 10 mL pipette with an error of ± 0.02 mL. Deionised water was used to rinse the centrifuge tube to ensure all organic is transferred to the pipette. The volume of entrained organic recorded as $\text{Vol}_{org,ent}$ below in Section 6.1.1.

Table 6.1: Investigation-specific plate configurations and flow rates. Note that SS* represents non-textured, non-treated stainless steel.

Chapter	**Upper Plate Material**	**Lower Plate Material**	**Flow rate/s (mL/min)**	**Plate Spacings (μm)**
6	PMMA	SS*	1	50, 100, 200, 300, 400, 500, 600, 1200
	PMMA	SS*	3, 5	50, 200, 600, 1200
7.1	PMMA	SS - Straight texture (SS-S)	1, 3, 5	50, 200, 600, 1200
	PMMA	SS - Crosshatch (SS-C)	1, 3, 5	50, 200, 600, 1200
	PMMA	SS - Straight to Outlet (SS-StO)	1, 3, 5	50, 200, 600, 1200
7.2	SS*	SS*	3	50
	SS*	SS-StO	3	50
	Treated-SS (T-SS)	SS*	3	50
	T-SS	SS-StO	3	50

6.1.1 Mass balance

A simple mass balance, shown in Figure 6.2, was used to aid in the calculation of separation efficiency and entrainment extent.

The volume of the organic and aqueous phases into the P-TS is determined using Equation 6.1. The value of a was determined by centrifuging a sample of the inlet dispersion, the procedure for which is described in Section 6.1. The values of Vol_{in} are known.

$$F1 = Vol_{in} = Vol_{org,in} + Vol_{aq,in} = [aVol_{in}] + [(1-a)Vol_{in}] \tag{6.1}$$

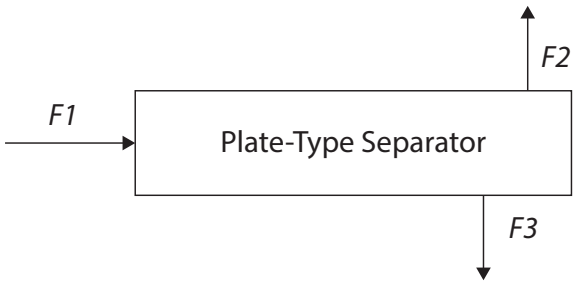

Figure 6.2: Simple mass balance across a P-TS where $F1$ is the dispersion inlet, $F2$ is the organic outlet and $F3$ the aqueous outlet and $F1 = F2 + F3$

The volume of organic out of the P-TS is split between streams $F2$ ($Vol_{org,out}$) and $F3$ ($Vol_{org,ent}$), the total volume is calculated in Equation 6.2. The error included within Equation 6.2 considers any volume remaining within the P-TS itself and is calculated using Equation 6.4. The values for $\text{Vol}_{org,out}$ and $\text{Vol}_{org,ent}$ are found experimentally following the methodology in Section 6.1.

$$F2 = Vol_{org,out} + Vol_{org,ent} + a(error) \tag{6.2}$$

The aqueous phase out of the reactor is only found in stream $F3$ and is calculated using Equation 6.3. The volume of aqueous cannot be directly measured experimentally as water is used to rinse glassware to ensure all entrained organic is accounted for and to reduce experimental error. However, the volume of the biphasic mixture out (Vol_{mix}) is first measured before any rinse water is added; the procedure for this measurement is shown in Section 6.1. The error within Equation 6.3 is the same as the error in Equation 6.2 and is calculated using Equation 6.4.

$$F3 = Vol_{mix} = Vol_{org,ent} + Vol_{aq,out} + [(1 - a)error] \tag{6.3}$$

$$error = Vol_{in} - Vol_{org,out} - Vol_{mix} \tag{6.4}$$

The results of the above mass balance are used to calculate the separation efficiency of the P-TS, Equation 6.5, and the percentage of entrained organic within the biphasic

outlet, $\%Org_{ent}$, in Equation 6.6.

$$\%Efficiency = [\frac{Vol_{Org,out}}{Vol_{in} + (a * error)}] * 100 \tag{6.5}$$

$$\%Org_{ent} = [\frac{Vol_{org,ent}}{Vol_{mix}}] * 100 \tag{6.6}$$

All experiments were completely in triplicate and the averages of the three separation efficiencies and extents of entrainment are reported within section 6.2.

6.2 Results and Discussion

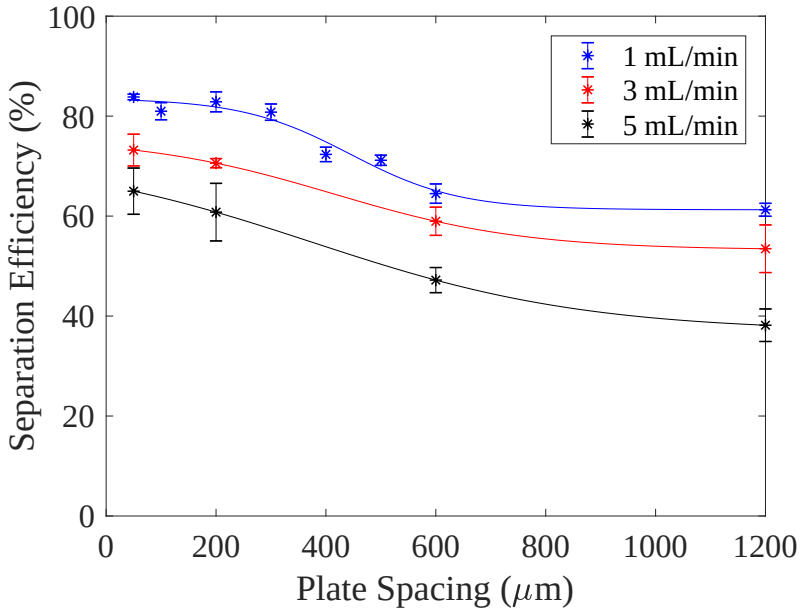

Figure 6.3: SS* plate efficiency.

Figure 6.3 shows a clear reduction in separation efficiency as the volumetric flow rate is increased. The average decrease that occurs is $\approx 10\,\%$ at each plate spacing when the flow rate is increased by 2 mL/min, i.e from 1 mL/min to 3 mL/min up to 5 mL/min. It can also be seen that the relationship between plate spacing and efficiency of separation is non-linear for all flow rates examined. It was found that the data was best fitted against

a logistic function or "S-curve" using the formula[125]:

$$f(x) = \frac{L}{1 + e^{-k(x-x_0)}} \tag{6.7}$$

where L is maximum difference between y-axis values, k the steepness of the curve and x_0 the x-value of the midpoint. The location of L and k are shown for the 1 mL/min system in Figure 6.4.

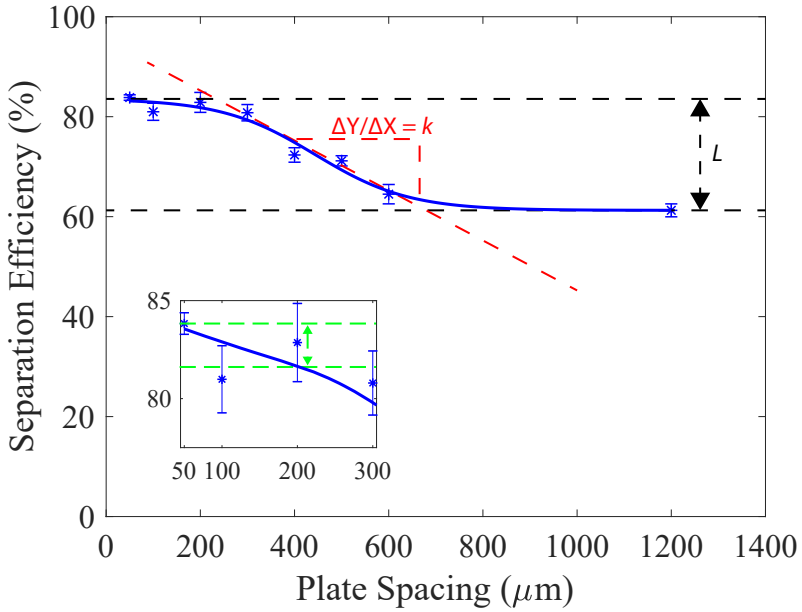

Figure 6.4: Annotated SS* plate efficiency for a 1 mL/min volumetric flow rate, showing the location of fitting parameters.

From the shape of the data, and the strength of the fitting (R-squared values), it can be confirmed that separation efficiency gradually deteriorates with increasing plate spacing until a spacing of between 200 - 300 μm. After this position, and until $\approx$600 μm, the rate of separation efficiency deterioration greatly increases. After this 600 μm position, the rate of change in separation efficiency decreases again into a plateau. This plateau remained stable until the largest plate spacing tested 1200 μm. The separation efficiency beyond this point was not considered, however, it is assumed that at a much larger plate spacing, the efficiency plateau will begin to reduce again, continuing to drop and tend towards zero.

Within this application of the Equation 6.2, the value of L , shown in Figure 6.4, can be considered as the total efficiency decrease between 50 μm and 1200 μm. With the 1 mL/min systems reducing by 21.9 % between over this range. To further understand the data, the gradient of the fitted decline can be considered. Within this application the gradient of the decline, k can be considered as the rate of change of separation efficiency with plate spacing, as shown in Figure 6.4. The value of this provided by the curve fitting is 4×10^{-2} %/μm.

The same values as above can be inferred by fitting an S-curve relationship to experimental values for 3 and 5 mL/min systems, as shown in Figure 6.3. The total deterioration of separation efficiency (L)observed for 3 and 5 mL/min systems are 21.5 %, and 26.8 % respectively. Overall, considering all three systems tested, the total deterioration in separation efficiency remains stable between the volumetric flow increase from 1 to 3 mL/min, however, decreases at the flow rate is further increased up to 5 mL/min. This could be due to increased droplet break-up at the increased rate of flow or a reduction in coalescence due to the reduction of time within the reactor. Conclusive evidence of which is more dominant cannot be made without considering the outlet DSD, this discussion is continued in Section 6.2.3.

The rate of reduction in efficiency with increased plate spacing between $\approx$ 300 and 600 μm, shown as k in Figure 6.4, was found to be 3.4×10^{-2} and 3.1×10^{-2} %/μm, for 3 and 5 mL/min systems respectively. This data is inferred from the S-curve fitted to experimental data, as the strength of the fitted data has an R-squared > 0.998 for both 3 and 5 mL/min. However, it is understood that the relationship may not exactly follow this trend as experimental data is not provided for these plate spacings. Considering the inferred relationship for the k values, it could be suggested that the rate of change of separation efficiency deterioration with plate spacing slows as flow rate increases. However, it is more likely that higher separation efficiencies can be achieved at larger plate spacing for lower flow rates, e.g. the efficiency drop-off position for a 1 mL/min volumetric flow rate occurs at a higher plate spacings than it does for 5 mL/min. This hypothesis is supported by comparing the overall separation drop between 50 and 200 μm; overall the

efficiency decrease between these heights at 1 mL/min is 1.03 % in comparison for 3.6 % and 6.5 % for 3 and 5 mL/min. The methodology of this calculation for the 1 mL/min system is shown in green in the inset of Figure 6.4, the same methodology was used to calculate the 3 and 5 mL/min values.

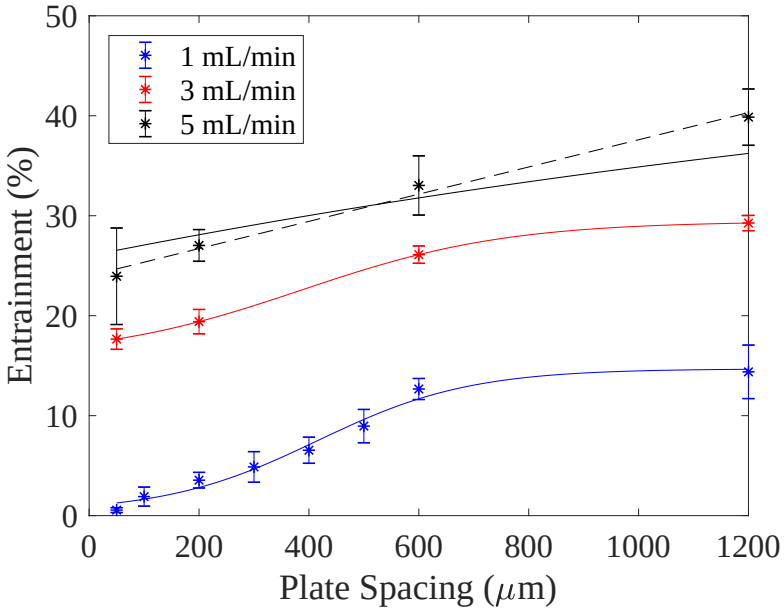

Figure 6.5: SS* percentage of aqueous entrained

This trend can also be observed when investigating the variation in the magnitude of entrained organic found in the aqueous outlet with plate spacing, as shown in Figure 6.5. As with the separation efficiency data, an S-curve could be fitted with strong agreement for lower flow rates. A linear fitting, shown as a dashed line Figure 6.5, provided a greater value of R-squared for 5 mL/min, suggesting that the strength of the relationship found reduces with plate spacing, to confirm this more data points would be required. Comparing the relationship between droplet entrainment within the aqueous outlet and plate spacing, it is clear to see that as plate spacing increases so does the value of droplet entrainment, which is also supported by the reduction in separation efficiency. Looking into the effect of flow rate on this relationship, the curve fitting parameters can again be compared. The overall entrainment increase, L in Equation 6.2, observed at 1 mL/min is 14.9%. This trend steadily increases to 15.4% for 3 mL/min and 16.4% for 5 mL/min. This increase

mimics the L values observed within the separation efficiency data, therefore, confirming that as separation efficiency decreases, the volume of organic within the biphasic outlet increases.

The gradient term, k from Equation 6.2, for the entrainment study is analogous to the increase of percentage entrainment with plate spacing. When comparing the gradient change between $50\,\mu m$ and $200\,\mu m$, it is found that the rate of change of entrainment with plate spacing is higher at 5 mL/min, which has a gradient change of $1.8\times10^{-2}\,\%/\mu m$ in comparison to $1.5\times10^{-2}\,\%/\mu m$ for 1 mL/min (based on the linear fitting for 5 mL/min). Looking at the effect at larger plate spacings, this trend switches and gradient values between plate spacings $200\,\mu m$ and $600\,\mu m$ increases faster for 1 mL/min with a gradient of $2.2\times10^{-2}\,\%/\mu m$ in comparison to $7.8\times10^{-3}\,\%/\mu m$ at 5 mL/min. This, again, is in support of what was observed within the separation efficiency investigations. The relationships discussed between entrainment and separation efficiency with increasing plate spacing will need to be taken into account when designing the P-TS for an industrial flow sheet. As discussed in Chapter 3, the ease of which droplets will coalescence is effected by changes in pH, [HMI] and the v% of ligand within the organic phase. For systems with fast coalescence rates, i.e. a high concentration HMI system could be separated to the desired extent with a larger plate spacing and higher volumetric flow rate. Whereas, in a dilute HMI system i.e. towards the back end of the extraction flow sheet, a smaller plate spacing and lower flow rate may be necessary to achieve the desired separation.

Comparing the two data sets together, it can be concluded that at low plate spacings the separation efficiency increases and therefore, droplet entrainment is reduced. For higher flow rates, separation efficiency is initially reduced (at low plate spacings) however, the rate of deterioration of separation efficiency with plate spacing reduces for lower volumetric flow rates. Confinement theory, described in Section 4.1, suggests that the increased separation efficiency due to the microfluidic nature of a device is only apparent when confinement is greater than 0.2[82]. Figure 6.6, clearly shows the position at which confinement is reached within this system.

From Figure 6.6, we can confirm that there is a rapid decrease in separation efficiency

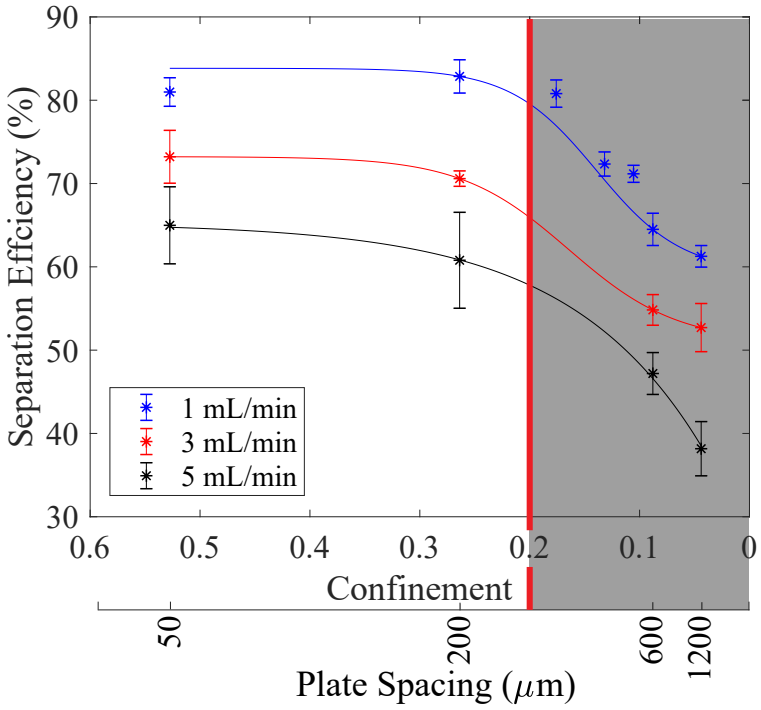

Figure 6.6: Effect of confinement on separation efficiency

for all systems tested as plate spacing is increased to outside of confinement conditions (< 0.2, $\approx$, $> 300\ \mu m$). Whereas, increasing confinement conditions beyond 0.2 has a negligible effect on the separation efficiency. When considering this negligible change in terms of confinement, it is concluded that the separation efficiency increase achieved through increasing the confinement (reducing plate spacing) is not a sufficiently high enough gain to offset the large increase in pressure and loss of volumetric throughput experienced.

6.2.1 Comparison to gravity separation

The reasoning behind this research is to find an efficient method of separation in comparison to industry standards. Figure 6.7 showns a comparison between the separation efficiencies found for the P-TS and the separation extent of a gravity separating system. Both figures show the separation of 30% kerosene/water dispersion. The data in Figure 6.7 was prepared and recorded using the mixing methodology discussed in Section 5.2.1

and the separation extent calculated using:

$$Separation\,extent = 100 - \left(\frac{Height\,of\,dispersion}{Total\,height} * 100\right) \tag{6.8}$$

where the height or dispersion and total height are indicated in the Figure 6.7b inset.

The bulk separation time calculated for Figure 6.7a was calculated using

$$Separation\,time = \frac{Volume\,of\,P-TS}{Volumetric\,flow\,rate} \tag{6.9}$$

This is not being used as the true residence time of the P-TS as a residence time distribution (RTD) was not recorded. In comparison to literature, the bulk separation time used within this study will be a slightly under estimatation of residence time, as literature has found the droplets tend to travel at the same rate as the bulk[31,35]. Bulk separation time is used as a value to indicate the time the bulk flow is within the P-TS.

It is noted that as the reactor volume change within this investigation is achieved through increasing the channel height as opposed to the channel length, the data shown in Figure 6.7a is not as traditionally expected. Here it is seen that, the separation efficiency decreases with increased time within the reactor. This is due to the loss in wall effects and confinement experienced when the channel height and therefore reactor volume is increased.

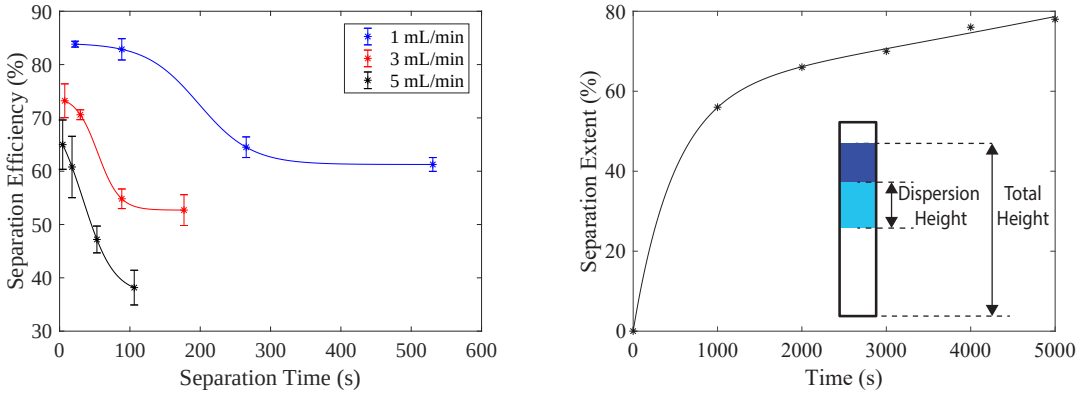

(a) Effect of separation time on separation efficiency for a SS* P-TS

(b) Separation extent over time for a gravity separating system

Figure 6.7: Comparison of separation time for P-TS and gravity separating systems

It can be seen in Figure 6.7b, that the dispersion separation rate is initially fast, reaching *approx* 60 % separation in 1000 seconds (16 minutes), however, after this time the rate begins to a plateau. The separation increase over the next 60 minutes is 23 %. The separation continued for several hours (not recorded) with a reducing rate. Often a thin dense layer of dispersion remained 24 hours later. Comparing the data in Figure 6.7b with that of Figure 6.7a, it can be seen that the gravity settled separation efficiency achieved within 60 minutes (78 %). Using Figure 6.3, it was found that an equivalent 78 % separation efficiency can be achieved within a $\approx 330\,\mu m$ P-TS at 1 mL/min. The separation time with this configuration P-TS to achieve 78 % was ≈ 160 s. In this case, the P-TS is 95 % faster than gravity settling.

The fastest separation time investigated with the P-TS was 4.4 s with a flow rate of 5 mL/min and plate spacing of $50\,\mu m$. Under these conditions, a separation efficiency of 65 % was achieved, this is considered a substantial achievement due to the speed of the separation. Under gravity settling conditions the same separation extent took ≈ 30 minutes resulting in an improvement of 409×. A comparison between the most efficient separation, 83.8 % achieved at a $50\,\mu m$ plate spacing and 1 mL/min, was made by extrapolating the data shown in Figure 6.7b. Under gravity separation conditions, 83.8 % was achieved in ≈ 6200 s. The same separation efficiency within the P-TS had a bulk separation time of 66 s, this is a 98.9 % improvement in comparison to gravity separation.

6.2.2 Droplet size distribution methodology

With the aid of Dr. Keeley (University of Leeds, School of Electronic and Electrical Engineering) a MATLAB script was written to streamline the droplet counting process. The script was verified via manual droplet counting. The methodology used to create this script is described below.

The script first sets a known circle radius, then loops though different intensity threshold levels to find all circles/droplets with an equal radius to what was previously set. This process is completed using the imfindcircle function. The centre x-y coordinates and radius for all droplets with the corresponding radius are found and recorded. This procedure

is repeated for increasing droplet radii, where the maximum droplet radius was set much higher than the expected max so that no droplets are missed.

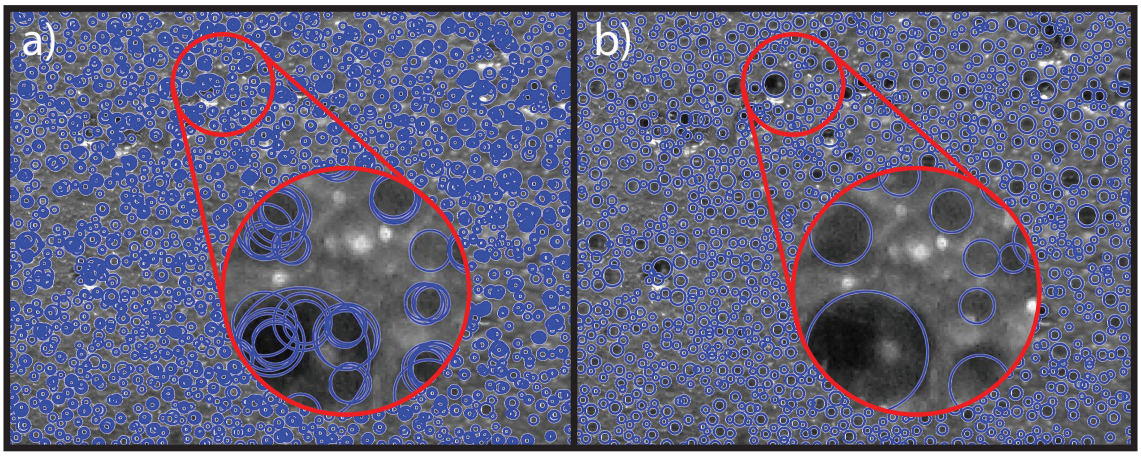

Figure 6.8: Development of droplet counting code a) droplets identified after initial processing loop. b) Final identified droplets

The result of the first stage of iterations is the known x-y location of the centre of all droplets and the corresponding radius from all threshold intensities. As some droplets will appear in multiple threshold intensities, repeats must be removed. This is achieved by rounding the centre locations to integer numbers of pixels to avoid sub-pixel difference caused by thresholding. Next droplets with identical x-y locations and radii are counted as one, removing droplets found in multiple thresholds. The results at end of this process are shown in Figure 6.8a.

After this initial stage, it was found that the frequency of droplet occurrence was higher than the actual value. Viewing the visual output from the code, Figure 6.8a, it was found that often the same droplet was found for multiple radii depending on the threshold level and further processing was required. To address this, a second processing loop was included to remove these droplets.

Droplet radii are sorted from largest to smallest, and the largest droplet added to a list of unique droplets. The remaining droplets are now checked to see if the droplet center is within the radius of all larger droplets in the new unique list, if the droplet does not overlap with any larger bubbles (in the unique list), it is recorded to the list of unique

droplets. This processing loop is ended after all droplets are checked and the results of this are shown in Figure 6.8b.

It was found that when comparing the results of multiple different systems with manual droplet counting using the software packed ImageJ, excellent corroboration between DSDs was found. A limitation of this code is that only circular droplets are counted and therefore non-circular droplets within the flow, such as slugs or elongated flow structures are not included in the final DSD. A further limitation of the code is that only droplets in focus will be counted. However, if the cameras are well calibrated this should not prove to be an issue as the focal plane of all images will be equal.

The output of the MATLAB script is an individual DSD. These have been combined to make Figure 6.9.

6.2.3 Effect of plate spacing on DSD

The effect of plate spacing on the droplet environment within the plate is still yet to be defined. Figure 6.9 shows the average DSD of the biphasic outlet at each plate spacing, and the average inlet of all tests. The average inlet, Inlet*, of all tests is used throughout this thesis as a comparison to outlet and other location DSD. In was chosen that Inlet* would be used as a direct comparison between different systems and, as excellent correlation between inlet dispersions was achieved. The flow rate used to produce Figure 6.9 is 1 mL/min, other flow rates are not shown as the affect of flow rate on droplet distribution is discussed in further detail in Section 7.1, however, there was a strong correlation of trends between the different flow rates tested.

From Figure 6.9 it can be seen that overall the frequency of droplet occurrence decreases with plate spacing, as supported by trends within the entrainment data shown in Figure 6.5. A decrease in plate spacing can also be seen to cause a decrease in the overall size and spread of droplet diameters within the outlet, shown in Figures 6.10a and b. In Figure 6.10a, the data span of the distribution was calculated by finding the width of the distribution at a droplet diameter 70 % less that the d_{max}, this position was chosen so the data span was not effected by the noise within the lower diameter data. A linear

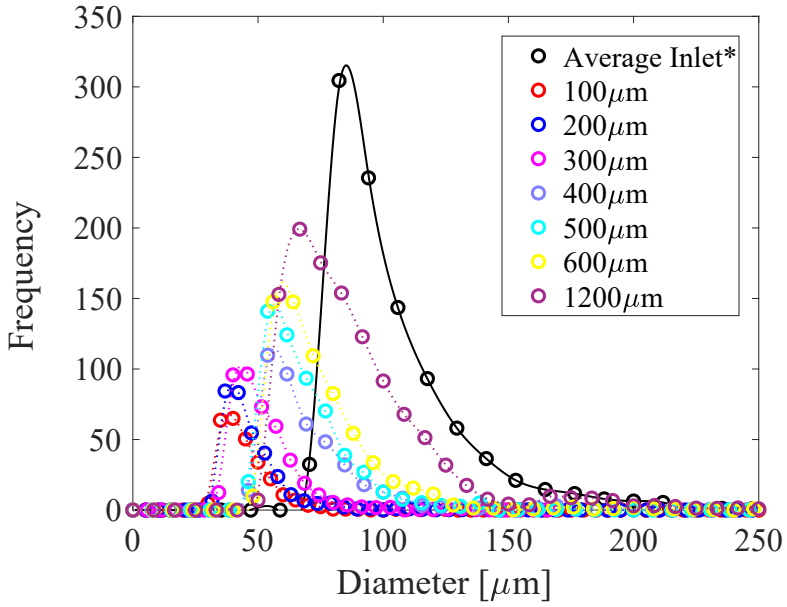

Figure 6.9: Comparison of plate spacing and droplet size distribution SS* (1mL/min)

relationship between the spread of the data with increased plate spacing was found. Figure 6.10b, also shows a general increase of $d_{[3,2]}$ with plate spacing.

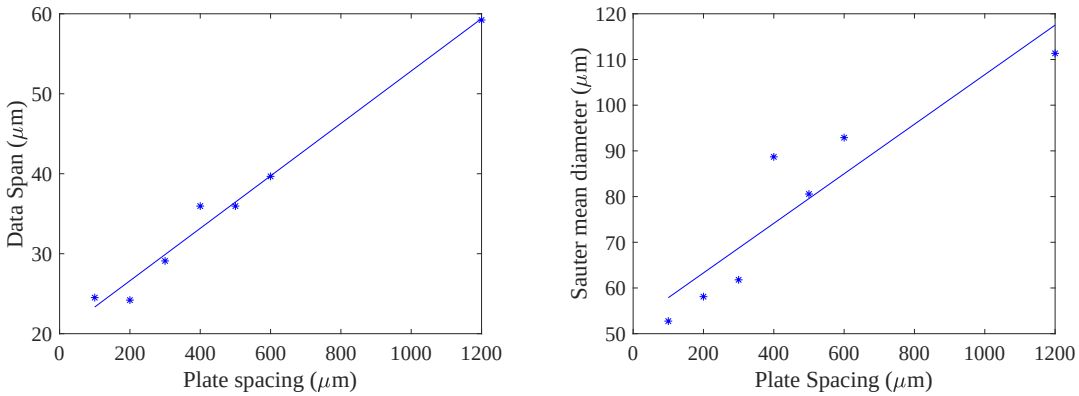

(a) Spread of DSDs 70 % less than the d_{max} for increasing plate spacings.

(b) Variation of $d_{[3,2]}$ with increasing plate spacing for a 1mL/min flow rate

Figure 6.10: Effect of plate spacing on the outlet droplet size distributions of a 1 mL/min system

In Section 4, it is discussed that the Peclet (Pe) and capillary (Ca) numbers can be used to determine the type of coalescence occurring and the likelihood of a droplet coalescencing within a flowing system, respectively. Using the equations within Section

4, and $d_{[3,2]}$ values, Peclet and capillary numbers can be calculated for the different plate spacings and flow rates, and are shown in Figures 6.11 and 6.12. The critical capillary number was estimated by using be p and p_{crit} term in Equation 4.4.

In Section 4 it was discussed that when $Pe >> 1$, then flow-driven coalescence is dominant. It was found that the Pe number is greater than 1 for all flow rates and plate spacing, therefore a flow driven coalescence model is confirmed. The only variable factor within the Pe number formula, Equation 4.1 in Chapter 4, is the hydraulic diameter, d_h, which only varies by the height of the channel. Figure 6.11 shows the effect of reducing confinement on the Pe number. The value of $Pe = 1$ is shown in green. The constants used in the calculation of these values are provided in the nomenclature.

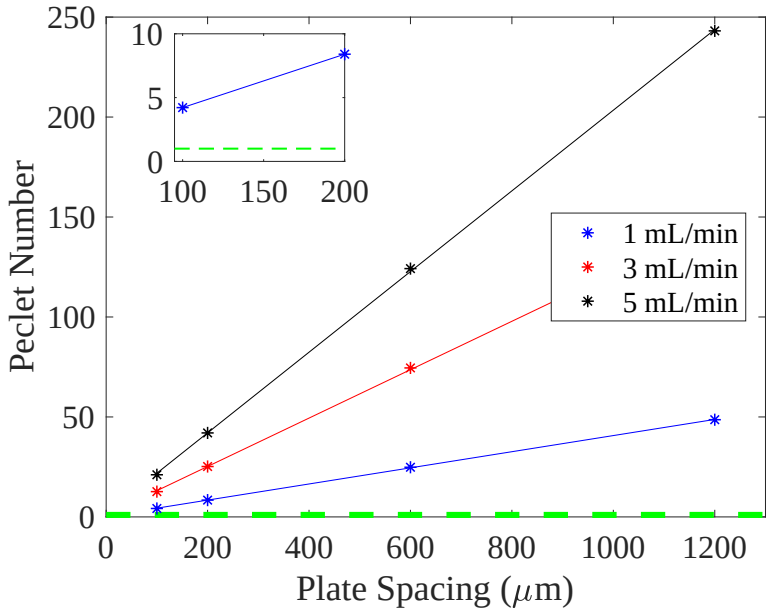

Figure 6.11: Use of Peclet number to determine coalescence model for various plate spacings and flow rates

It can be seen that at lower plate spacings the coalescence model tends towards a diffusion driven model as opposed to flow-driven. This trend is understandable as droplets have less space to occupy in confinement and are therefore forced together. It could be proposed that the high separation efficiencies within the P-TS are due to the coalescence of flowing droplets within the static droplet regime. However, if this were true the separation

efficiency achieved at 50 μm and 5 mL/min would be highest. Therefore, droplets at higher flow rates, when the $Pe \approx 1$, experience greater droplet break-up than those at lower flow rates.

As Pe is greater than 1 for all cases, the relationship between droplet coalescence and break up can be determined by the relationship between Ca and Ca_{crit}, with droplet break up occurring more frequently as Ca moves towards Ca_{crit}, shown in green in Figure 6.12a. It can be seen that the value of Ca gets closer to Ca_{crit} as the plate spacing is decreased, which is due to the increased shear rate experienced in confinement. The shear rates within the study are in the range of $1{\times}10^{+3}$ this is comparable to those found by Chen *et al.* with a similar P-TS configuration[33].

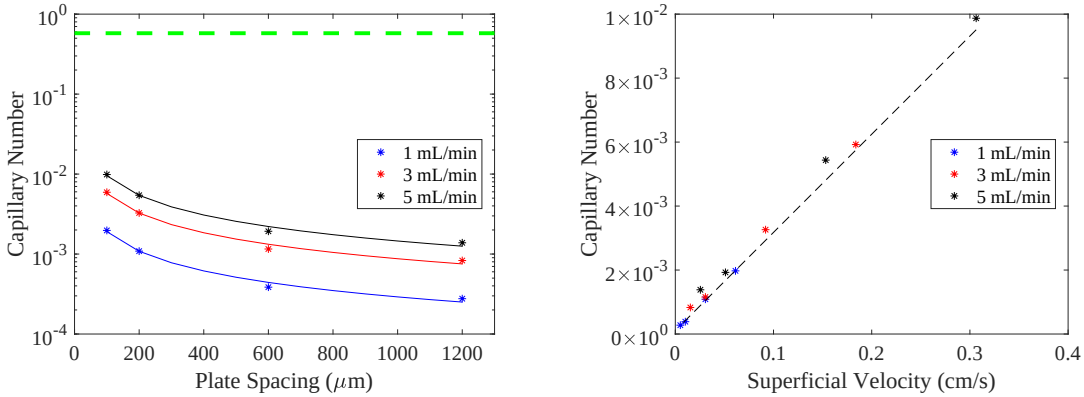

Figure 6.12: Variation of Capillary number with plate spacing and superficial velocity

Although the relationship between plate spacing and Ca has yet to be discussed in literature, Chen *et al.*[33] found a linear relationship between Ca and increasing superficial velocity. In Figure 6.12b, it is shown that the same relationship was observed within this investigation.

6.3 Conclusions

Within this investigation it was confirmed that the P-TS is a highly efficient method for the separation of fine droplet immiscible dispersions.

The efficiency of separation is greater in highly confined situations (lower plate spacings) and lower flow rates. As plate spacing is expanded, a non-linear reduction in separation efficiency is observed for all flow rates. The point at separation efficiency deterioration increases with plate spacing occurs at higher plate spacings for reduced flow rates. Therefore, low flow rate systems maintain the ideal, confined separation conditions at higher plate spacings than higher flow rates.

It can be concluded that the separation times and separation efficiencies achieved are significant improvements to gravity separation of the same dispersion. With the fastest separation time providing a 409× improvement and the shortest separation time a 98.9 % improvement. The increased separation efficiency is the direct result of confined, wall effects within the P-TS.

CHAPTER 7

Application of Physical and Chemical Surface Variations on the Separation Efficiency of L-L dispersions within a P-TS

There are two overall aims for the work within this chapter. First, the effect of introducing surface textures into the reduced confinement conditions experienced within the P-TS on separation efficiency is investigated. Using the methodologies developed in Section 6.1, plate spacings ranging between 150-1300 μm are investigated for flow rates of 1, 3, and 5 mL/min on three different plate textures, shown in Table 6.1. Plate spacings are increased to allow for the 100 μm texture height. The DSD and separation efficiency of each plate spacing, flow rate and texture configuration are recorded. The results of this investigation are compared to those found in Chapter 6.

Following from this, the plate configuration with the most potential is investigated further, by looking into the effect of replacing the upper PMMA plate with SS and a hydrophobic coated stainless steel (T-SS). The overall outcome of this chapter is the final design of an optimised P-TS constructed in industry appropriate materials.

7.1 Textured Plates

From reviewing current literature on the P-TS in Section 1.4, it was concluded that extensive work had been undertaken to find the effect of plate geometry on separation efficiency within a P-TS device. This work covered the effect of plate spacing (over a shorter range than what is covered within this thesis)[31,32], plate length and plate width[35]. For this reason it was decided that rather than alter the geometry of the plate as before, textures would be applied to the surface to introduce slight turbulence and promote the potential break up of emulsions formed during dispersion creation.

7.1.1 Formation of droplet structures within reducing confinement

Within the tests completed in Chapter 6, it was observed that in high confinement, thin flow structures were formed, as shown in Figure 7.1. These structures grew in length and width with increased plate spacing. To determine a quantitative result from these images a MATLAB script was written to count the number of interfaces in a 1 Pixel slice of the reactor. Examples of this procedure are shown in Figure 7.2. Within this chapter, the interface is a macroscopic term considering the bulk flow. The definitions of interface should be considered as the outline of a slug, between the aqueous and organic phases.

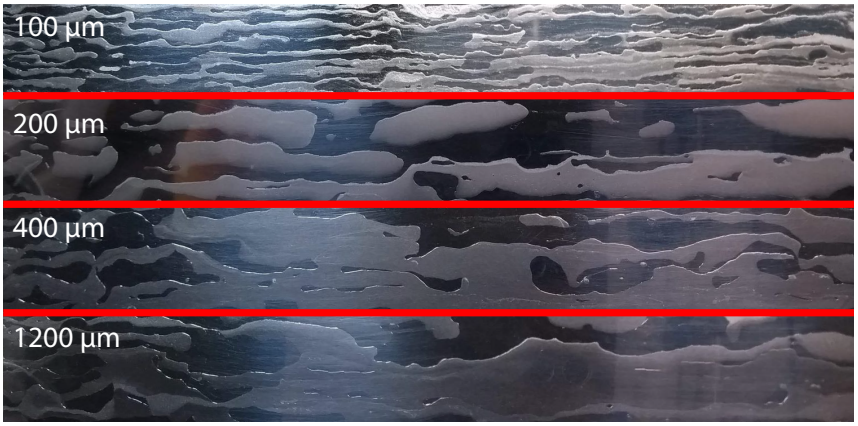

Figure 7.1: Bulk slug flow showing a visual change in flow behaviour with increasing plate spacing.

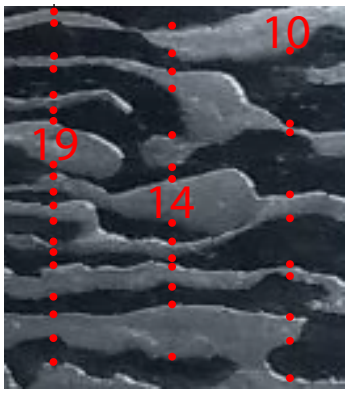

Figure 7.2: Examples of interface counting followed to determine a numeric value for change of flow behaviour with plate spacing. Each red dot represents a counted interface. Using MATLAB this process was repeated for 1 Pixel slices of the reactor.

Following this procedure, the results showed high correlation to the threshold image

as shown in Figure 7.3, which shows that the number of interfaces decreases at a length of $\approx 8\,\text{cm}$, when the density of white flow structures is at its lowest. The results from three experiments at three different plate spacings are shown in Figure 7.4.

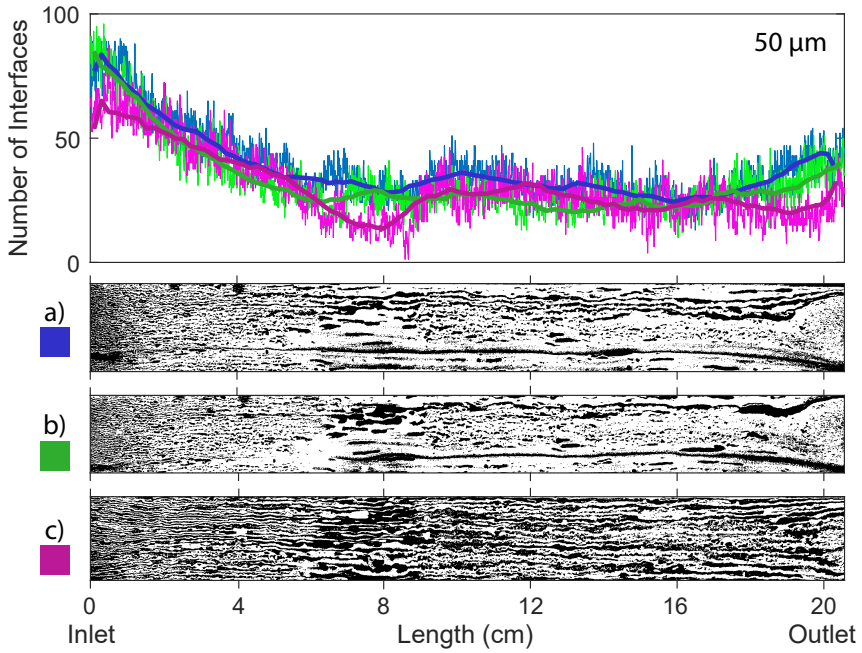

Figure 7.3: Comparison of the number is interfaces across the width of the flow channel for a $50\,\mu m$ plate spacing, where a,b and c represent three separate experiments

In Figure 7.4, it can be seen that as plate spacing increases the overall reduction of the number of interfaces decreases and by $400\,\mu m$ the interface number across the width of the plate remains stable for the entire length. Relating this back to what is now known about the relationship between plate spacing and separation efficiency, it is apparent that an increased number of interfaces increases the extent of separation. This is most probably due to a reduction in distance a droplet has to travel before reaching its 'like' phase. For example, consider two slugs travelling at equal bulk velocity one in a $50\,\mu m$ channel and the other in a $400\,\mu m$. A droplet within the centre of the larger, $400\,\mu m$ slug has a greater lateral distance to travel before reaching its 'like' phase to coalesce.

From Figure 7.4 a clear decrease in the number of interactions across the width of the channel in the first 8 cm is apparent for only the $50\,\mu m$ plate spacing. It is assumed this is due to the break-up of droplets with a diameter greater than the plate spacing upon entry

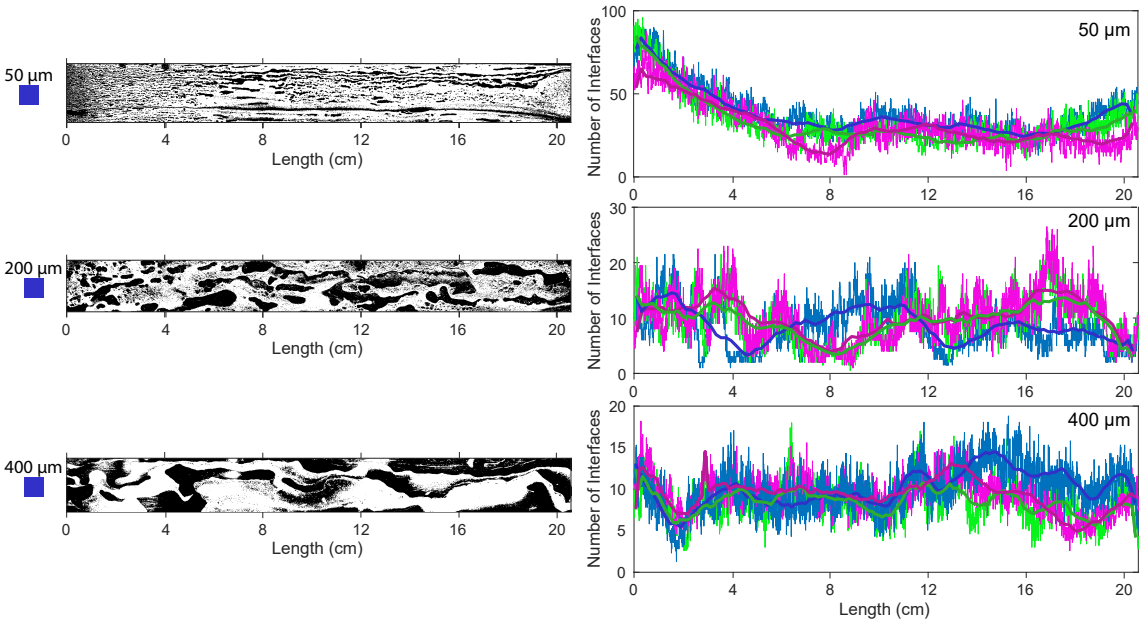

Figure 7.4: Comparison between number of interfaces across the width of the channel for increasing plate spacings

to the P-TS and sudden increase of pressure. As these droplets coalescence, the width of the slugs increases, until the steady state observed after then $\approx 8\,\text{cm}$ length. Droplets entering the $200\,\mu m$ spacing feel a much lower pressure increase due to the increase in cross-sectional areas, and do not have this sudden break up. To investigate this further the DSDs taken at entry, centre and outlet positions, as shown in Figure 5.12, can be compared.

It can be seen that in Figure 7.5a, the inlet DSD dispersion is higher than those seen in Figures 7.5b and c. This reduction in droplet coalescence supports the hypothesis proposed above, confirming that the large reduction in the number of interactions across the width of the plate in the first 8 cm at $50\,\mu m$ is due to an increase of droplet break up as a result of high confinement and the resulting an increase in pressure. It should be noted that the DSD recorded in the spot camera locations, location 1 in Figure 5.12, will not be as accurate as the stationary inlet and outlet images (camera location 3 in Figure 5.12) due to a blurring or 'halo effect' around the flowing droplets caused by droplet elongation due to wall effects. Therefore the droplet counting code described in Section 6.8 will report

lower values than the true reading. This limitation predominately occurs above a plate spacing of 200 μm, as multiple layers of droplets are being recorded as the inlet DSD is less than the plate spacing. This is shown in the insert in Figure 7.5c

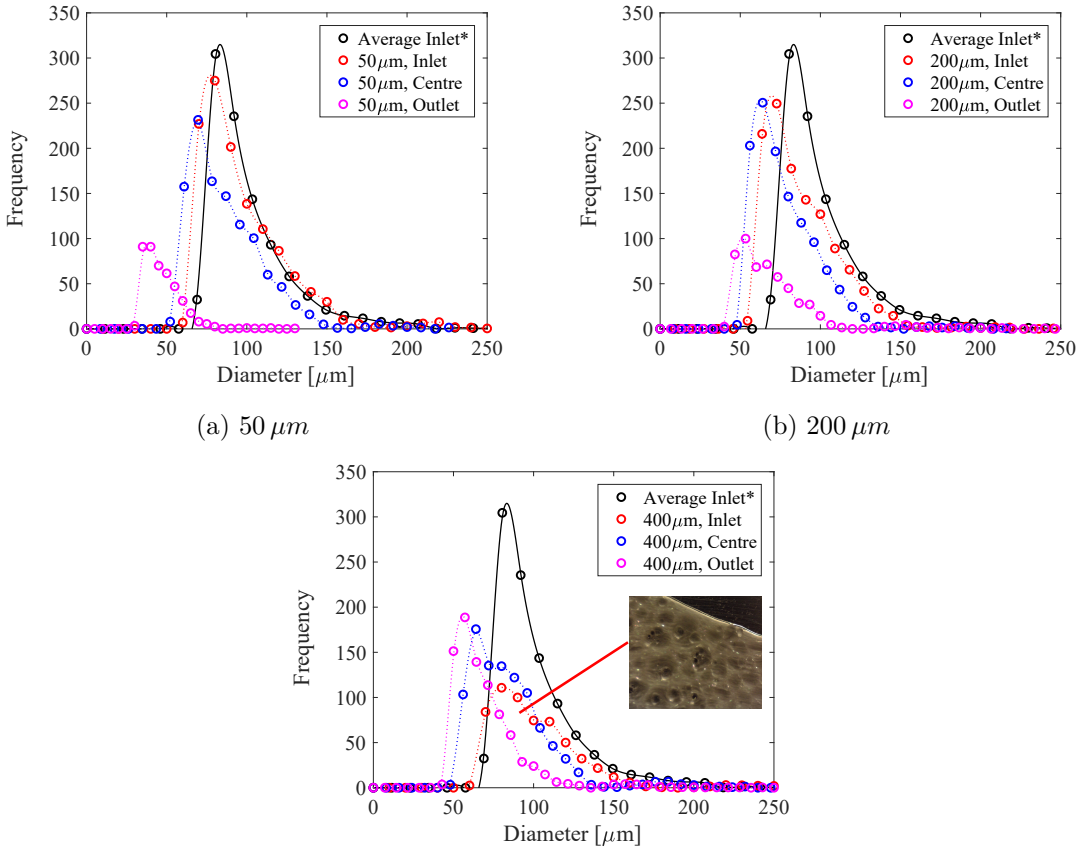

(a) 50 μm

(b) 200 μm

(c) 400 μm

Figure 7.5: DSD for spot location analysis as shown by camera location 2 in Figure 5.12 for increasing plate spacings

As it was found that spot location analysis had reduced accuracy above a plate spacing of 200 μm, DSD for spacings above this value will not be discussed. Although multiple droplet layers were observed within the 200 μm plate spacing, manual droplet counting provided verification of the DSD produced using the droplet counting script. It was concluded that when the number of droplet layers increased above two the reduced accuracy occurred.

Figure 7.6 was produced to shown the relationship between the DSD of different plate

spacings at the three locations investigated. It can seen that at the inlet of the P-TS, Figure 7.6a, the overall droplet size is higher for smaller plate spacings and the overall number of droplets is larger. This again supports that at lower plate spacings droplet break-up is higher within the initial 8 cm. However, comparing both inlet DSD there is an overall reduction in the droplet diameter in comparison to the average inlet*, therefore suggesting that inlet droplet-break up occurs for all confined plate spacings (50 - 300 μm as indicated by Figure 6.6), with the magnitude of the effect increasing with increased confinement. Further down the plate the DSD produced at the centre, Figure 7.6b, shows the lower plate spacing droplet diameter and frequency has reduced in comparison to the 200 μm. Figure 7.6b also shows that coalescence has occurred between the inlet and centre locations as indicated by the reduction of droplet frequency in comparison to the average inlet. Greater coalescence has occurred for the lower plate spacing. Finally, reviewing the data provided in Figure 7.6c, retrieved from the outlet location, significant coalescence has occured in both cases as droplet frequency has reduced. The data also shows that the majority of coalescence achieved was of larger droplet diameters, indicated by the reduction in droplet diameters.

A discrepancy can be seen between the two outlet camera locations (shown as locations 1 and 3 in Figure 5.12). The solid line plotted on Figure 7.6c is the static outlet DSD recorded in camera location 3, for a 200 μm plate spacing, shown as Outlet* in the figure legend. This discrepancy is thought to be the result of the coalescence of larger droplets occurring in the time from the spot analysis outlet location and final DSD imaging.

Textures were applied within the inlet area to promote increased velocities and introduce slight turbulent mixing into the system. It was proposed that the introduction of slight mixing within this first portion of the P-TS would reduce the speed of smaller droplets within the centre of large slugs and increase the number interfaces across the width within this area. Textures were not extended the entire length of the plate so that turbulence produced within the texture area can dissipate and laminar, confined coalescence can occur.

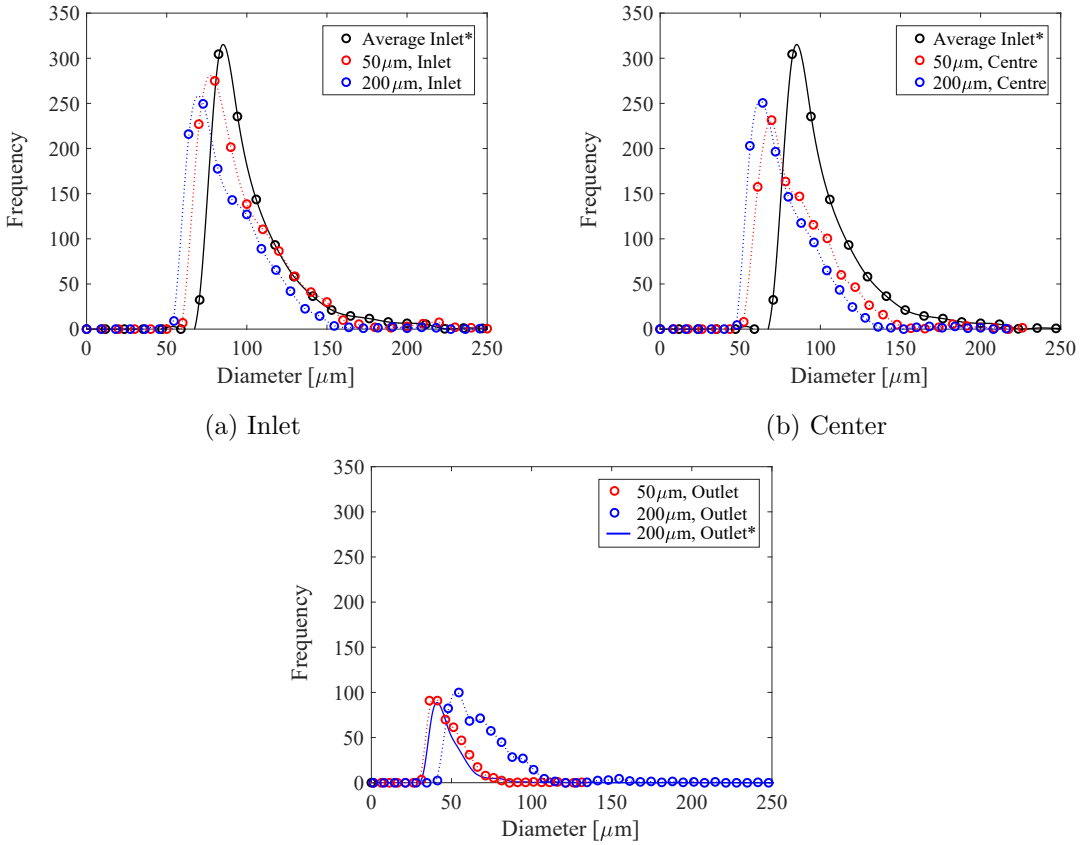

(a) Inlet

(b) Center

(c) Outlet

Figure 7.6: Comparison of droplet size distribution recorded at different spot locations with increasing plate spacings

7.1.2 Texturing of stainless plates

Texturing of the stainless steel was achieved using a LPKF Protolaser U3 laser cutter. By choosing a slow cut speed and thin width of texture (1 mm), rather than cutting the SS the heat caused by the laser created an oxide layer which deposited above the profile of the SS, as shown by Figure 7.7. Profiles were produced using a contact profilometer.

Laser Induced Breakdown Spectroscopy (LIBS)[126] was used with the assistance of Dr. Lord (University of Leeds. Department of Civil Engineering) to determine the material created by the texture methodology. As the name suggests, LIBS is a destructive, rapid chemical analysis technology which uses a short, focused laser pulses to create a micro-plasma on the surface of the sample and a corresponding reference sample.

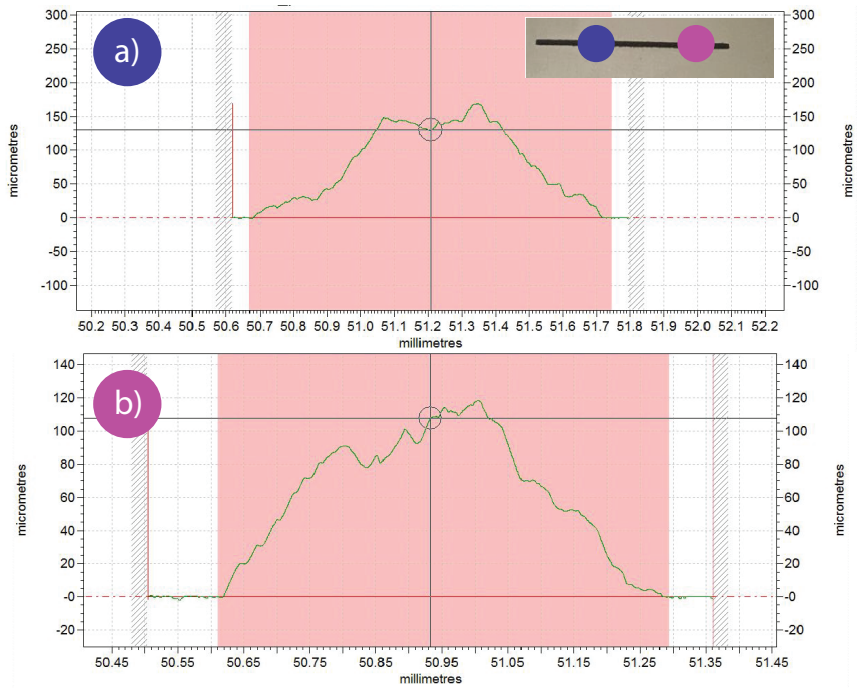

Figure 7.7: Profile of texture height and width at two test locations a and b; a and b are colour coded to the test locations shown in the insert

The interaction of the focused laser beam with the sample is a complex and not fully understood phenomenon[127]. When a pulse of high-power laser makes contact with the sample surface, irradiation at the focal spot leads to material removal; this process is known as ablation phenomenon[127]. The ablated material compressed the surrounding atmosphere and leads to the formation of a shockwave[127]. During this process, a wide variety of processes occur including; rapid local heating, melting, and intense evaporation. This evaporated material expands as a plume above the sample surface and, due to the high temperatures involved, a plasma is formed[127]. The plasma contains electrons, ions and neutral material as well as excited species of the ablated matter. The light emitted by these excited species are measured by the LIBS spectrometer. Further detail about the LIBS process and analysis can be found in the 'Handbook of Laser-Induced Breakdown Spectroscopy" by Creamers[126].

The raw reference data produced from the LIBS is shown in Figure 7.8a, the three colours represent the output of the three detectors on the LIBs device. The coloured

spectra shows the raw sample data and the black spectra the reference data from a clean, SS* sample. For each detector, the sample and reference data are normalised to a peak apparent in both of relatively similar intensity. The normalised intensities are then scaled by a factor x^3 to reduce noise[128], the results of this are shown in Figure 7.8b. Using the National Institute of Standards and Technology (NIST) database[128] it was found that wavelengths corresponding to the large peaks shown in Figure 7.8b indicate an increased presence of Fe(II) or Fe(III). It is therefore assumed that the process of texture manufacture by slow travelling laser cutter formed an iron oxide above the surface of the SS.

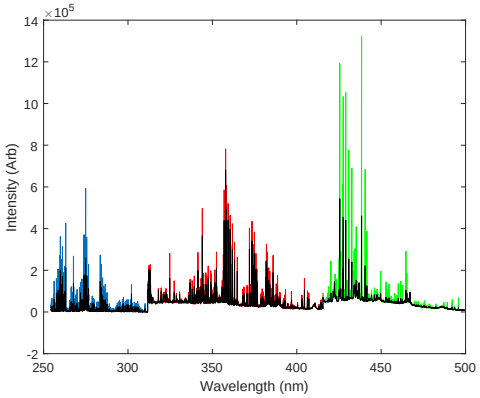

(a) Raw LIBS reference data (Coloured) and sample data (black).

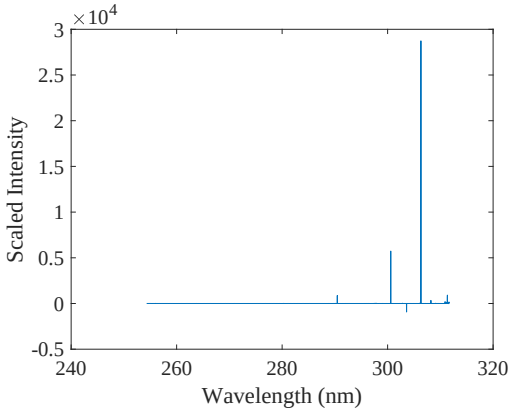

(b) Peak identification for use with the NIST database.

Figure 7.8: LIBS data analysis.

7.1.2.1 Design of textures

The final designs of the textured plates are shown in Figure 7.9. The overall textured area is 0.5 mm wider than the gasket creating the plate spacing and 60 mm long. A shorter length textured area was chosen due to size limitations of machinery. The final plate was manufactured in two parts, the textured area and the larger plate, the textured area was precision welded into position. Although the weld sits outside of the flow area was important that the weld was neat and flat, as it can be seen in Figure 7.9 the seam of the welding is precise and in the case of the cross hatch plate can barely be seen.

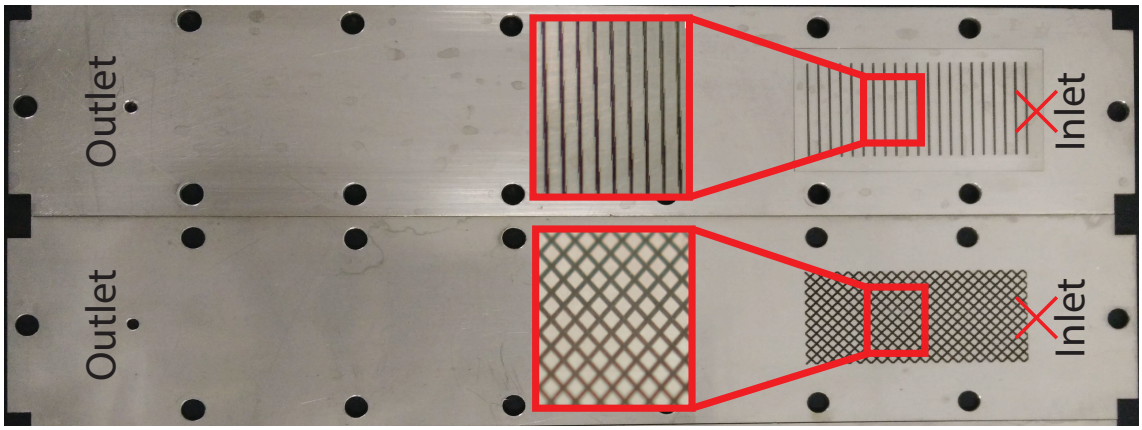

Figure 7.9: SS-S (top) and SS-C (Bottom) textured plates. Volume of texture for both textures is

7.1.3 Effect of plate textures on separation efficiencies

The non-linear relationship observed in Section 6 was achieved again within the textured P-TS and an S-curve was fitted to the separation efficiencies and extent of entrainment figures below. As such analysis will be a comparison between the values of L and k from Equation 6.2, which correspond to the total efficiency loss between the plate spacings tested and the rate at which efficiency is lost with increasing plate spacing.

The SS* plate data is desaturated behind the data for the SS-S and SS-C textures in Figures 7.10 and 7.11 for ease of reading, so the effect of introducing the texture can clearly be seen.

At first glance of Figures 7.10 and 7.11, it is apparent that only the SS-S texture at 1 mL/min and small plate spacing achieves a greater separation efficiency than the SS* plate. It is also apparent that the effect of increasing the flow rate has a larger impact on separation efficiency for higher plate spacings in the textured plate systems. It should be noted that the plate spacing at the texture is equal to those tested in for the SS* system, however, for the majority of the plate, the plate spacing has increased by 100 μm and the larger plate spacing will be used in all future calculations.

Looking at Figure 7.10 in greater detail there is a much higher loss in separation efficiency at larger plate spacings than the non-textured P-TS. A difference between 1

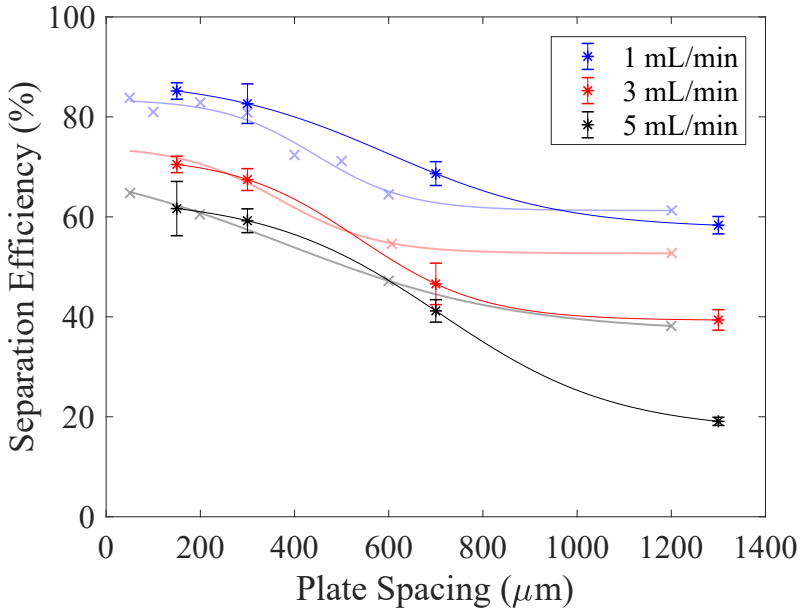

Figure 7.10: Plate efficiency for the SS-S plate texture. Desaturated below this data (shown as crosses) is the SS* separation efficiency data from Figure 6.3.

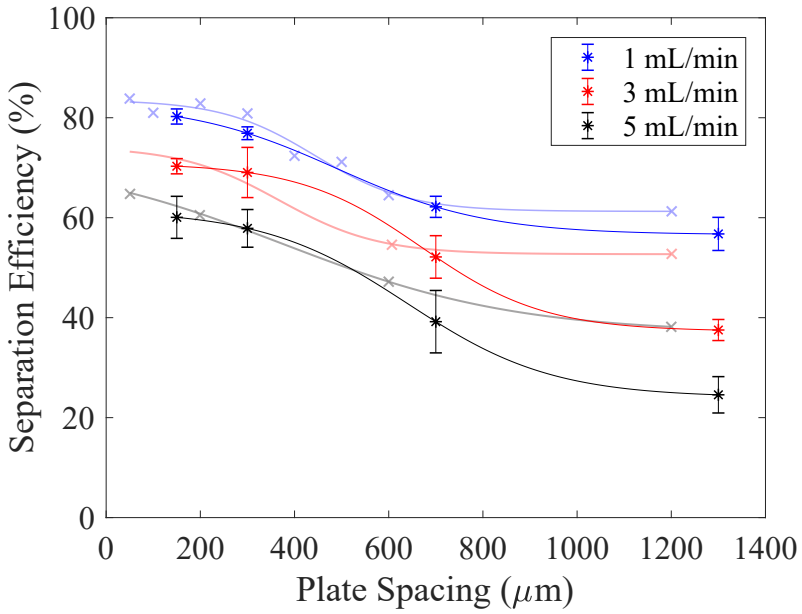

Figure 7.11: Plate efficiency for SS-C plate texture. Desaturated below this data (shown as crosses) is the SS* separation efficiency data from Figure 6.3.

and 5 mL/min of 23.5 % and 39.2 % occurs for plate spacings 150 μm and 1300 μm for the SS-S texture, respectively, as opposed to 20.2 % and 23.1 % for the SS* for the same plate

spacings, according the the fitted data. Showing that the reduction in separation efficiency with flow rate is greater and higher plate spacings when a texture is introduced. This is also apparent in the data from the curve fitting with the L value showing overall efficiency drops of 29.9 %, 31.0 % and 46.6 % for 1, 3 and 5 mL/min, SS-S texture configurations. These values are 4.3 %, 10.6 % and 15.8 % higher than those for the SS* configuration. The progressive increase is most likely due to increased droplet break-up over the textures at higher flow rates, or due to the 100 μm bulk increase in plate spacing for the textured system. Using the fitted data the to predict the efficiency at 150 μm the change in efficiency achieved by adding the SS-S texture is +4.7 %, −1.3 % and −0.7 % for 1, 3 and 5 mL/min, which are a stark contrast to the change in efficiency occurring at 1200 μm (−2.5 %, −13.4 % and −17.8 %). These values show that at low plate spacings the texture has negligible effects on separation efficiency. Whereas, as the plate spacing increases, the effect of the texture causes a large drop in separation efficiency which gets progressively higher with increasing flow rates.

The same relationship is observed between the SS-C texture and SS* configurations, with the change in efficiency achieved by adding the SS-C texture at 150 μm being 12.2 %, −1.5 % and −2.3 % for 1, 3 and 5 mL/min and −4.4 %, −14.9 % and −13.2 % at 1200 μm 1, 3, 5 mL/min respectively. Comparing the difference between the SS-S and SS* textures with that of the SS-C and SS* textures, it is apparent that at lower plate spacing the SS-S texture aids in separation more than the SS* and SS-C configurations. However, at higher plate spacings the SS-S texture deterioration in separation efficiency increases with flow rate. The opposite is observed for the SS-C texture relationship, which initially increases with flow rate then remains steady after 3 mL/min. This suggests that the SS-S texture creates greater droplet break-up at higher plate spacings than the SS-C.

Overall the result obtained with the introduction of the texture was not as expected. It was expected that increasing droplet mixing the promotion of coalescence would occur, however this was not observed in the overall results.

A basic, 3D, single-phase computational model was produced using a computational fluid dynamics software package, Fluent. The aim of modelling a single phase system was

to find areas of increased turbulence caused by the introduction of the texture. Ideally a multiphase model would have been completed, however, this was not feasible with computational resources available. However, the computational single phase data was related to the practical P-TS, two-phase flow conditions through the assumption of higher turbulence within the model would directly relate to droplet break-up and the premature detachment of settled droplets from the wall.

The model used was a $k-\epsilon$ model with enhanced wall treatment, where k is the turbulent kinetic energy and ϵ is the turbulent dissipation rate[129]. Ideally a low Reynolds $k-\epsilon$ would have been used, however, it is not available in software. To combat this, the values of k and ϵ were calculated prior to running the simulation, using data provided through the experimental work completed. The equations for the calculation of k and ϵ are shown below[129].

$$k = \frac{3}{2}(vI)^2 \tag{7.1}$$

where k is defined above, v is the superficial velocity and $I = 0.16(Re_{dh})^{\frac{-1}{8}}$ is the turbulent intensity at the inlet calculated using the hydraulic Reynolds number.

$$\epsilon = Cu^{\frac{3}{4}}\frac{k^{\frac{3}{2}}}{\ell} \tag{7.2}$$

where Cu is an empirical constant (0.09), k is calculated as above and the turbulent length scale is $ell = 0.07D_h$ where D_h is the hydraulic diameter.

A simple 2.7 cm wide, 2.5 cm long mesh of the straight texture channel was produced. Four straight mounts were included to represent the texture and the height, width and spacing between the textures was equal to that of the physical plates (100 μm height, 2 mm wide and 5mm apart).

The turbulent kinetic energy results are shown for plate spacing 200, 400, 600 and 1200 μm are shown in Figure 7.12. From this initial plot it can be seen that there is high levels of localised turbulence in all cases. The turbulent kinetic energy dissipates within quickly and is not carried down the plate.

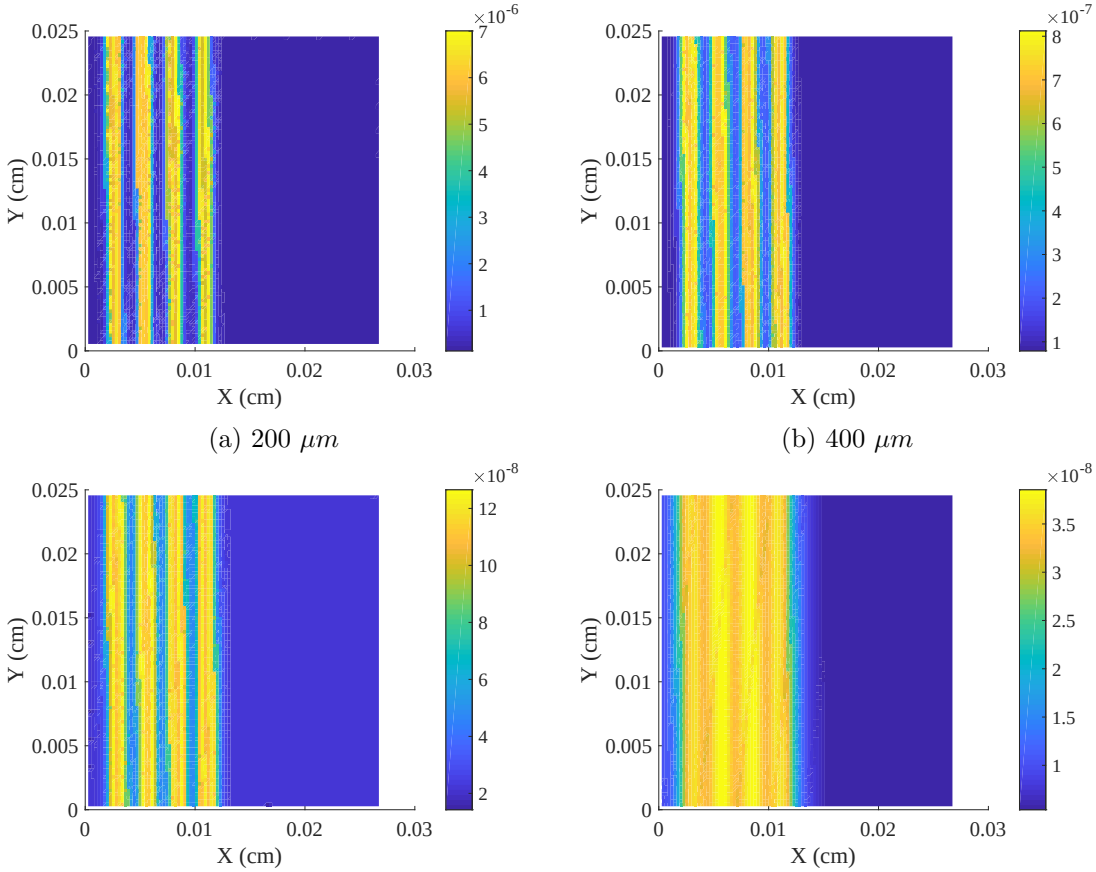

(a) 200 μm (b) 400 μm

(c) 600 μm (d) 1200 μm

Figure 7.12: Overhead view of the basic model showing the turbulent kinetic energy produced by the introduction of straight textures into the flow channel. The direction of flow is left to right.

When plotting the above graphs onto the same colour map range, it become apparent that although initially the turbulence looks higher in Figure 7.12d than it does in Figure 7.12a, it is in fact much lower, as shown in Figure 7.13.

Comparing Figure 7.13a - d, it can be seen that the magnitude of the localised turbulence reduces as plate confinement is reduced. Combining this data with that of the separation efficiency experimental results, it can therefore be concluded that, areas of localised turbulence to break-up flow structure formation in high confinement aids the overall separation efficiency of a P-TS.

When viewing the effect of textures on the turbulent kinetic energy looking through the plate spacing, Figure 7.14, it can be seen that at lower plate spacings the turbulence

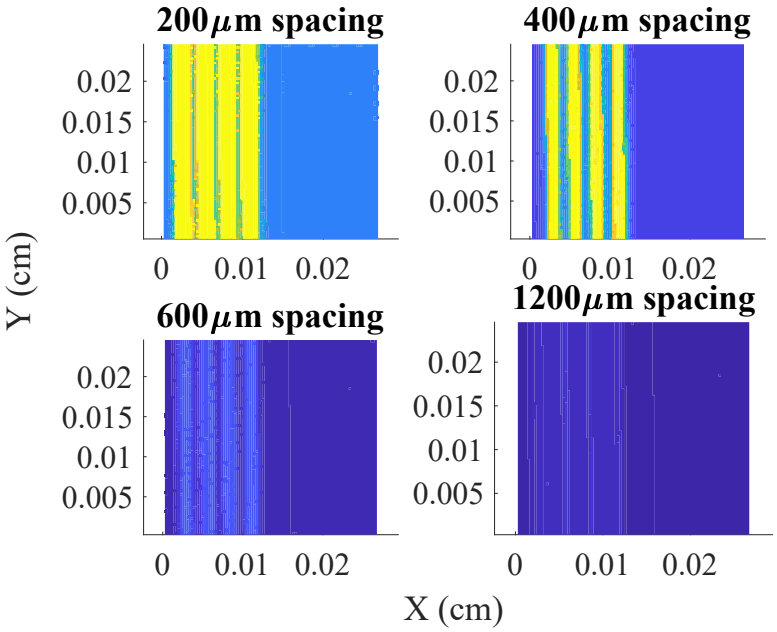

Figure 7.13: Overhead view of the basic model showing the turbulent kinetic energy produced by the introduction of straight textures into the flow channel, adjusted to same colour mapping scale for all plots. The direction of flow is left to right.

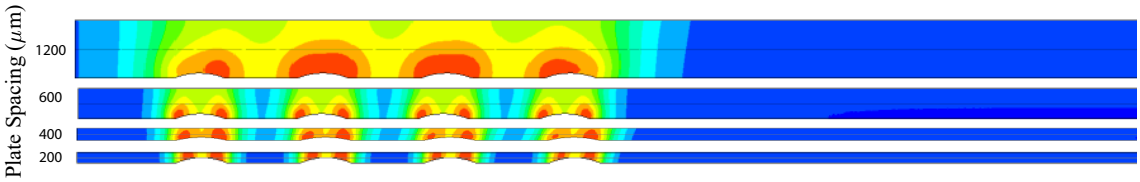

Figure 7.14: Side view of the basic model showing the turbulent kinetic energy produced by the introduction of straight textures into the flow channel. The direction of flow is left to right.

is at its highest across the entire height of the channel. As plate spacing is increased the increased turbulent dissipates towards the centre of the channel. Practically this means that there will be more circulation of droplets with low kinetic energy in the larger plate volume as opposed to high kinetic break-up at with a low plate spacing. However, this data would require plotting on the same colourmap to form a direct comparison. Overall it seen that the localised, turbulent kinetic energy is greater at low spacings. As there is an increase in separation efficiency under high confinement and high localised, turbulent kinetic energy conditions, it is believed that the introduction of textures over a greater

area would increase separation efficiency for less confined systems.

In addition to the data provided by the Fluent model above, the static outlet DSD of the SS-S and SS-C textures can be reviewed. Figure 7.15 shows the variation of droplet distribution with plate spacing and flow rate. Its can be seen that there is a significant difference in DSD with plate spacing when comparing Figures 7.15a and 6.9 (from Section 6). Figure 6.9 showed a steady increase of droplet frequency and $d_{[3,2]}$, whereas for the SS-S spacing there is an initial large increase of droplets when increasing the plate spacing from 150 μm to 300 μm, followed by a steady increase to at 700, with a plateau beyond. This plateau was not expected as the separation efficiency reduces over this period.

The DSD for varying flow rates at the plate spacing of 150 μm is shown in Figure 7.15b. An increase in droplet diameter was expected with an increase in flow rate and this relationship with observed. This change in DSD corresponds to the separation efficiencies achieved with the lowest separation efficiency and the highest number of droplets observed at 5 mL/min.

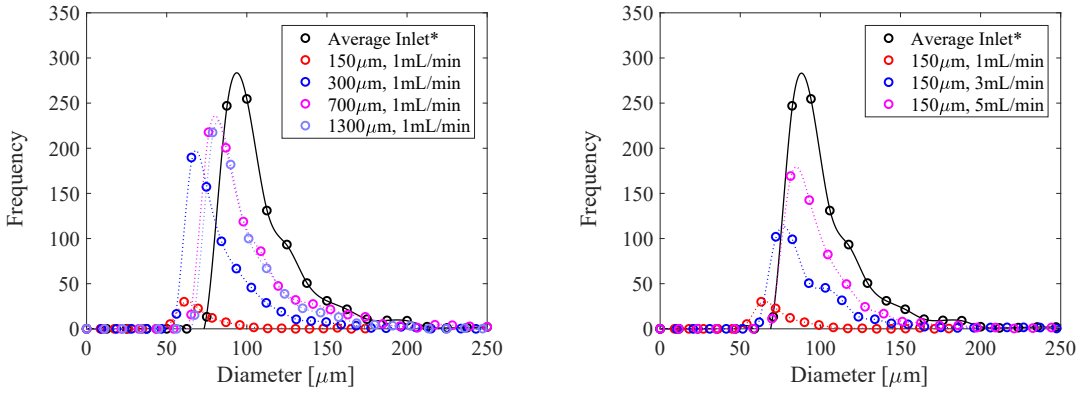

(a) Variation with plate spacing

(b) Variation with flow rate

Figure 7.15: DSD for varying plate spacing and flow rates for the SS-S texture.

A similar relationship is observed for the SS-C texture configuration, shown in Figure 7.16. Comparing Figure 7.16a with Figure 6.9, for the non-textured SS* plates, a similar relationship between plate spacing and DSD is observed. There is a steady increase of droplets observed with an increase in plate spacing, although a plateau at 700 μm was again observed. It is interesting to note that the frequency of droplets at a 700 μm plate

spacing is a larger than the average inlet*, suggesting that there is some break-up of larger droplets into smaller droplets at these higher plate spacings. The overall number of droplets shown in Figure 7.16 is much higher than in Figure 7.15, with the most prominent change being observed for the 150 μm plate spacing.

The DSD for varying flow rates at the plate spacing of 150 μm for a SS-C texture is shown in Figure 7.16b. As with Figure 7.15, the expected trend is observed with the largest number of droplets (at 5 mL/min) resulting the in lowest separation efficiency.

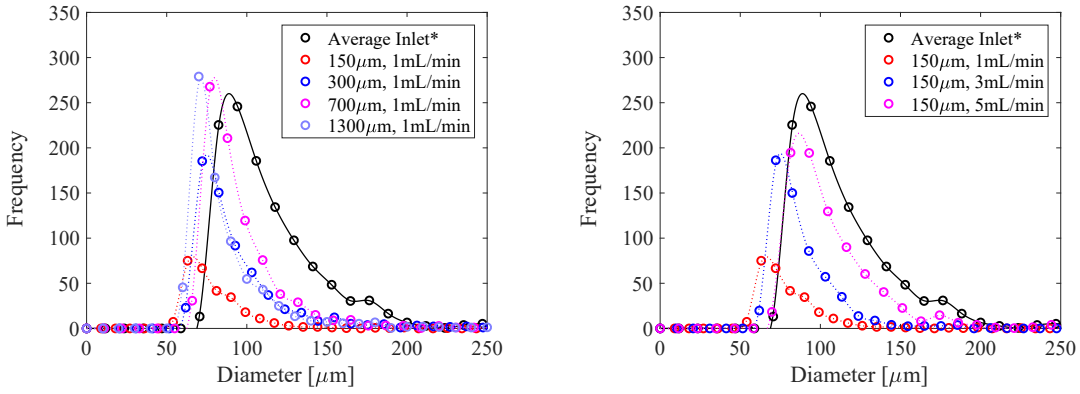

(a) Variation with plate spacing

(b) Variation with flow rate

Figure 7.16: DSD for varying plate spacing and flow rates for the SS-C texture

Overall the introduction of a small textured area did not provide the efficiency increase expected for the higher plate spacings, however, small but significant improvements were made for smaller plate spacings in some cases. It was expected that smaller droplets caught within a slug would be held up and slowed down by the texture, increasing the potential of a coalescence event. This was not observed as similar separation efficiencies are achieved for smaller plate spacing and a loss of separation efficiency observed at larger plate spacings. However, it is still believed that a textured area could achieve the desired effect. This is still believed due to the results shown in Figure 7.10. Using a SS-S texture a 4 % greater separation efficiency was achieved for a plate spacing 100 μm larger than the lowest used in the non-texture configuration. It is therefore believed that increasing the length of the texture towards the outlet will increase the separation achieved in confinement. The straight to outlet (SS-StO) texture shown in Figure 7.17 was designed to achieve this.

The texture was tapered to the aqueous outlet to allow for the development of laminar separation and the reduction added confinement within the textured areas.

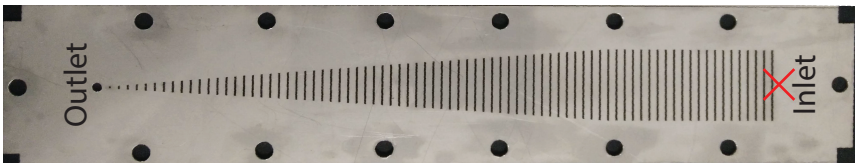

Figure 7.17: Straight texture extended toward the aqueous outlet to aid in separation within confinement.

The results achieved with a SS-StO textured plate are shown in Figure 7.18. Again the results of the SS* investigation are plotted and desaturated behind the data to aid in ease of comparison.

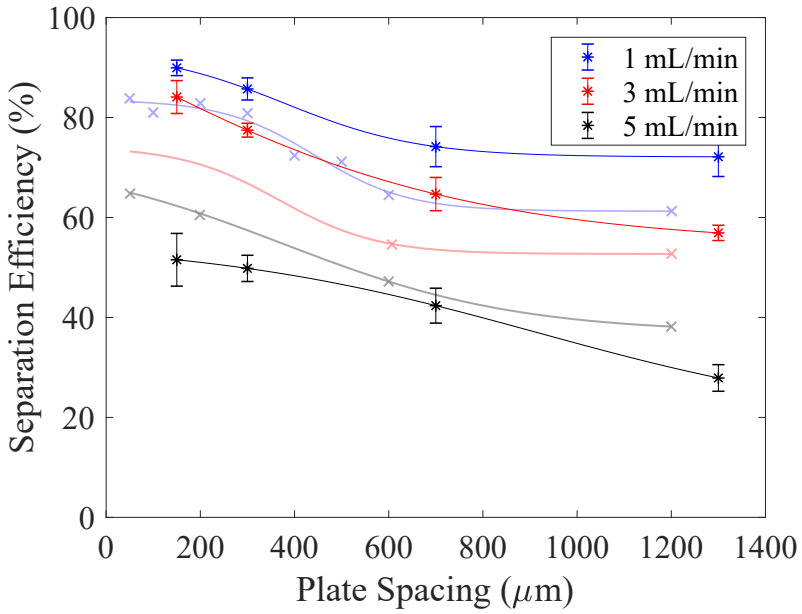

Figure 7.18: Straight texture extended toward the aqueous outlet to aid in separation within confinement. Desaturated below this data (shown as crosses) is the SS* separation efficiency data from Figure 6.3.

At a glance it can easily be seen that for low flow rates and low plate spacings there is an increase of separation efficiency achieved using the SS-StO texture. Comparing these results achieved with the addition of the SS-StO texture with those of the SS* configuration, an increase of 7.1 % is achieved at a plate spacing of 150 μm and 11.1 % at

1200 μm for a 1 mL/min flow rate. This trend in efficiency is also observed at 3 mL/min with increases of 13.3 % and 4.9 % for plate spacing of 150 μm and 1200 μm respectively. However, when the flow rate is increased to 5 mL/min there is an efficiency loss of 10.8 % and 11.8 %.

Comparing all four systems together in Figure 7.19, it is clear to see that the SS-StO is the most efficient P-TS for flow rates. At higher flow rates, the separation efficiency achieved overall is the worst of all the P-TS investigated. The largest deterioration in efficiency at the higher flow rate is observed for the smallest plate spacing, suggesting the elongation of the texture causes large droplet break-up under confinemen. In comparison, shorter textures can utilise the benefits of the non-textured area to recover from large droplet breakage.

7.1.4 Conclusion

In this chapter, flow structure formation was observed for low plate spacings. These structures were seen to break down with increased plate spacing. As it was found that separation efficiency reduces with plate spacing, it was concluded that an increased number of interfaces can aid in separation. The premise of this conclusion was that a droplet in a narrow flow structure has a reduced lateral distance to travel to meet its 'like' phase in contrast

As the highest separation efficiency was achieved for a plate spacing of 50 μm, where the greatest number of interfaces was observed within the inlet area of the P-TS, textured areas were introduced to this area to mimic the break down behaviour at higher plate spacings. However, the addition of textures within this area did not achieve the desired effect, with only slight improvements to separation efficiency being observed at low flow rates, and a loss of separation efficiency occurring at higher flow rates.

A simplified computational model was used to show limited turbulence created by the introduction of the textures, therefore concluding that the reduction in separation is likely from the increase in plate spacing required to account of the textured area.

An elongated texture, spanning the entire length of the plate was introduced (SS-StO)

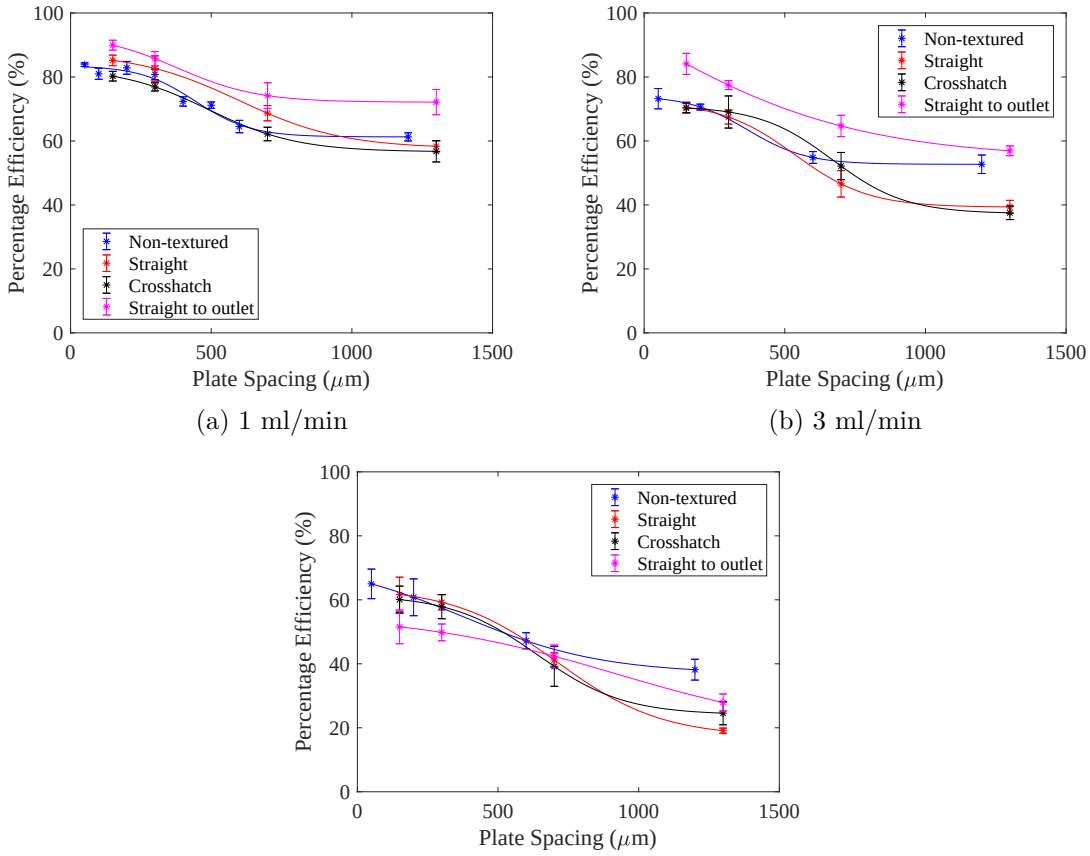

(a) 1 ml/min

(b) 3 ml/min

(c) 5 ml/min

Figure 7.19: Comparison of the separation efficiency acheived by all P-TS investigated for different 1, 3, and 5 mL/min

and an overall separation efficiency increase was achieved for 1 and 3 mL/min systems. A reduced separation efficiency was observed for higher flow rates, due to increased droplet break-up as the velocity of droplet impact with the texture is increased.

Overall the SS-StO P-TS provided the highest separation efficiencies in comparison to all configurations tested and therefore will be taken forward for further investigation in Section 7.2. The volumetric flow rate and plate spacing (including texture height) chosen for the following experiments are 3 ml/min and 200 μm as there is greater scope for efficiency improvement.

7.2 Hydro-Treated Plates

From the above experimental and computational design work, it has been concluded that smaller plate spacing provides greater confinement and larger separation efficiencies. It was also found that increasing the volumetric flow rate through the separator had the opposite effect. Through visual techniques, the change in DSD across the plate length was reviewed, as well as an overall view to capture the behaviour of larger flow structures. It was found that in confinement, pearl string structures of droplets are formed which elongate and expand as plate spacing is increased. The outcome of the previous studies concludes that the two most efficient plate configurations with SS* and SS-StO lower plates, at a flow rate of 1 mL/min.

Considering the relationship between plate spacing, volumetric flow rate and separation efficiency, it was decided that the final optimisation tests would be completed at 3 mL/min in a 100 μm plate configuration (200 μm for StO texture). This configuration was chosen as it has the most scope for improved separation extent within a desirable time frame, without the increased pressure drop associated with a lower plate spacing.

Although an optimised efficiency has been achieved, the P-TS in the current configuration is not suitable for industrial use due to the PMMA upper plate material. PMMA is proven to fracture under load and has low chemical resistance to common chemicals used within the majority of industrial processes. The ideal configuration of P-TS would

be stainless steel upper and lower plates (SS-SS) as SS is a strong industrial standard material with high chemical and corrosion resistance. However, previous studies have found that the loss of the hydrophobic/hydrophilic plate characteristics results in a large drop in separation efficiency, as discussed in Section 1.4[31,32,35].

To combat the loss of hydrodynamic wall effects caused by the replacement of the upper PMMA plate with a SS* plate, a hydrophobic coating was applied to the SS through treatment with a silane functional group. Silane functionality is a common method for increasing the hydrophobic properties of materials and is used in for applications such as corrosion inhabitation, adhesion promotion and contaminations control[130–133].

Silanes are the most important, diverse class of surface modification reagents, developed within the past century[134]. Many hundreds of silanes have been developed to tailor surface properties for a vast amount of applications. There are two main processes used in industrial and academic applications for the deposition of silane onto a surface, which are liquid or gas phase deposition. The liquid approach is simple, requiring only standard laboratory glassware, however, is incredibly temperature and humidity sensitive. The liquid deposition process is commonly more difficult to reproduce and also requires toxic, flammable organic solvents which can be avoided by using gas phase deposition[135–137]. The gas phase deposition, or chemical vapor deposition (CVD) requires vacuum equipment which can be costly, but is more reproducible and only requires the silane solution in very small volumes ($\leq 1\,\mathrm{mL}$) and no other chemicals. For these reasons a CVD method was used within this study.

7.2.1 Silane functionality

Silicon, being in the same family as carbon in the periodic table, has very similar physical and chemical properties as carbon, such as the ability to form four convalent bonds. However, due to differences in p-orbital configurations the chemical properties are not identical as Si can only naturally form single Si-Si bonds, unlike carbon. Although chemists have achieved the Si=Si form before[138–140].

Silane in its purist form is a silicon atom covalently bonded to four hydrogen atoms

forming SiH_4. SiH_4 is highly relative, pyrophoric, in air and requires specialist equipment to handle[139,140]. The term "silane", commonly reported on in literature, is actually a silane derivative known as a silane coupling agent (SCA) where one of the hydrogen atoms is replaced with another chemical moiety, as shown in Figure 7.20[139,140]. Silane derivatives are much safer to work[138–140].

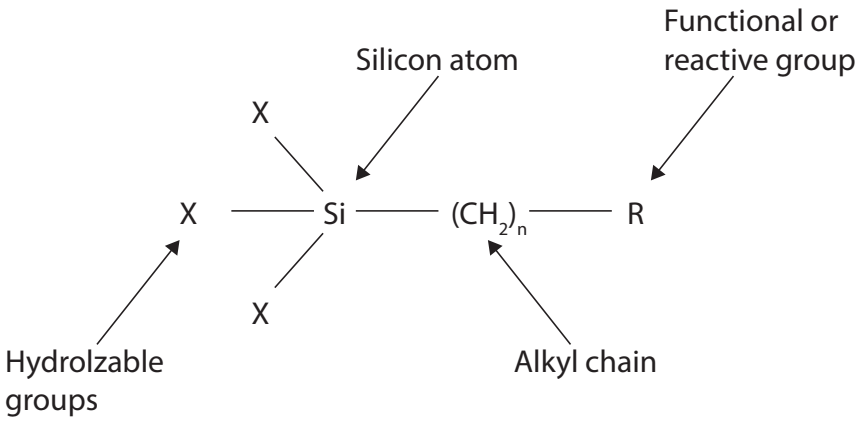

Figure 7.20: General structure of a SCA monomer.[139]

Silane reactive groups (X in Figure 7.20) often can not react with organic molecules but can convalently bond with certain inorganic molecules[139,140]. SCA can be used to couple organic and inorganic substrates as the organic arm (terminating in R, shown in Figure 7.20) can be designed to facilitate covalent linkage with organic molecules. The silane chosen for this application was 1H,1H,2H,2H-Perfluorooctyltriethoxysilane, shown in Figure 7.21[138–140].

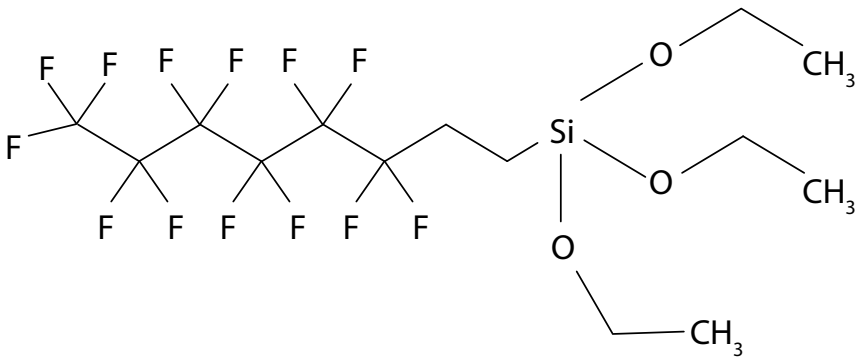

Figure 7.21: Structure of 1H,1H,2H,2H-Perfluorooctyltriethoxysilane.

The initial reaction occurring near the inorganic substrate is the condensation of SCAs, forming a -Si-O-Si- linked polymer matrix[138]. The polymer matrix then interacts with the inorganic substrate through the formation of a network of hydrogen bonds[138]. A further condensation reaction occurs resulting in the formation of stable oxane bonds. The oxane bonds, or siloxane linkage, consist of convalently linked organosilane polymers to the surface. These stages are shown in Figure 7.22[138].

Siloxane linkage produced using the method shown in Figure 7.22 do not form organised monolayers but a thick polymer layer with the reactive groups extending out from the surface known as a surface active matrix (SAM)[138,141]. The thickness of this layer depends on the concentration of SCA used and the amount of water present in the solution. It has been found through computational methods that increasing the density of -Si-O-Si- bonds increases the disorder within the reactive groups, this is shown in Figure 7.23, where 7.23a has fewer bonds and more order within the reactive group tails[141].

7.2.2 Methodology

7.2.2.1 Metal-Metal configuration methodology

The majority of the methodology for running the P-TS in a metal-metal configuration is the same as that in Section 6.1. However, as the top plate is no longer clear, images taken in camera positions 1 and 2 in Figure 5.12 could not be taken.

A SS* plate prior to surface coating was first tested with a SS* lower plate at 3 mL/min and 100 μm. This process was then repeated with the same top plate and the SS-StO lower plate and a spacing of 200 μm.

Chemical vapour deposition of the SS* plate was undertaken using the methodology described in Section 7.2.2.2 to created a treated SS plate (T-SS). Experiments at 3 mL/min and 100 μm/ 200 μm with a T-SS upper plate and SS*, SS-StO lower plates were then completed.

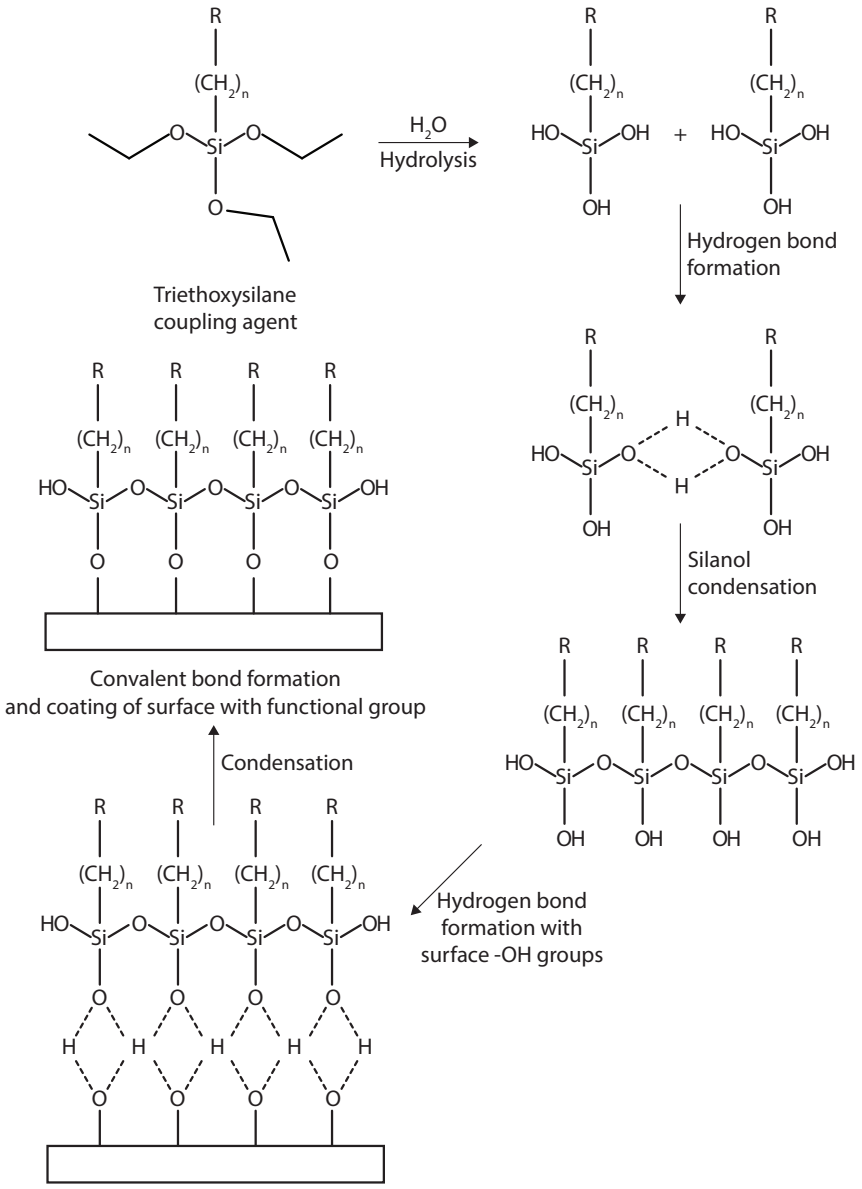

Figure 7.22: Formation of a organosilane coating on an inorganic substrate[138].

7.2.2.2 Chemical vapour deposition of SCA methodology

In all cases the reagents used were 99 % purity or higher from Fisher Scientific (Loughborough) and Sigma Aldrich (Dorset), with the exception of 1H,1H,2H,2H-Perfluorooctyltriethoxysilane that was 98 %. The All water used is ultrapure, deionized water from a MilliQ by Millipore water purification system (Millipore, Watford, UK).

The initial contact angle of a fully manufactured plate, to the specification provided

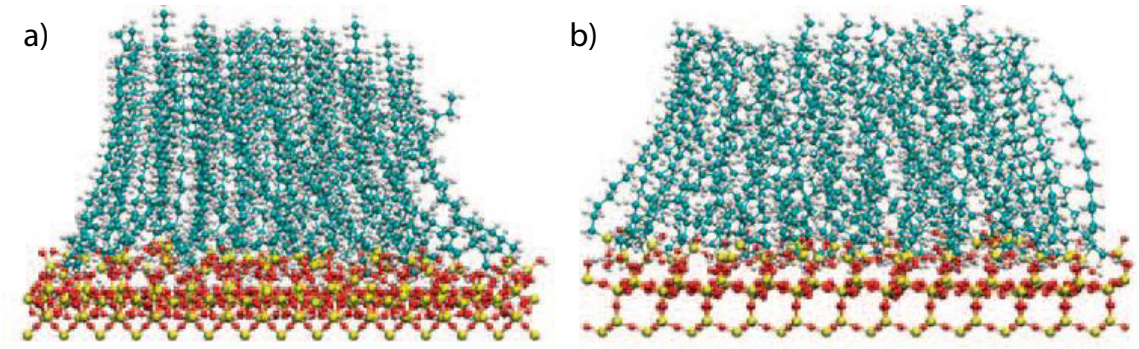

Figure 7.23: SAM produced with the -Si-O-Si- bond density of a) 26 and b) 52.[141]

in Figure 5.1(b), was taken following the methodology covered in Section 3.1.1. The plate was then cleaned thoroughly in two stages. The first stage was to fully submerge the plate in a 3 M HNO_3 bath heated to 75 ^oC for 30 minutes. After cleaning with the acidic solution the plate was thoroughly rinsed with water and acetone to remove any surface contaminants. In the second cleaning stage the plate was fully submerged in a 3 M sodium hydroxide (NaOH) solution, again heated to 75 ^oC and for 30 minutes. After a final rinse with water and acetone the SS plate was ready for treatment with the silane.

In a fume cupboard, a small beaker was filled with 1 mL of 1H,1H,2H,2H Perfluorooctyl-triethoxysilane. The beaker and cleaned plate were placed in a desiccator and a vacuum pulled using a portable diaphragm vacuum pump. When the air within the desiccator was fully evacuated the vacuum line was sealed and the pump turned off. As no heat was used in this methodology the plate and silane were left under vacuum for 48 hours, however, with the addition of heating this time can be reduced.

The coating of the plate formed through the evaporation of the silane under vacuum followed condensation of the silane vapour onto the material surface. The contact angle of the treated SS (T-SS) was taken to confirm the coating was successful. Before and after pictures with the corresponding contact angles are shown in Figure 7.24.

7.2.3 Discussion of final design results

Data shown in Figure 7.25, shows the comparison between three P-TS configurations with varying upper plate materials. Literature has previously shown running the P -

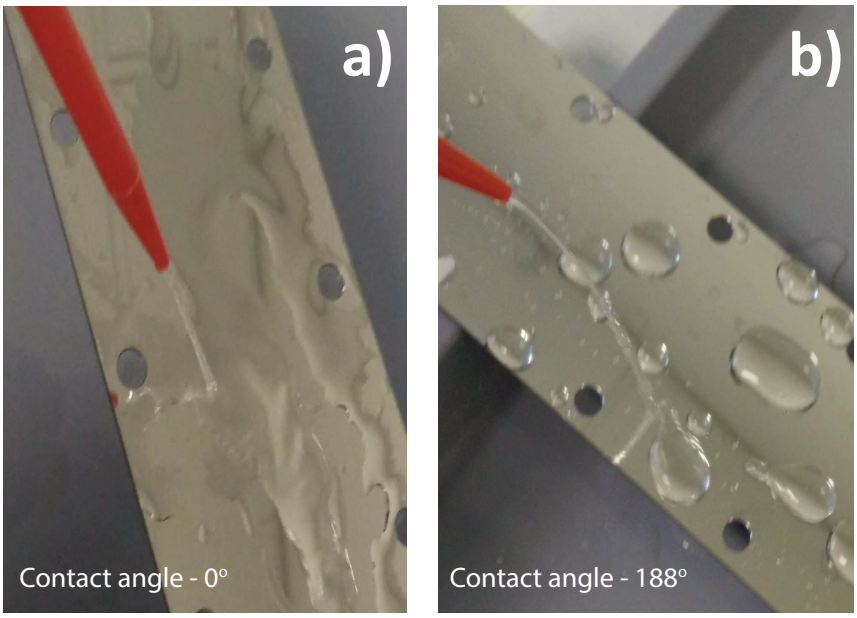

Figure 7.24: Effect of applying a SAM on stainless steel surface. Where a) shows water wetting the surface and b) shows water beading and rolling off the T-SS.

TS in a hydrophobic-hydrophobic plate configuration results in a large decrease in efficiency[31–33,35]. In this work, it is shown that the same occurs in hydrophilic-hydrophilic plate configuration, as shown by green bars in Figure 7.25. However, the efficiency drop shown is not as substantial as those observed in the hydrophobic-hydrophobic plate configuration. It is believed that this is due to the effect of the organic phase on the hydrophilic nature of SS, as discussed in Chapter 3.

The effect of applying a hydrophobic coating onto the upper plate material is shown in blue in Figure 7.25. Comparing these results with those from Chapter 6, shown in purple, it can be seen that the separation efficiency increased by 13 % and 18 % when introducing the silane coated non-textured lower plate to the system and the T-SS, respectively.

The increased plate spacing was achieved through design optimisation which considered all parts within this thesis. From literature and the contact angle experiments in Chapter 3, it was known that a large difference in the hydrodynamics of the plate material was required to achieve large separation factors[31,32,35]. Within this final experiment, a superhydrophobic coating was applied to ensure this difference was maximised. In Chapter 6, it was found that a confined plate spacing can increase droplet coalescence by reducing the

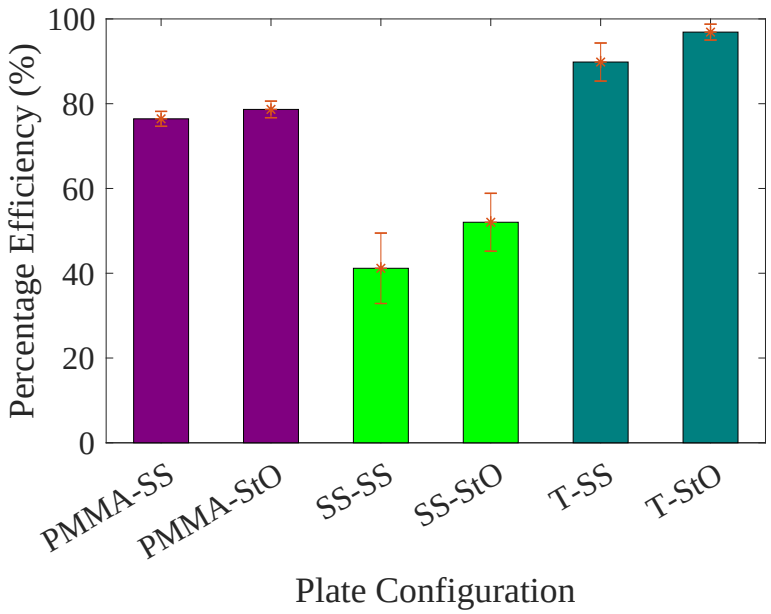

Figure 7.25: Comparison of efficiencies achieved across all tested plate configuration.

angle at which droplets met and forcing smaller, fast flowing droplets into the coalescence zone shown in Figure 4.1. The principle of confinement is utilised within the final P-TS design. Finally in Chapter 7.1, it was found that increasing the number of interactions across the width of the plate, increased separation efficiency is achieved, and therefore textures were introduced to the lower plate to promote the break-up of flow structures formed through localised turbulence through the spacing between the textured and upper plated. The combination of these three experimental chapters resulted in the highest efficiency of separation being achieved in a 200 μm plate spacing, with a 100 μm StO texture lower plate and a T-SS upper plate at 3 mL/min; the efficiency achieved with this configuration was 96.9 %.

CHAPTER 8

Conclusion & future work

8.1 Contact Angle

The hydrophilic behaviour of SS is reduced in the presence of an organic continuous phase or organic contamination. In terms of separator design, previous studies have suggested that the cause of separation in the P-TS is a result of the different fluid interactions with the hydrophobic and hydrophilic walls[31–33,35]. Using the results found within this study, if the previous statement is correct, it would be found that the separation efficiency of a P-TS is reduced when the continuous phase of a dispersion is organic phase. This theory was used in Section 7.2 to aid in the design of the final, optimised P-TS.

Further to this, it was observed that increasing the pH within the dispersed phase, reduces the contact angle on both hydrophilic and hydrophobic environments, however the opposite was found when increasing the pH within the continuous phase. The effect of increasing [HMI] within the dispersed phase was minimal for both hydrophilic and hydrophobic test materials. However, as with the pH, increasing [HMI] in the continuous phase causes an increase in contact angle. It was also found that an increase in the volume of TBP within the organic phase will increase the contact angle in all cases.

The effect of these relationships within the P-TS were unable to be investigated due to low dispersion longevity of the systems tested within this study, as shown in Section 5.2. Further work would have to be completed within a radiation environment or using TBP radiation degradation products, to increase the system viscosity to directly compare the effect of increased/decreased contact angle with [HMI] variations experienced within the PUREX flowsheet on P-TS separation efficiencies.

8.2 Interfacial Tension and Coalescence Rate

In all cases an increase in [HMI] resulted in an increase in interfacial tension and a higher coalescence rate. The introduction of TBP increased coalescence rate by 12 %, which is supported by the drop in interfacial tension and droplet volume observed in the presence of TBP. This interfacial tension change was found to be controlled by the [HMI] for systems with a pH greater than 1.5. Below a pH of 1.5, the interfacial tension is likely governed by the relationship at the droplet interface between the ligand, TBP, and $[H^+]$. This relationship between interfacial tension and coalescence rate was expected due to the well documented theory of cohesive forces of molecules at the droplet interface[41].

In practice this conclusion means that in an industrial flowsheet, the efficiencies of the separation stages will vary within a bank as the HMI varies and so, the system [HMI] and diluent concentrations must be taken into consideration to improve separation efficiency and reduce over-engineering.

Again, unfortunately, the effect of these relationships within the P-TS were unable to be investigated due to low dispersion longevity of the systems tested within this study, as shown in Section 5.2. To investigate the effects of P-TS separation efficiencies with interfacial tension and [HMI] variations experienced within a PUREX flowsheet, further work is required within a radiation environment.

8.3 P-TS Design Optimisation

Within this investigation it was confirmed that the P-TS is a highly efficient method for the separation of fine droplet immiscible dispersions.

The efficiency of separation is greater in highly confined situations (lower plate spacings) and lower flow rates. As plate spacing is expanded, a non-linear reduction in separation efficiency is observed for all flow rates. The point at separation efficiency deterioration increases with plate spacing occurs at higher plate spacings for reduced flow rates. Therefore, low flow rate systems maintain the ideal, confined separation conditions at higher

plate spacings than higher flow rates.

As expected entrainment of droplets within the biphasic outlet increased with plate spacing and reduced with separation efficiency, as supported by a decrease in droplet frequency in outlet DSDs. The diameter of entrained droplets within the biphasic outlet reduces with plate spacing, however, when compared to the inlet DSD the total diameter change from inlet to outlet is low.

It can be concluded that the separation times and separation efficiencies achieved are significant improvements to gravity separation of the same dispersion. With the fastest P-TS separation time, 4.4 s achieved with SS*, 50 μm spacing and 5 mL/min, providing a 409$\times$ improvement compared to gravity separation. The shortest P-TS separation time, $\approx$ 550 s achieved with SS*, 1200 μm spacing and 1 mL/min,also provided a 98.9 % improvement compared to gravity separation. The increased separation efficiency is the direct result of confined, wall effects within the P-TS.

Flow structure formation was observed for low plate spacings. These structures were seen to break down with increased plate spacing. As it was found that separation efficiency reduces with plate spacing and concluded that an increased number of interfaces can aid in separation. The premise of this conclusion was that a droplet in a narrow flow structure has a reduced lateral distance to travel to meet its 'like' phase, in comparison to a droplet caught in the center of a large slug.

As the highest separation efficiency was achieved for a plate spacing of 50 μm, when then greatest number of interfaces was observed within the inlet area of the P-TS, textured areas were introduced to this area to mimic the break down behaviour at higher plate spacings. However, the addition of textured within this area did not achieve the desired effect. With only slight improvements to separation efficiency being observed at low flow rates, and a loss of separation efficiency occurring for at higher flow rates.

A simplified computational model was used to show limited turbulence created by the introduction of the textures, therefore concluding that the reduction in separation is likely from the increase in plate spacing required to account of the textured area.

An elongated texture, spanning the entire length of the plate was introduced (SS-StO)

and an overall separation efficiency increase was achieved for 1 and 3 mL/min systems. A reduced separation efficiency was observed for higher flow rates, due to increased droplet break-up as the velocity of droplet impact with the texture is increased.

Overall the SS-StO P-TS provided the highest separation efficiencies in comparison to all configurations tested and was taken forward for further investigation. The volumetric flow rate and plate spacing (including texture height) chosen for further investigation were 3 ml/min and 200 μm as they had the greatest scope for efficiency improvement.

The effect of applying a hydrophobic coating onto the upper plate material was found. The results of this experiment were compared to those from the non-textured P-TS from Section 6. It was found that the separation efficiency increased by 17 % and 23 % when introducing the silane coated non-textured lower plate to the system and the T-SS, respectively.

The final increase in separation efficiency was achieved through design optimisation which considered all parts within this thesis.

- From literature and the contact angle experimental in Chapter 3, it was shown that a large difference in the hydrodynamics of the plate materials was required to achieve large separation factors[31,32,35].

- In Chapter 6, it was found that a confined plate spacing can increase droplet coalescence by reducing the angle at which droplets met and forcing smaller, fast flowing droplets into the coalescence zone shown in Figure 4.1.

- in Chapter 7.1, it was found that increasing the number of interactions across the width of the plate, increased separation efficiency and therefore textures where introduced to the lower plate to break-up flow structures formed through localised turbulence through the spacing between the texture and upper plate.

The final optimised design uses a super-hydrophobic coating to ensure the maximum difference in hydrodynamics between the plate materials was maximised. The principle of confinement was utilised through choosing a low, confined plate spacing, and finally

a texture was applied to the lower plate to introduce localised turbulence through the spacing between the texture and upper plate.

The combination of these three experimental chapters resulted in the highest efficiency of separation being achieved in a 200 μm plate spacing, with a 100 μm StO texture lower plate and a T-SS upper plate at 3 mL/min; the efficiency achieved with this configuration was 96.9 %.

8.4 Future Work

Although this thesis has thoroughly investigated the design of a P-TS, there are many factors that could be investigated computationally and compared to the results within this thesis to further strengthen the theory as to why such high separation factors were achieved. The computational work completed within this thesis was limited and only used to show the general increase in flow velocity and turbulence. To fully asses the hydrodynamics within the P-TS a full, in depth CFD assessment is required using advanced CFD techniques. This is required to fully capture the turbulent phenomena arising from confinement and wall effects within the P-TS. This would include the use of a low Reynolds number, turbulence model or Large Eddy Simulation (LES) to correctly approximate a solution to the navier-stokes equations. Additionally, the use of a multiphase model such as Volume of fluid or eulerian-eulerian methods should be used to capture and asses the complexities of the coalescencing dispersed phase.

Now it is known that the P-TS can achieve high separation rates with industry appropriate materials, the next stage in the design process will be to focus on scale up of the volumetric throughput. It has been shown in this work that scale up by increasing the plate spacing is not feasible therefore, scale-up by number up will have to be used. Computational methods can be used to quickly predict the separation efficiency of multiple units to achieve a desired throughput. This separation efficiency can be optimised by varying the plate spacing and geometry of the individual units. Once scale up is completed, a cost and efficiency comparison between the P-TS and a bank of centrifugal contactors could

be completed.

Further work is required to ensure the longevity and chemical/radiation compatibility of the super-hydrophobic coating. The feasibility and cost of coating removal for decommissioning purposes could also be investigated.

Bibliography

[1] P. Hewitt, *Managing the Nuclear Legacy.* No. july, UK Government White Paper, 2002.

[2] UK Government, *The Road to 2010 Addressing the nuclear question in the twenty first century.* 2009.

[3] WNA (World Nuclear Association), "Nuclear Power in the United Kingdom, UK Nuclear Energy.," 2017.

[4] T. Abram, "PACIFIC - Providing a Nuclear Fuel Cycle in the UK for Implementing Carbon Reductions," 2015.

[5] K. L. Nash and G. J. Lumetta, *Advanced separation techniques for nuclear fuel reprocessing and radioactive waste treatment.* Woodhead Publishing, 2011.

[6] D. Warin, "Developments in the partitioning and transmutation of radioactive waste," in *Advanced Separation Techniques for Nuclear Fuel Reprocessing and Radioactive Waste Treatment*, pp. 363–376, 2011.

[7] NDA (Nuclear Decommission Authority), "End in sight for reprocessing nuclear fuel at Sellafield | Dealing with the past, protecting the future," 2017.

[8] M. C. Regalbuto, "Alternative separation and extraction: UREX+ processes for actinide and targeted fission product recovery," in *Advanced Separation Techniques for Nuclear Fuel Reprocessing and Radioactive Waste Treatment*, pp. 176–200, 2011.

[9] I. Hore-Lacy, *Can americium replace plutonium in space missions?* World Nuclear News, 2014.

[10] R. Taylor, *Reprocessing and recycling of spent nuclear fuel.* Woodhead Publishing, 2015.

[11] M. Iqbal, *Synthesis and evaluation of potential ligands for nuclear waste processing.* PhD thesis, University of Twente, Enschede, The Netherlands, oct 2012.

[12] K. Loening, "Recommended Format for the Periodic Table of the Elements.," *Journal of Chemical Education*, vol. 61, no. 2, 1984.

[13] K. L. Nash and M. Nilsson, "Introduction to the reprocessing and recycling of spent nuclear fuels," in *Reprocessing and Recycling of Spent Nuclear Fuel*, pp. 3–25, 2015.

[14] M. Benedict, T. H. Pigford, and H. W. Levi, *Nuclear chemical engineering*. McGraw-Hill, 1981.

[15] P. Souček and R. Malmbeck, "Pyrochemical processes for recovery of actinides from spent nuclear fuels," in *Reprocessing and Recycling of Spent Nuclear Fuel*, pp. 437–456, 2015.

[16] J. Rydberg, M. Cox, C. Musikas, and G. R. Choppin, *Solvent Extraction Principles and Practice, Revised and Expanded*. 2004.

[17] J. Coulson and J. Richardson, *Chemical Engineering, Volume 2: Particle Technology and Separation Processes*. Wiley-Blackwell, 4th ed., 2008.

[18] G. R. Choppin, "Solvent Exraction Principles and Practice," *Solvent Extraction Principles and Practice*, vol. Second Edt, pp. 81–108, 2004.

[19] C. Poinssot, B. Boullis, and S. Bourg, "Role of recycling in advanced nuclear fuel cycles," in *Reprocessing and Recycling of Spent Nuclear Fuel*, pp. 27–48, 2015.

[20] S. Bourg, C. Poinssot, A. Geist, L. Cassayre, C. Rhodes, and C. Ekberg, "Advanced Reprocessing Developments in Europe Status on European Projects ACSEPT and ACTINET-I3," *Procedia Chemistry*, vol. 7, pp. 166–171, 2012.

[21] C. A. Sharrad and D. M. Whittaker, "The use of organic extractants in solvent extraction processes in the partitioning of spent nuclear fuels," in *Reprocessing and Recycling of Spent Nuclear Fuel*, pp. 153–189, 2015.

[22] T. C. Frank, L. Dahuron, B. S. Holden, W. D. Prince, A. F. Seibery, and L. C. Wil-

son, “Liquid-Liquid extraction and other liquid-liquid operations and equipment,” in *Perrys' chemical engineers' handbook*, pp. 15–41, 2007.

[23] M. H. I. Baird and C. Hanson, *Handbook of solvent extraction*. Krieger Pub. Co, 1991.

[24] C. Hanson, *Recent advances in liquid-liquid extraction*. Pergamon Press, 1 ed., 1971.

[25] E. Y. Kenig, Y. Su, A. Lautenschleger, P. Chasanis, and M. Grünewald, “Micro-separation of fluid systems: A state-of-the-art review,” *Separation and Purification Technology*, vol. 120, pp. 245–264, dec 2013.

[26] D. Green and R. Perry, *Perry's Chemical Engineers' Handbook*. 2007.

[27] L. E. Burkhart and R. Fahien, *Pulse Column Design*. US Atomic Energy Commission, 1958.

[28] C. A. Sleicher, “Entrainment and extraction efficiency of mixer-settlers,” *AIChE Journal*, vol. 6, sep 1960.

[29] R. Cusack, “Rethink your liquid-liquid separations,” *Hydrocarbon Processing*, vol. 88, no. 6, pp. 53 – 60, 2009.

[30] A. Burkholz, *Droplet Separation*. VCH Publishing, 1989.

[31] E. Kolehmainen and I. Turunen, “Micro-Scale Liquid-Liquid Separation in a Plate-Type Coalescer,” in *Micro-Scale Liquid-Liquid Separation in a Plate-Type Coalescer Proceedings of European Congress of Chemical Engineering*, 2007.

[32] Y. Okubo, M. Toma, H. Ueda, T. Maki, and K. Mae, “Microchannel devices for the coalescence of dispersed droplets produced for use in rapid extraction processes,” *Chemical Engineering Journal*, vol. 101, pp. 39–48, aug 2004.

[33] X. Chen, H. Lu, W. Jiang, L.-Y. Chu, and B. Liang, “De-emulsification of Kerosene/Water Emulsions with Plate-Type Microchannels,” *Industrial & Engineering Chemistry Research*, vol. 49, pp. 9279–9288, oct 2010.

[34] J. Fukushima, H. Tatsuta, N. Ishii, J. Chen, T. Nishiumi, and K. Aoki, "Possibility of coalescence of water droplets in W/O emulsions by means of surface processes," *Colloids and Surfaces A: Physicochemical and Engineering Aspects*, vol. 333, pp. 53–58, feb 2009.

[35] T. Roques-Carmes, H. Monnier, J.-F. Portha, P. Marchal, and L. Falk, "Influence of the plate-type continuous micro-separator dimensions on the efficiency of demulsification of oil-in-water emulsion," *Chemical Engineering Research and Design*, vol. 92, pp. 2758–2769, nov 2014.

[36] D. E. Leng and R. V. Calabrese, "Immiscible Liquid – Liquid Systems," *Handbook of Industrial Mixing: Science and Practice*, pp. 639–753, 2004.

[37] K. Ward and Z. H. Fan, "Related content Mixing in microfluidic devices and enhancement methods," *Journal of mircomechanic and microengineering*, vol. 25, 2015.

[38] S. R. Kosvintsev, G. Gasparini, R. G. Holdich, I. W. Cumming, and M. T. Stillwell, "Liquid-Liquid Membrane Dispersion in a Stirred Cell with and without Controlled Shear," *Industrial & Engineering Chemistry Research*, vol. 44, 2005.

[39] D. Tsaoulidis and P. Angeli, "Liquid-liquid dispersions in intensified impinging-jets cells," *Chemical Engineering Science*, vol. 171, pp. 149–159, nov 2017.

[40] R. Murakami, H. Moriyama, T. Noguchi, M. Yamamoto, and B. P. Binks, "Effects of the Density Difference between Water and Oil on Stabilization of Powdered Oil-in-Water Emulsions," *Langmuir*, vol. 30, pp. 496–500, jan 2014.

[41] J. Berthier and J. Berthier, "Theory of Wetting," in *Micro-Drops and Digital Microfluidics*, ch. 2, pp. 7–73, Elsevier, 2013.

[42] J. D. Berry, M. J. Neeson, R. R. Dagastine, D. Y. Chan, and R. F. Tabor, "Measurement of surface and interfacial tension using pendant drop tensiometry," *Journal of Colloid and Interface Science*, vol. 454, pp. 226–237, sep 2015.

[43] J. Drelich, C. Fang, and C. L. White, "Measurement of interfacial tension in Fluid-Fluid Systems," 2014.

[44] P. L. du Noüy, "A new apparatus for measuring surface tension," *The Journal of general physiology*, vol. 1, pp. 521–4, may 1919.

[45] W. D. Harkins and H. F. Jordan, "A method for the determination of surface and interfacial tension from the maximum pull on a ring," *Journal of the American Chemical Society*, vol. 52, pp. 1751–1772, may 1930.

[46] R. D. Vold and M. J. Vold, *Colloid and interface chemistry.* Addison-Wesley, 1983.

[47] A. I. Rusanov and V. A. V. A. Prokhorov, *Interfacial tensiometry.* Elsevier, 1996.

[48] L. Rayleigh, "On the Theory of the Capillary Tube," *Proceedings of the Royal Society A: Mathematical, Physical and Engineering Sciences*, vol. 92, pp. 184–195, jan 1916.

[49] P. Rehbinder, "Dependence of surface activity and surface tension of solutions upon temperature and concentration," *Z. Phys. Chem.*, no. 111, pp. 447–464, 1924.

[50] A. M. Worthington, "On Pendent Drops," *Proceedings of the Royal Society of London*, vol. 32, pp. 362–377, jan 1881.

[51] A. M. Worthington, "Note on a point in the theory of pendant drops," *Philos. Mag.*, no. 19, pp. 46–48, 1885.

[52] F. Bashford and J. Adams, *An attempt to test the theories of capillary action: by comparing the theoretical and measured forms of drops of fluid.* University Press, 1883.

[53] A. C. Merrington and E. G. Richardson, "The break-up of liquid jets," *Proceedings of the Physical Society*, vol. 59, pp. 1–13, jan 1947.

[54] T. Z. Harmathy, "Velocity of Large Drops and Bubbles in Media of Infinite or Restricted Extent," *AIChE Journal*, vol. 6, 1960.

[55] J. M. Andreas, E. A. Hauser, and W. B. Tucker, "Boundard tension by pendant drops," *The Journal of Physical Chemistry*, vol. 42, pp. 1001–1019, jan 1937.

[56] C. E. Stauffer, "The Measurement of Surface Tension by the Pendant Drop Technique," *The Journal of Physical Chemistry*, vol. 69, pp. 1933–1938, jun 1965.

[57] M. D. Misak, "Equations for determining 1/H versus S values in computer calculations of interfacial tension by the pendent drop method," *Journal of Colloid and Interface Science*, vol. 27, pp. 141–142, may 1968.

[58] C. Huh and R. Reed, "A method for estimating interfacial tensions and contact angles from sessile and pendant drop shapes," *Journal of Colloid and Interface Science*, vol. 91, pp. 472–484, feb 1983.

[59] Y. Rotenberg, L. Boruvka, and A. Neumann, "Determination of surface tension and contact angle from the shapes of axisymmetric fluid interfaces," *Journal of Colloid and Interface Science*, vol. 93, pp. 169–183, may 1983.

[60] N. M. Dingle, K. Tjiptowidjojo, O. A. Basaran, and M. T. Harris, "A finite element based algorithm for determining interfacial tension (γ) from pendant drop profiles," *Journal of Colloid and Interface Science*, vol. 286, pp. 647–660, jun 2005.

[61] N. J. Alvarez, L. M. Walker, and S. L. Anna, "A non-gradient based algorithm for the determination of surface tension from a pendant drop: Application to low Bond number drop shapes," *Journal of Colloid and Interface Science*, vol. 333, pp. 557–562, may 2009.

[62] M. Hoorfar and A. W. Neumann, "Recent progress in Axisymmetric Drop Shape Analysis (ADSA)," *Advances in Colloid and Interface Science*, vol. 121, pp. 25–49, sep 2006.

[63] E. A. Guggenheim, "The Principle of Corresponding States," *J. Chem. Phys. J. Chem. Phys. Journal Homepage*, vol. 13, no. 7, 1945.

[64] B. E. Rapp, "Surface Tension," in *Microfluidics: Modelling, Mechanics and Mathematics*, pp. 421–444, 2017.

[65] D. Packham, "Work of adhesion: contact angles and contact mechanics," *International Journal of Adhesion and Adhesives*, vol. 16, pp. 121–128, may 1996.

[66] M. Härth and D. W. Schubert, "Simple Approach for Spreading Dynamics of Polymeric Fluids," *Macromolecular Chemistry and Physics*, vol. 213, pp. 654–665, mar 2012.

[67] R. Tadmor, "Line Energy and the Relation between Advancing, Receding, and Young Contact Angles," *Langmuir*, vol. 20, 2004.

[68] G. Whyman, E. Bormashenko, and T. Stein, "The rigorous derivation of Young, Cassie–Baxter and Wenzel equations and the analysis of the contact angle hysteresis phenomenon," *Chemical Physics Letters*, vol. 450, pp. 355–359, jan 2008.

[69] A. Thompson, *Surface-tension-driven coalescence*. PhD thesis, University of Nottingham, 2011.

[70] D. G. A. L. Aarts, H. N. W. Lekkerkerker, H. Guo, G. H. Wegdam, and D. Bonn, "Hydrodynamics of Droplet Coalescence," *Physical Review Letters*, vol. 95, oct 2005.

[71] N. B. Vargaftik, B. N. Volkov, and L. D. Voljak, "International Tables of the Surface Tension of Water," *Journal of Physical and Chemical Reference Data*, vol. 12, pp. 817–820, jul 1983.

[72] S. L. Bajoria, K. R. Virendra, N. K. Pandey, U. K. Mudali, and R. Natarajan, "Effect of tri-n-butyl phosphate on physical properties of dodecane–nitric acid system," *J Radioanal Nucl Chem*, vol. 295, pp. 271–276, 2013.

[73] S. Nave, C. Mandin, L. Martinet, L. Berthon, F. Testard, C. Madic, and T. Zemb, "Supramolecular organisation of tri-n-butyl phosphate in organic diluent on approaching third phase transition," *Physical Chemistry Chemical Physics*, vol. 6, p. 799, feb 2004.

[74] J. Eggers, J. R. Lister, and H. A. Stone, "Coalescence of liquid drops," *J. Fluid Mech*, vol. 401, pp. 293–310, 2018.

[75] N. Ouerfelli and M. Bouanz, "A shear viscosity study of cerium (III) nitrate in concentrated aqueous solutions at different temperatures," *J. Phys.: Condens. Matter*, vol. 8, pp. 2763–2774, 1996.

[76] L. Duchemin, J. Eggers, and C. Josserand, "Inviscid coalescence of drops," *Journal of Fluid Mechanics*, vol. 487, jun 2003.

[77] M. Wu, T. Cubaud, and C.-M. Ho, "Scaling law in liquid drop coalescence driven by surface tension," *Citation: Physics of Fluids*, vol. 16, 2004.

[78] S.-P. Lyu, F. S. Bates, and C. W. Macosko, "Coalescence in Polymer Blends during Shearing," *AIChE Journal*, vol. 46, no. 2, 2000.

[79] O. Levenspiel, *Chemical reaction engineering.* 1999.

[80] Y. Yoon, A. Hsu, and L. G. Leal, "The influence of surface tension gradients on drop coalescence," *Citation: Physics of Fluids*, vol. 19, p. 1833, 2007.

[81] L. G. Leal, "Flow induced coalescence of drops in a viscous fluid," *Citation: Physics of Fluids*, vol. 16, p. 1833, 2004.

[82] D. Chen, R. Cardinaels, and P. Moldenaers, "Effect of Confinement on Droplet Coalescence in Shear Flow," *Langmuir*, vol. 25, pp. 12885–12893, nov 2009.

[83] X. Li, H. Ren, W. Wu, H. Li, L. Wang, Y. He, J. Wang, and Y. Zhou, "Wettability and Coalescence of Cu Droplets Subjected to Two-Wall Confinement," *Scientific Reports*, vol. 5, p. 15190, dec 2015.

[84] a. K. Chesters, "The modelling of coalescence process in fluid-liquid dispersions: A Review of Current Understanding," *Chemical Engineering Research and Design*, vol. 69, no. 4, pp. 259–270, 1991.

[85] Y. Liu and R. F. Ismagilov, "Dynamics of Coalescence of Plugs with a Hydrophilic Wetting Layer Induced by Flow in a Microfluidic Chemistrode," *Langmuir*, vol. 25, pp. 2854–2859, mar 2009.

[86] M. Minale, J. Mewis, and P. Moldenaers, "Study of the morphological hysteresis in immiscible polymer blends," *AIChE Journal*, vol. 44, pp. 943–950, apr 1998.

[87] R. de Bruijin, *Deformation and breakup of drops in simple shear flows*. PhD thesis, Eindhoven Univ. of Technology, 1989.

[88] H. P. Grace, "Dispersion phenomena in high viscosity immiscible fluid systems and application of static mixers as dispersion devices in such systems," tech. rep., 1982.

[89] G. I. Taylor, "The Formation of Emulsions in Definable Fields of Flow," *Proceedings of the Royal Society A: Mathematical, Physical and Engineering Sciences*, vol. 146, pp. 501–523, oct 1934.

[90] J. Janssen, *Dynamics of Liquid-Liquid Mixing*. PhD thesis, Eindhoven University of Technology., 1993.

[91] E. Lepercq-Bost, M.-L. Giorgi, A. Isambert, and C. Arnaud, "Use of the capillary number for the prediction of droplet size in membrane emulsification," *journal of membrane science*, vol. 314, 2008.

[92] D. Barthès-Biesel and A. Acrivos, "Deformation and burst of a liquid droplet freely suspended in a linear shear field," *Journal of Fluid Mechanics*, vol. 61, p. 1, oct 1973.

[93] H. Mousa, W. Agterof, and J. Mellema, "Experimental Investigation of the Orthokinetic Coalescence Efficiency of Droplets in Simple Shear Flow," *Journal of Colloid and Interface Science*, vol. 240, pp. 340–348, 2001.

[94] J. Blawzdziewicz, R. Goodman, N. Khurana, E. Wajnryb, and Y.-N. Young, "Nonlinear hydrodynamic phenomena in Stokes flow regime," *Physica D: Nonlinear Phenomena*, vol. 239, pp. 1214–1224, jul 2010.

[95] M. Borrell, Y. Yoon, and L. G. Leal, "Experimental analysis of the coalescence process via head-on collisions in a time-dependent flow," *Physics of Fluids*, vol. 16, pp. 3945–3954, nov 2004.

[96] K. B. Migler, "String Formation in Sheared Polymer Blends: Coalescence, Breakup, and Finite Size Effects," *physical re*, vol. 86, 2001.

[97] J. Feng, H. H. Hu, and D. D. Joseph, "Direct Simulation of Initial Value Problems for the Motion of Solid Bodies in a Newtonian Fluid. Part 2. Couette and Poiseuille Flows.," tech. rep., 1994.

[98] J. Feng and D. D. Joseph, "The motion of solid particles suspended in viscoelastic liquids under torsional shear," *Journal of Fluid Mechanics*, vol. 324, p. 199, oct 1996.

[99] D. Highgate, "Particle Migration in Cone-plate Viscometry of Suspensions," *Nature*, vol. 211, pp. 1390–1391, sep 1966.

[100] D.-d. Liu, Y.-m. Xu, X.-t. Ding, J. Yang, and Z.-j. Ma, "Utilizing the Plateau-Rayleigh Instability with Heat-Driven Nano-Biosensing Systems," *Journal of Laboratory Automation*, vol. 20, no. 4, pp. 463–470, 2015.

[101] S. Tomotika, "On the Instability of a Cylindrical Thread of a Viscous Liquid Surrounded by Another Viscous Fluid," *Proceedings of the Royal Society A: Mathematical, Physical and Engineering Sciences*, vol. 150, pp. 322–337, jun 1935.

[102] L. Rayleigh, "On the Stability, or Instability, of certain Fluid Motions," *Proceedings of the London Mathematical Society*, vol. s1-11, pp. 57–72, nov 1879.

[103] H. Mehrabian and J. J. Feng, "Capillary breakup of a liquid torus," *J. Fluid Mech*, vol. 717, pp. 281–292, 2013.

[104] Y. Son, N. S. Martys, J. G. Hagedorn, and K. B. Migler, "Suppression of Capillary Instability of a Polymeric Thread via Parallel Plate Confinement," *Macromolecules*, vol. 36, no. 15, pp. 5825–5833, 2003.

[105] A. Vananroye, P. Van Puyvelde, and P. Moldenaers, "Effect of Confinement on Droplet Breakup in Sheared Emulsions," *Langmuir*, vol. 22, 2006.

[106] T. Cubaud and T. G. Mason, "Capillary threads and viscous droplets in square microchannels," *Citation: Physics of Fluids*, vol. 20, p. 364, 2008.

[107] W. Lee, L. M. Walker, and S. L. Anna, "Role of geometry and fluid properties in droplet and thread formation processes in planar flow focusing," *Citation: Physics of Fluids*, vol. 21, p. 364, 2009.

[108] C. W. Park and G. M. Homsy, "Two-phase displacement in Hele Shaw cells: Theory," *Journal of Fluid Mechanics*, vol. 139, pp. 291–308, 1984.

[109] P. G. Saffman, "Viscous fingering in Hele-Shaw cells," *Journal of Fluid Mechanics*, vol. 173, pp. 73–94, 1986.

[110] M. Hashimoto, P. Garstecki, H. A. Stone, and G. Whitesides, "Interfacial instabilities in a mircofluidic Hele-Shaw cell," *Soft Matter*, vol. 4, no. June, 2008.

[111] P. G. Saffman, "The lift on a small sphere in a slow shear flow," *J. Fluid Mech*, vol. 22, no. 2, pp. 385–400, 1965.

[112] S. D. Hudson, "Wall migration and shear-induced diffusion of fluid droplets in emulsions," *Physics of Fluids*, vol. 15, p. 1106, 2003.

[113] A. Karnis and S. Mason, "Particle motions in sheared suspensions: XXIII. Wall migration of fluid drops," *Journal of Colloid and Interface Science*, vol. 24, pp. 164–169, jun 1967.

[114] D. L. G. Leal and P. Chan, "The motion of a deformable drop in a second-order fluid," Tech. Rep. 1, 1979.

[115] B. Hanson, "Process engineering and design for spent nuclear fuel reprocessing and recycling plants," in *Reprocessing and Recycling of Spent Nuclear Fuel*, pp. 125–151, 2015.

[116] G. Akay, T. Pekdemir, A. M. Shakorfow, and J. Vickers, "Intensified demulsification and separation of thermal oxide reprocessing interfacial crud (THORP-IFC) simulants," *Green Process Synth*, vol. 1, pp. 109–127, 2012.

[117] H. W. Yarrantion and Masliyah J H, "Numerical simulation of Ostwald Ripening in Emulsions," *Journal of colloid and interface science*, vol. 196, pp. 157–196, 1997.

[118] D. J. Luning Prak, S. M. Alexandre, J. S. Cowart, and P. C. Trulove, "Density, Viscosity, Speed of Sound, Bulk Modulus, Surface Tension, and Flash Point of Binary Mixtures of n-Dodecane with 2,2,4,6,6-Pentamethylheptane or 2,2,4,4,6,8,8-Heptamethylnonane.," *journal of chemical engineering data*, vol. 59, 2014.

[119] T. F. Tadros, "Emulsion Formation, Stability, and Rheology," in *Emulsion Formation and Stability*, pp. 1–75, Weinheim, Germany: Wiley-VCH Verlag GmbH & Co. KGaA, jan 2013.

[120] T. Allen, "Particle size, shape and distribution," in *Particle Size Measurement*, pp. 124–191, Dordrecht: Springer Netherlands, 1990.

[121] J. Sauter, "Determining size of drops in fuel mixture of internal combustion engines," *Zeitschrift des vereines des deutscher Ingenieure*, vol. 31, pp. 1–40, 1926.

[122] S. Maab, S. Wollny, A. Voigt, M. Kraume, Á. M. Kraume, S. Wollny, and A. Voigt, "Experimental comparison of measurement techniques for drop size distributions in liquid/liquid dispersions," *Exp Fluids*, vol. 50, pp. 259–269, 2011.

[123] D. Greaves, J. Boxall, J. Mulligan, A. Montesi, J. Creek, E. Dendy Sloan, and C. A. Koh, "Measuring the particle size of a known distribution using the focused beam reflectance measurement technique," *Chemical Engineering Science*, vol. 63, pp. 5410–5419, 2008.

[124] J. A. Boxall, C. A. Koh, E. D. Sloan, A. K. Sum, and D. T. Wu, "Measurement and Calibration of Droplet Size Distributions in Water-in-Oil Emulsions by Particle

Video Microscope and a Focused Beam Reflectance Method," *Industrial & Engineering Chemistry Research*, pp. 1412–1418, 2010.

[125] D. Kucharavy and R. De Guio, "TRIZ Future Conference 2007 Application of S-shaped curves," *Procedia Engineering*, vol. 9, pp. 559–572, 2011.

[126] D. Cremers and L. Radziemski, *Handbook of Laser-Induced Breakdown Spectroscopy*. Wiley, 2013.

[127] F. J. Fortes, J. Moros, P. Lucena, L. M. Cabalín, and J. J. Laserna, "Laser-induced breakdown spectroscopy," *Analytical Chemistry*, vol. 85, no. 2, pp. 640–669, 2013.

[128] A. Kramida, Y. Ralchenko, and J. Reader, "NIST Atomic Spectra Database (ver. 5.5.6)," *National Institute of Standards and Technology, Gaithersburg*, 2018.

[129] Fluent, "FLUENT 6.3 User's Guide," tech. rep., 2006.

[130] H. Wang, Y. Xue, J. Ding, L. Feng, X. Wang, and T. Lin, "Durable, Self-Healing Superhydrophobic and Superoleophobic Surfaces from Fluorinated-Decyl Polyhedral Oligomeric Silsesquioxane and Hydrolyzed Fluorinated Alkyl Silane," *Angewandte Chemie International Edition*, vol. 50, pp. 11433–11436, nov 2011.

[131] D. Bikiaris, P. Matzinos, A. Larena, V. Flaris, and C. Panayiotou, "Use of silane agents and poly(propylene-g-maleic anhydride) copolymer as adhesion promoters in glass fiber/polypropylene composites," *Journal of Applied Polymer Science*, vol. 81, pp. 701–709, jul 2001.

[132] W. van Ooij, D. Zhu, M. Stacy, A. Seth, T. Mugada, J. Gandhi, and P. Puomi, "Corrosion Protection Properties of Organofunctional Silanes—An Overview," *Tsinghua Science & Technology*, vol. 10, pp. 639–664, dec 2005.

[133] V. Gupta, A. Diwan, D. Evans, C. Telford, and M. R. Linford, "Self-termination in the gas-phase layer-by-layer growth of an aza silane and water on planar silicon and nylon substrates," *Journal of Vacuum Science & Technology B, Nanotechnology*

and Microelectronics: Materials, Processing, Measurement, and Phenomena, vol. 32, p. 061803, nov 2014.

[134] B. Johnson, C. Cushman, B. M. Lunt, and M. Kaykhaii, "An Introduction to Silanes , their Chemical Vapor Deposition onto Si / SiO 2 , and Characterization," *vacuum Technology and Coating*, 2016.

[135] M. Luppi and S. Ossicini, "Multiple Si=O bonds at the silicon cluster surface," *Journal of Applied Physics*, vol. 94, pp. 2130–2132, aug 2003.

[136] G. T. Carroll, D. Wang, N. J. Turro, and J. T. Koberstein, "Photons to illuminate the universe of sugar diversity through bioarrays," *Glycoconjugate Journal*, vol. 25, pp. 5–10, jan 2008.

[137] Ghaleb A. Husseini, Justin Peacock, Amarchand Sathyapalan, Lloyd W. Zilch, Matthew C. Asplund, E. T. Sevy, and M. R. Linford, "Alkyl Monolayers on Silica Surfaces Prepared Using Neat, Heated Dimethylmonochlorosilanes with Low Vapor Pressures," 2003.

[138] T. Charpentier, *The heterogeneous ice nucleation properties of structured and chemically tailored surfaces for the development of novel anti-icing materials.* PhD thesis, University of Leeds, 2012.

[139] Matinlinna J and V. Pekka, "Silane Based Concepts on Bonding Resin Composite to Metals," *Journal of contemoirary dental practice*, vol. 8, no. 2, 2007.

[140] G. L. Witucki, "A Silane Primer: Chemistry and Applications of AIkoxy Silanes," *Journal of coatings technology*, vol. 65, 1993.

[141] Yamamoto, H, W. T, and O. I, "A molecular simulation study of an organosilane self-assembeld monolayer/SiO2 substrate interface.," *Journal of chemical physics*, vol. 128, 2008.